

ORBIT EPHEMERIS MONITORS FOR CATEGORY I LOCAL AREA
AUGMENTATION OF GPS

BY

LIVIO RAFAEL GRATTON

Submitted in partial fulfillment of the
requirements for the degree of
Master of Science in Mechanical and Aerospace Engineering
in the Graduate College of the
Illinois Institute of Technology

Approved _____
Adviser

Chicago, Illinois
July 2003

ACKNOWLEDGEMENT

I thank my advisor, Dr. Boris Pervan, for opening to me the door to the fascinating world of Orbital Mechanics, GPS and Research in general, for his passion in transmitting knowledge well beyond the specific needs of my work with him, for his willingness to spend time listening and discussing new ideas with me in spite of the difference in knowledge and experience, for his precious time explaining, as many times as it was necessary, the use of the powerful tools needed to achieve meaningful results; and especially for his patience and understanding regarding my health problems in the past year.

I would also like to thank my defense and reading committees, Dr. Sudhakar Nair and Dr. Rollin Dix for their valuable time on revising this thesis.

I would like to thank all my colleagues, Fang Cheng Chan, Moonbeom Heo, Irfan Sayim, and Mathieu Joerger in the Navigation and Guidance Lab for their helpful assistance and advantageous discussion during the time of my research, and specially Samer Khanafseh, for his precious time saving help in the initialization tests.

I would also like to express my appreciation to the Federal Aviation Administration (FAA) for sponsoring my research.

Finally I want to thank the Ejército Argentino for providing my education as an engineer, and my friend Jerome Chiecchio for his persuasive encouragement to come to the Illinois Institute of Technology.

TABLE OF CONTENTS

	Page
AKCNOWLEDGMENT	iii
LIST OF TABLES	vi
LIST OF FIGURES	vii
LIST OF SYMBOLS	xiii
CHAPTER.	
I. INTRODUCTION	1
1.1 The Global Positioning System	1
1.2 Definition of GPS Orbit Model	6
1.3 Differential GPS and LAAS	8
1.4 Ephemeris Errors Threat Model	11
1.5 Ephemeris Monitoring	12
II. EPHEMERIS ERRORS	15
2.1 Pseudorange and Carrier Phase Measurements	15
2.2 The GPS Orbit Model and The Ephemeris Broadcast Parameters	18
2.3 Sensitivity Analysis	22
2.4 Prior Work	30
III MONITOR BASED ON PREVIOUSLY VALIDATED EPHEMERIDES	33
3.1 The Test Statistic	33
3.2 The Minimum Detectable Error	37
3.3 Satellite Position Estimate	39
3.4 Results	45
3.5 Experimental Verification	50

CHAPTER	Page
IV. MEASUREMENT BASED MONITOR	53
4.1 The Orbit Model.	54
4.2 LGF Measurements	55
4.3 Covariance Analysis and the MDE	58
4.4 Sensitivity Analysis	63
4.5 Cycle Ambiguity Resolution	68
4.6 MDE Values	70
V. CONCLUSIONS	73
APPENDIX	75
A. BROADCAST PARAMETER VALUES DISTRIBUTIONS	75
B. BROADCAST PARAMETER DIFFERENCES FROM DAY TO DAY DISTRIBUTIONS	83
C. SATELLITE POSITION SENSITIVITY TO BROADCASTED EPHEMERIS PARAMETERS VARIATIONS	91
D. EPHEMERIS PARAMETER VALUES	100
E. P_0 PARAMETER VALUES UPDATE FORMULAS FOR SECULAR EFFECTS	108
F. PARAMETER DIFFERENCES 24HS APPART	110
G. DISTRIBUTION OF TEST STATISTIC S FOR K DIFFERENT THAN 0	119
H. DETAIL OF CDF PLOTS FOR K DIFFERENT THAN 0	122
I. SENSITIVITY OF MDE VALUES TO LGF SITING	125
BIBLIOGRAPHY	128

LIST OF TABLES

Table	Page
2.1 GPS Orbit Model Formulas and Ephemeris Parameters	19
3.1 Missed Detection Experimental Verification	51
4.1 Approximate Maximum MDE Value at Different LGF Latitudes	65
4.2 Total MDE Values for Different Baseline Lengths	72

LIST OF FIGURES

Figure	Page
1.1 Three Segments in GPS-based Navigation System	2
1.2 General Differential GPS Configuration	8
2.1 Keplerian Orbit Ephemeris Parameters	21
2.2 Distribution of Values for the Eccentricity	22
2.3 Differences in Δn	26
2.4 Differences in Mean Anomaly	26
2.5 Differences in Argument of Perigee	27
2.6 Differences in $M_0 + \omega$	27
2.7 Position Sensitivity to Parameter Variations	29
3.1 Threshold and Non-Centrality Parameter for S	36
3.2 Fault Free and Failure δr_{total} Probability Space	38
3.3 Values of Parameter a With Time	40
3.4 Values of Parameter a at 24 hs intervals	41
3.5 ZOH and FOH Parameter Prediction Concepts	42
3.6 24hs Differences in Value of Inclination Angle	43
3.7 ZOH and FOH Position Error Distribution	44
3.8 Distribution of Test Statistic S	45
3.9 CDF of Test Statistic S	47
3.10 Tail Overbounding of CDF for ZOH	47
3.11 Tail Overbounding of CDF for FOH	48
3.12 Minimum Detectable Error Results	48

Figure	Page
3.13 MDE Values for Individual SV at k=0	49
4.1 Satellite Position Residuals for Different Orbit Models	54
4.2 MDE Values for Different Time Constants τ	64
4.3 Variation of MDE with Latitude	66
4.4 Variation of MDE with Longitude	66
4.5 MDE Sensitivity to σ_{ϕ}	67
4.6 MDE sensitivity to σ_{ρ}	68
4.7 Standard Deviation on Cycle Ambiguity Estimation for All Satellites...	70
4.8 MDE Values for Different Baseline Lengths	71
A.1 Distribution of Values for the Mean Anomaly	76
A.2 Distribution of Values for Mean Motion Difference From Computed Value	76
A.3 Distribution of Values for Semi-Major Axis	77
A.4 Distribution of Values for Longitude Of Ascending Node of Orbit Plane at toe	77
A.5 Distribution of Values for Inclination Angle at toe	78
A.6 Distribution of Values for Argument of Perigee	78
A.7 Distribution of Values for Rate of Right Ascension	79
A.8 Distribution of Values for Rate of Inclination Angle	79
A.9 Distribution of Values for the Amplitude of the Cosine Harmonic Correction Term to the Argument of Latitude	80
A.10 Distribution of Values for the Amplitude of the Sine Harmonic Correction Term to the Argument of Latitude	80

Figure	Page
A.11 Distribution of Values for the Amplitude of the Cosine Harmonic Correction Term to the Orbit Radius	81
A.12 Distribution of Values for the Amplitude of the Sine Harmonic Correction Term to the Orbit Radius	81
A.13 Distribution of Values for the Amplitude of the Cosine Harmonic Correction Term to the Angle of Inclination	82
A.14 Distribution of Values for the Amplitude of the Sine Harmonic Correction Term to the Angle of Inclination	82
B.1 Distribution of Differences in Eccentricity From Day to Day	84
B.2 Distribution of Differences in Semi-Major Axis From Day to Day	84
B.3 Distribution of Differences in Longitude of Ascending Node From day to Day	85
B.4 Distribution of Differences in Inclination Angle From Day to Day ...	85
B.5 Distribution of Differences in Rate of Right Ascension From Day to Day	86
B.6 Distribution of Differences in Rate of Inclination Angle From Day to Day	86
B.7 Distribution of Differences in Cuc From Day to Day	87
B.8 Distribution of Differences in Cus From Day to Day	87
B.9 Distribution of Differences in Crc From Day to Day	88
B.10 Distribution of Differences in Crs From Day to Day	88
B.11 Distribution of Differences in Cic From Day to Day	89
B.12 Distribution of Differences in Cis From Day to Day	89
C.1 One Sigma Position Difference due to Day to Day changes in Mo ...	92
C.2 One Sigma Position Difference due to Day to Day changes in Δn	92

Figure	Page
C.3 One Sigma Position Difference due to Day to Day changes in e	93
C.4 One Sigma Position Difference due to Day to Day changes in a	93
C.5 One Sigma Position Difference due to Day to Day changes in Ω_0	94
C.6 One Sigma Position Difference due to Day to Day changes in i_0	94
C.7 One Sigma Position Difference due to Day to Day changes in ω	95
C.8 One Sigma Position Difference due to Day to Day changes in $\dot{\Omega}$	95
C.9 One Sigma Position Difference due to Day to Day changes in i_{dot}	96
C.10 One Sigma Position Difference due to Day to Day changes in C_{uc}	96
C.11 One Sigma Position Difference due to Day to Day changes in C_{us}	97
C.12 One Sigma Position Difference due to Day to Day changes in C_{rc}	97
C.13 One Sigma Position Difference due to Day to Day changes in C_{rs}	98
C.14 One Sigma Position Difference due to Day to Day changes in C_{ic}	98
C.15 One Sigma Position Difference due to Day-to-Day changes in C_{is}	99
D.1 M_0 Values for PRN 2 Year 2002	101
D.2 Δn Values for PRN 2 Year 2002	101
D.3 Eccentricity Values for PRN 2 Year 2002	102
D.4 Square Root of a Values for PRN 2 Year 2002	102
D.5 Ω_0 Values for PRN 2 Year 2002	103
D.6 $\dot{\Omega}$ Values for PRN 2 Year 2002	103
D.7 C_{uc} Values for PRN 2 Year	104
D.8 C_{us} Values for PRN 2 Year 2002	104
D.9 C_{rs} Values for PRN 2 Year 2002	105

Figure	Page
D.10 Crc Values for PRN 2 Year 2002	105
D.11 Cis Values for PRN 2 Year 2002	106
D.12 Cic Values for PRN 2 Year 2002	106
D.13 ω Values for PRN 2 Year 2002	107
F.1 Mo Differences Day to Day	111
F.2 Deltan Differences Day to Day	111
F.3 e Differences Day to Day	112
F.4 sqrt(a) Differences Day to Day	112
F.5 Omega _o Differences Day to Day	113
F.6 io Differences Day to Day	113
F.7 omega Differences Day to Day	114
F.8 idot Differences Day to Day	114
F.9 Omegadot Differences Day to Day	115
F.10 Cus Differences Day to Day	115
F.11 Cuc Differences Day to Day	116
F.12 Crs Differences Day to Day	116
F.13 Crc Differences Day to Day	117
F.14 Cis Differences Day to Day	117
F.15 Cic Differences Day to Day	118
F.16 Mo+omega Differences Day to Day	118
G.1 Values of S with ZOH and k= -1 h	120
G.2 Values of S with FOH and k= -1 h	120

Figure	Page
G.3 Values of S with ZOH and $k = -2$ h	121
G.4 Values of S with FOH and $k = -2$ h	121
H.1 FOH Theoretical and Empirical CDF Tails $k = -1$ h	123
H.2 FOH Theoretical and Empirical CDF Tails $k = -2$ h	123
H.3 ZOH Theoretical and Empirical CDF Tails $k = -1$ h	124
H.4 ZOH Theoretical and Empirical CDF Tails $k = -2$ h	124
I.1 MDE Values From Measurement Based Monitoring Latitude= 0°	126
I.2 MDE Values From Measurement Based Monitoring Latitude= 30° ..	126
I.3 MDE Values From Measurement Based Monitoring Latitude= 45°	127
I.4 MDE Values From Measurement Based Monitoring Latitude= 60°	128
I.5 MDE Values From Measurement Based Monitoring Latitude= 90°	128

LIST OF SYMBOLS

Symbol	Definition
A	sensitivity matrix
b	clock bias
B	baseline vector
c	speed of light in vacuum
C	inflation factor
e_i	line of sight unit vector to satellite i
H	observation matrix
I	ionospheric delay
I_(n)	identity matrix of dimension n
k	time relative to toe
N	cycle ambiguity
p	ephemeris parameters vector
P-value	ephemeris decorrelation parameter
\hat{q}	estimate of “q”
r_i	satellite i position vector
r_u	user position vector
R	user satellite vector
S	chi square distributed test statistic
T	tropospheric delay
T	monitor test threshold
W	weighting matrix

Symbol	Definition
\mathbf{Z}	residuals vector
Δ^2	double difference
Δq	residual of “q”
$\delta\mathbf{p}$	ephemeris parameter vector error
$\delta\mathbf{r}$	position error
δt	advance of clock with respect to GPS time
λ	non centrality parameter
λ	carrier wavelength
σ	standard deviation
Σ_q	covariance of “q”
ρ	pseudorange
τ	time constant
v	uncompensated errors and measurement noise
ϕ	carrier phase measurement
ψ	orbit model errors

CHAPTER I

INTRODUCTION

The Global Positioning System (GPS) was designed and implemented in the 1970s to support different military uses. However, after two decades of system development, it has also become an important and versatile utility for civil society. The first chapter of this dissertation describes the basic concepts of GPS architecture and the information cycle between the different system segments. The concept of Differential GPS (DGPS) and its Federal Aviation Administration (FAA) implementation, the Local Area Augmentation System (LAAS) are also described. The idea and need of ephemeris error monitoring is then explained as the motivation for this work. Finally the specifications from LAAS Category I are translated into numbers that will allow measuring the impact of the monitor implementation on LAAS, with respect to satellite availability and necessary infrastructure.

1.1 The Global Positioning System

The current GPS system architecture was proposed by the Department of Defense (DoD) Joint Program Office in 1973 under the direction of Dr. Bradford W. Parkinson. This proposal was a synthesis of prior satellite navigation systems in order to meet requirements of all of the armed services [Par94]*. Full operational capability was attained by the end of 1994. Since then, improvements in the system performance, in signal receiver's capabilities, and the reduction of its costs, have made GPS a tool of widespread use well beyond its initial intent. From geodetic surveys to automobile navigation, it is present in all areas of human development. GPS use for aircraft precision approach and

* Corresponds to coded references in the Bibliography.

landing is one of the main areas of research in navigation at the present moment, and that is the subject of this work.

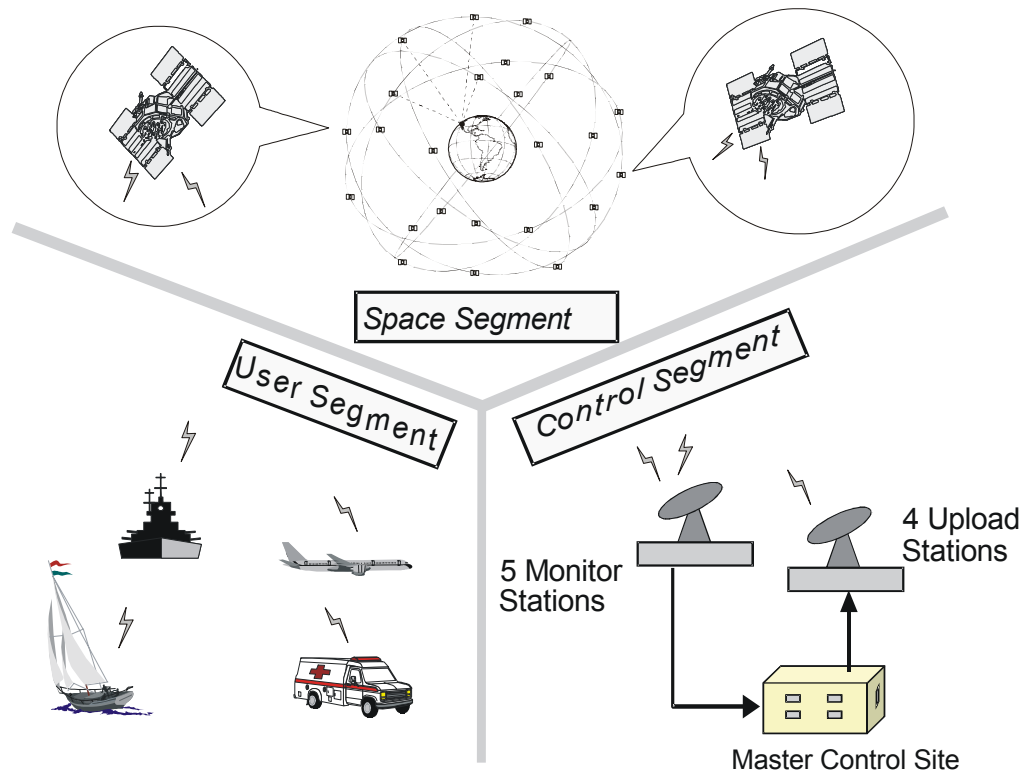


Figure 1.1 Three Segments in GPS-based Navigation System

The GPS system consists of three segments [Spi94]: the space segment, the control segment and the user segment, as shown in Figure 1.1. *The control segment* has five Monitoring Stations that track the satellite's position and velocity. This information is processed by the Master Control Station to compute and update the parameters that serve as input in the orbital model that describes GPS satellite motion. Once a day, that information is sent to the satellites via the last basic element of the control segment: the

four Uploading Stations. The ground control segment will also keep satellite clock error within requirements, and command satellite maneuvers when needed. *The space segment* comprises 24 space vehicles (SV) (plus some spare satellites) distributed over space to provide global signal coverage. Each of these satellites continuously transmits a ranging signal that includes navigation data (the ephemeris parameters and other parameters related to clock error). *The user segment* includes all user receivers. These receivers measure their distance to each satellite by observing the time it took for the signal to reach them. With these ranges, and the computed satellite locations at the time of transmission (obtained using the ephemeris data the satellite itself broadcasts), the user estimates its own position.

GPS satellites broadcast the ranging signals along with navigation data on two different frequencies: a civil signal (L1) and a military signal (L2). Only the L1 signal is considered in this thesis, since the goal is to achieve an ephemeris monitor that is realizable with the civil Category I LAAS infrastructure. The L1 band is centered at 1575.42 MHz and is modulated with a Course Acquisition (C/A) code and a Precise (P/Y) code. The P/Y code is encrypted and reserved for military users, so this work does not deal with it.

The L1 is also modulated with navigation data that includes satellite orbit ephemerides. The service provided by the C/A code is called Standard Positioning Service (SPS). When a civil user receiver is tracking a satellite signal, it can measure the distance between the receiver and the satellite using a Delay Lock Loop (DLL). That is, it compares the received signal with a replica generated within the receiver. By computing how much it has to delay the replica signal to make them match, it knows the time

difference between satellite broadcast and receiver reception. Multiplying by the speed of light, it has the range to that satellite. This is an ideal case, in reality the obtained measurement (ρ_i) is:

$$\rho_i = |\mathbf{r}_i - \mathbf{r}_u| + cb_u + \varepsilon_{\rho_i} \quad (1-1)$$

The first term in the right side is the distance between the position vector of the i th satellite (\mathbf{r}_i) (calculated from the broadcast ephemeris) and the position vector of the user receiver (\mathbf{r}_u), which is the basic unknown to be determined. The second term (cb_u) is the product of the difference between receiver clock and GPS system time (b_u), and the speed of light (c). The source of this term is the user receiver, and thus is a bias common to measurements to all satellites. The third term (ε_{ρ_i}) includes all remaining measurement error sources such as satellite clock offset from GPS time, tropospheric delay, ionospheric delay, satellite ephemeris error, multipath error, and receiver noise. Since, as seen above, code measurements are the composite of true ranges and other (error) sources, a more suitable name for the raw code measurement of user-satellite distance is *pseudorange*.

In order to estimate the user position, \mathbf{r}_u , and the receiver clock bias error, cb_u , the measurement equation is linearized about a nominal value (a prior estimate of \mathbf{r}_u).

Defining a prior estimate of state vector:

$$\hat{\mathbf{x}} = \begin{bmatrix} \hat{\mathbf{r}}_u & \hat{cb}_u \end{bmatrix}^T \quad (1-2)$$

and an estimate of other error sources as $\hat{\varepsilon}_{\rho_i}$, the pseudorange measurement can be predicted as follows:

$$\hat{\rho}_i = |\mathbf{r}_i - \hat{\mathbf{r}}_u| + c\hat{b}_u + \hat{\varepsilon}_{\rho_i} \quad (1-3)$$

Defining the difference between the measured and the predicted pseudoranges as the measurement residual:

$$\Delta\rho_i = \hat{\rho}_i - \rho_i \quad (1-4)$$

the linearized measurement equation can be written as:

$$\Delta\rho_i = \begin{bmatrix} -\hat{\mathbf{e}}_i^T & 1 \end{bmatrix} \begin{bmatrix} \Delta\mathbf{r}_u \\ c\Delta\mathbf{b}_u \end{bmatrix} + \Delta\varepsilon_{\rho i} \quad (1-5)$$

where

$\hat{\mathbf{e}}_i \equiv \frac{\mathbf{r}_i - \hat{\mathbf{r}}_u}{|\mathbf{r}_i - \hat{\mathbf{r}}_u|}$, is the estimated line of sight unit vector, and

$$\Delta\mathbf{r} \equiv \hat{\mathbf{r}}_u - \mathbf{r}_u, \quad \Delta\mathbf{b}_u \equiv \hat{\mathbf{b}}_u - \mathbf{b}_u, \quad \Delta\varepsilon_i \equiv \hat{\varepsilon}_{\rho i} - \varepsilon_{\rho i}$$

Because there are three position states (the three user position coordinates) and one clock bias state (the receiver clock difference from GPS time), four or more satellites in view are needed to resolve the state vector. A matrix equation can express the stack of these four or more measurement residuals equations as follows:

$$\Delta\boldsymbol{\rho} = \mathbf{G} \Delta\mathbf{x} + \Delta\boldsymbol{\varepsilon} \quad (1-6)$$

$$\text{where } \Delta\boldsymbol{\rho} = \begin{bmatrix} \Delta\rho_1 \\ \Delta\rho_2 \\ \vdots \\ \Delta\rho_n \end{bmatrix}, \quad \mathbf{G} = \begin{bmatrix} -\hat{\mathbf{e}}_1^T & 1 \\ -\hat{\mathbf{e}}_2^T & 1 \\ \vdots & \vdots \\ -\hat{\mathbf{e}}_n^T & 1 \end{bmatrix}, \quad \Delta\mathbf{x} = \begin{bmatrix} \Delta\mathbf{r}_u \\ c\Delta\mathbf{b}_u \end{bmatrix}, \quad \text{and} \quad \Delta\boldsymbol{\varepsilon} = \begin{bmatrix} \Delta\varepsilon_{\rho 1} \\ \Delta\varepsilon_{\rho 2} \\ \vdots \\ \Delta\varepsilon_{\rho n} \end{bmatrix}$$

The pseudorange measurement noise ($\Delta\boldsymbol{\varepsilon}$) is assumed to be zero mean, so the least squares solution to the set of normal equations is obtained as follows:

$$\Delta\hat{\mathbf{x}} = (\mathbf{G}^T \mathbf{G})^{-1} \mathbf{G}^T \Delta\boldsymbol{\rho} \quad (1-7)$$

When a prior estimate of user position used to construct matrix \mathbf{G} is off by a large amount (a few kilometers), iteration might be necessary until the change of the least

squares estimate is sufficiently small. However, matrix \mathbf{G} is constructed from line-of-sight unit vectors and the satellite distance from the user is very large, so it is not very sensitive to prior position estimate error.

If the measurement error variances are not equal across all satellites, a diagonal weighting matrix $\mathbf{W}^{-1/2}$ [Zum96] may be introduced to give a weighted least squares estimate:

$$\Delta\hat{\mathbf{x}} = (\mathbf{G}^T \mathbf{W}^{-1} \mathbf{G})^{-1} \mathbf{G}^T \mathbf{W}^{-1} \Delta\mathbf{p} \quad (1-8)$$

The equations defined above represent the basic single point solution in GPS positioning. In general, more precise pseudorange measurements (small $\Delta\epsilon_p$) and good satellite geometry (well separated and redundant) will result in a more accurate user position estimate.

Of all the error sources mentioned in this section, one is the concern of this thesis: the *satellite orbit ephemeris*.

1.2 Definition of GPS Orbit Model

The ideal GPS satellite orbit is a circular orbit with an inclination of 55° and a period of 12 sidereal hours. Considering a Keplerian orbit model, this implies an *eccentricity* (e) of 0 and a *semi major axis* (a) of 26,561.75 km. The true longitude at epoch for each satellite in the constellation was defined such as to provide the necessary four satellite signal coverage, globally at all times.

Keplerian orbits are based solely on the attraction between two spherical bodies. GPS satellite orbits are affected and shaped by many other factors as well. The most important divergence from a Keplerian model being that the earth is not spherical but oblate in shape. Significant additional effects come from the attraction of the moon, the

sun, the solar radiation pressure, other planets and some error when putting the satellite on its orbit.

The control segment, with sophisticated orbit models, and the constant updates from its monitoring stations, can very accurately predict satellite behavior. But the information that satellites can handle and broadcast is strongly limited by the hardware weight/cost constraint of what can be put in orbit. There is also a constraint related to how fast and how often the uploading stations can send information to the satellites.

To provide the user with the necessary information in spite of these data flow limitations, GPS uses a simplified formula that requires relatively few parameters as input to model the satellite orbit. These ephemeris parameters however are valid for a limited time and have to be updated regularly. Once a day, 12 sets of ephemerides are uploaded to each satellite. A given ephemeris is very accurate for two hours, after which the satellite automatically changes to the following ephemeris equally accurate for that new two-hour span, and so on until the new upload 24 solar hours later. The user receiver uses them to compute the satellite position by adding the time of transmission as the last necessary input. In this work, the term *GPS Orbit Model* refers to the model used by receivers to compute satellite positions, and *Broadcast Ephemeris* is the corresponding set of parameters broadcasted by the satellite itself that serve as inputs to that model.

The normal errors due to imperfections in the *GPS Orbit Model* are typically about three meters rms, but can be as big as 10m [Mis99]. This nominal error is not significant when compared to the anomalous errors considered in this work, which are of the order of thousands of meters. Discarding this small nominal error, when the *true position* of a satellite is needed for comparison or any other consideration, that position is computed

using the *GPS Orbit Model* with the corresponding fault free broadcasted ephemeris for that specific time.

1.3 Differential GPS and LAAS

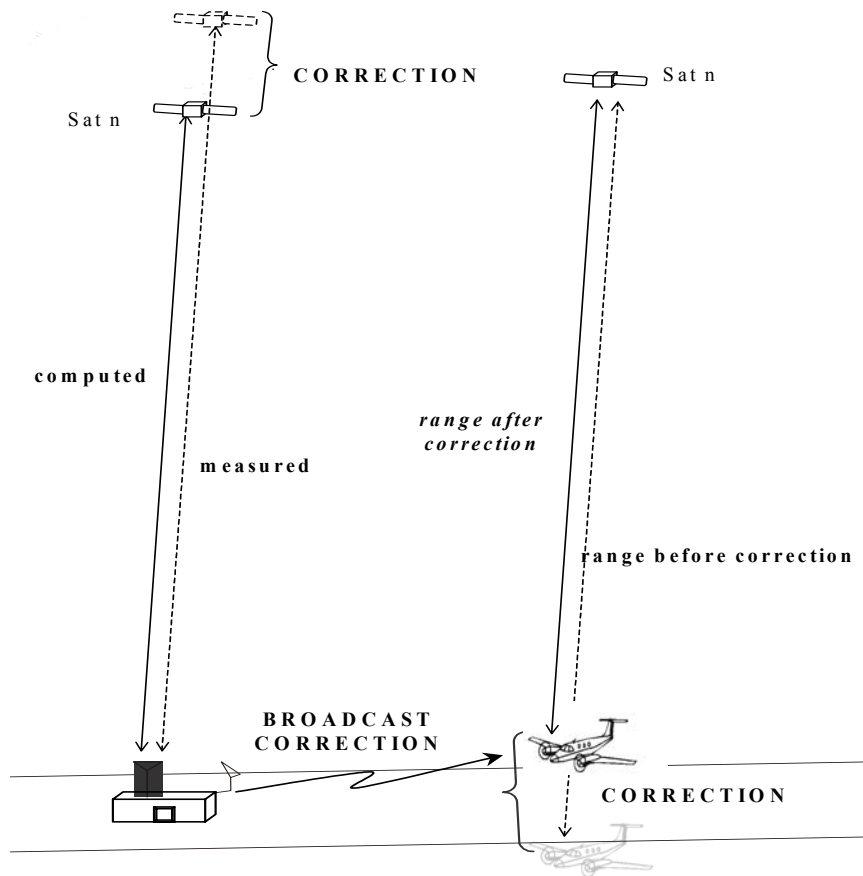


Figure 1.2 General Differential GPS Configuration

DGPS is a powerful tool to reduce measurement errors. The main concept in DGPS is that a receiver at the ground facility (the *LAAS Ground Facility (LGF)* specifically for

LAAS), whose exact location is known, compares its measured ranges to the satellites with the distances computed using the *broadcast ephemeris*. It can then send a ranging correction for each satellite to the users that will add them to their own measurements making them more accurate. This correction capability can reduce the user positioning error from tens of meters to the sub-meter level. [Mis99]

The FAA is transitioning the National Airspace System (NAS) from ground based to satellite based navigational aids. The new architecture would consist of GPS, the Wide Area Augmentation System (WAAS), and its version of DGPS, LAAS. LAAS is intended to be the primary radio-navigation system for Category (Cat) I II and III Precision Approach and Landing. LAAS Cat I is the object of this work, so no further reference to Cat II/III or WAAS is made. LAAS is expected to enhance airport capacity by increasing the number of aircraft that can land under all weather conditions and providing for more flexible approaches to airports, especially by allowing shorter curved paths that will save fuel usage. In addition, LAAS is also considered to be an enabling technology to help prevent accidents on runways and taxiways.

The main distinguishing feature of LAAS compared to other DGPS structures, is that it uses *multiple* receivers with high performance Multipath Limiting Antennas (MLA). Even though the use of multiple receivers was not originally related to ephemeris monitoring, if these antennas are physically located with a certain pattern, they form baselines that can be useful in its implementation.

LAAS has strict specifications that have to be met. A brief description of them follows, as they provide the boundaries and guidelines for this research.

Availability: the ability of the system to provide the required function at the initiation of the approach. Basically the percentage of time the system is functioning correctly and can be used. This specification will vary between 0.99 and 0.99999 depending on the location and use of the airport being considered. It always has to be equal or better than the availability provided by existing Instrument Landing System (ILS) installations.

Integrity: the trust that can be placed on the correctness of the information supplied. The integrity risk is the most hazardous of all, since it means that not only the information is wrong, but also it is assumed to be right. The requirement on LAAS Cat I integrity risk is that it be smaller than 2×10^{-7} per approach.

Continuity: the probability that the system (LAAS) will perform its function without interruption during the intended operation (landing). This assumes the system was operational at the beginning of the approach. The continuity interruption probability must be smaller than 8×10^{-6} per every 15 seconds.

Other specifications for LAAS not directly related to this work can be found in [PT1LAAS99], [PTLAAS00], [PTFAA01].

In the case of ephemeris monitoring, its consideration as an integrity issue has changed (increased) compared to when the LAAS architecture was initially conceived. The need of a more effective monitor was realized when the evaluation process for the system was already started.

Therefore the ideal result of this research would be to *find a process or algorithm that effectively monitors ephemeris errors, without affecting the availability or continuity performance achieved before the monitor's implementation.*

1.4 Ephemeris Errors Threat Model

The ephemeris messages for each satellite is created and broadcasted independently, and since ephemeris anomalies are low probability events, the likelihood of multiple simultaneous ephemeris failures is assumed to be negligible.

The current LAAS ephemeris threat model identifies two types of hazards, the first type being subdivided into two separate classes:

Type A: The broadcast ephemeris data is erroneous following a satellite maneuver.

Type A1: The satellite maneuver is announced to the LGF.

Type A2: The LGF is unaware of the satellite maneuver.

Type B: The broadcast ephemeris data is erroneous, but no satellite maneuver is involved.

The likelihood of Type B failures is higher than Type A because orbit ephemeris uploads and broadcast ephemeris changeovers are frequent (once per day and once every two hours, respectively) whereas spacecraft maneuvers are rare (approximately once every two years per satellite). With regard to means of detection, Type B failures are easier to detect than Type A1 because anomalies of the former type can be identified by comparison with prior validated broadcast ephemerides. In contrast, prior ephemerides are of no use in the detection of Type A1 failures because of the intervening maneuver. Ideally, the monitor to be implemented should be able to detect both types of failures.

Since unannounced maneuvers undoubtedly represent a very small subset of all spacecraft maneuvers, Type A2 failures are expected to be much less likely than Type A1. Given the unlikelihood of Type A2 failures a monitor for Type B and Type A1 ephemeris

failures is considered sufficient for Cat I precision approach and landing. (Real time detection of Type A2 failures requires dual frequency receivers). [Cha01]

1.5 Ephemeris Monitoring

For aircraft navigation with LAAS, it is a system requirement that both space and ground segment failures must be detected and isolated by the LGF before differential corrections are broadcast. The aircraft is accountable only for the management of failures in its own navigation avionics

In general, integrity for LAAS fails when an error in position exceeds the *Horizontal Alert Limit* (HAL) or the *Vertical Alert Limit* (VAL), and this error is not annunciated to the pilot. The vertical requirements for LAAS are more stringent than the horizontal, so only vertical is considered in this work. Analogous derivations can be done for HAL.

The alert limit varies depending on the type of precision approach, and the position of the aircraft relative to the runway. The most critical user location is when the aircraft reaches the end of its approach. For Category I, this occurs at a 200 feet altitude where $VAL = 10$ m.

LAAS users continuously generate a *Vertical Protection Level* (VPL) that takes into account the different error sources and satellite geometry. When this number exceeds the VAL, it means the system cannot rule out an integrity failure within the specified integrity risk requirement, and an alarm will sound. The VPL/VAL test may also generate a number of *Fault Free Alarms* (FFA) that affect availability. This is acceptable as long as the probability of FFA's complies with the specifications of LAAS given in section 1.4.

The *Vertical Protection Level for an Ephemeris failure hypothesis (VPL_e)* for each satellite “i” is computed at the aircraft using [Pul02]:

$$\text{VPL}_e(i) = \text{Pvalue}_i \left(\|\mathbf{S}_{\text{vert},i}\| \|\mathbf{x}\| + k_{\text{md}} \sqrt{\sum_{j=1}^n S_{\text{vert},j}^2 \sigma_j^2} \right) \Rightarrow \text{VPL}_e = \max_i \text{VPL}_e(i) \quad (1-9)$$

where

$S_{\text{vert},i}$ is the i-th element of the row of the weighted-least-squares projection matrix corresponding to the vertical position state

σ_i is the fault free ranging error standard deviation for the i-th satellite.

k_{md} is a missed detection multiplier (based on the prior probability of an ephemeris anomaly and the LAAS navigation integrity risk requirement allocated to ephemeris faults).

P-value $_i$ is the *ephemeris decorrelation parameter* for satellite i. The P-value for each satellite is broadcast by the LGF to users.

Its magnitude is proportional to the minimum ephemeris error detectable by the LGF ephemeris monitor, and inversely proportional to the range:

$$\text{Pvalue}_i = \frac{\text{MDE}}{\rho_i} \quad (1-10)$$

The *Minimum Detectable Error (MDE)* is the smallest position error that can be detected at the LGF (within the misdetection probability constraint). From (1-9) and (1-10) it is obvious that the smaller the MDE, the smaller the VPL_e so the main aim of this work is to validate and reduce the magnitude of the MDE values.

This monitoring process at the aircraft will also generate a number of FFAs. If the probability of a FFA is sufficiently low, then the needed integrity with respect to ephemeris errors will be provided without affecting navigation availability or continuity.

Prior work performed at MITRE Corporation [Shi01] shows that for an MDE smaller than approximately 3500m, the availability for LAAS is not affected. Thus, the ideal result for this research stated at the end of section 1.4 can be more specifically defined as *providing an algorithm that effectively monitors ephemeris errors, with an MDE smaller than 3500 m.*

CHAPTER II

EPHEMERIS ERRORS

Prior to deriving specific fault detection algorithms, it is useful to study the nature of the possible ephemeris errors and how they will affect the user of LAAS. To do so, this chapter offers a brief description of the basic measurements available at the LGF, their error sources and how the errors are reduced by the DGPS implementation. This is followed by a description of the *GPS Orbit Model* and the *Broadcast Ephemeris* defined in Chapter I, with a sensitivity analysis of satellite position to variations in these parameters. This is an interesting study in itself, but its results will also provide useful options for the specific task being pursued. Some general results are also shown that helped orient and frame the thought process that led to the final monitor model.

2.1 Pseudorange and Carrier Phase Measurements

There are two basic kinds of measurements used by GPS receivers in the applications that concern this work, the Pseudorange and the Carrier Phase measurement. They can also be combined or differenced in various ways to help eliminate error sources or for smoothing as will be seen in Chapter IV. As noted earlier, the pseudorange is basically the difference between the signal's time of broadcast (at the satellite) and the user's reception time, multiplied by the speed of light. This is the measurement defined in (1-1). It is expanded in (2-1) to better understand the error sources:

$$\rho = R + c[\delta t_u - \delta t^s + I + T] + v \quad (2-1)$$

where:

ρ = pseudorange

R = true user-satellite distance

δt_u = advance of the receiver clock with respect to the GPS system

δt^s = advance of the satellite clock with respect to the GPS system

I = signal delay due to the ionosphere

T = signal delay due to the troposphere, and

υ = all other uncompensated model and measurement errors (including multipath and receiver noise).

The pseudorange is unambiguous, since it gives a unique scalar as a result, but the errors due to receiver noise and multipath can be at the meter level. [Mis99]

The Carrier phase measurement is obtained by computing the difference between the phase of the broadcast signal at the moment of reception, and the phase of the identical auto generated signal at the receiver. Since the wavelength of this signal is 19 cm, once the phase lock is obtained, the measurement is very precise (centimeter level) compared with the meter level precision of the pseudorange. The phase difference within a cycle is obtained, but the number of full cycles elapsed is unknown. Determining this cycle ambiguity is essential for the full use of this measurement's advantages. The formula for the carrier phase measurement is then:

$$\phi\lambda = R + c[(\delta t_u - \delta t^s) + I + T] + N\lambda + \delta\phi_u^s\lambda + \upsilon \quad (2-2)$$

where the new elements introduced with respect to (2-1) are:

ϕ = carrier phase measurement in units of cycles

λ = carrier wavelength

N = number of full cycles (ambiguity)

$\delta\phi_u^s$ = initial phase difference between SV and receiver clocks

These corrections do not eliminate non-common errors caused by multipath, receiver noise and the receiver's clock errors, but if the distance between the LGF and the user is small enough, the errors produced by the I, T and satellite clock error terms, can be considered common to both.

The *Differential Ranging Error (DRE)* $\delta\Delta\phi_i$ is defined as the residual after differencing the two ranges from a satellite to two different antennas (at airport, and at user receiver), after the computed difference is subtracted from the measured one. The behavior of the fault free noise is known in a statistical sense, and given correct broadcast parameters the GPS orbital model gives an insignificant error (less than 10 meters for a 20,000 km (minimum) range). So in case of an anomalous ephemeris error, the magnitude of $\delta\Delta\phi_i$ is an indicator of how much of the error caused by the ephemeris failure remains in the satellite-user range after the ranging correction transmitted by the LGF has been applied.

It is shown in reference [Cha01] that the effective differential ranging error due to an ephemeris anomaly is:

$$\delta\Delta\phi_i \equiv \Delta R_{\alpha\beta}^i - \mathbf{e}_\alpha^i \mathbf{T} \mathbf{B} = \delta\mathbf{e}_\alpha^i \mathbf{T} \mathbf{B} \quad (2-3)$$

where:

$\Delta R_{\alpha\beta}^i$ = range to satellite i from antenna "α" minus range to satellite i

from antenna "β"

\mathbf{e}_α^i = LOS unit vector.

\mathbf{B} = baseline vector between the two antennas.

$\delta\mathbf{e}_\alpha^i$ = LOS unit vector error

It can be shown [Cha01] that the LOS unit vector error can be expressed to first order as a function of the SV position error with the following :

$$\delta\Delta\phi_i = \delta\mathbf{e}_\alpha^i \mathbf{B} = \frac{1}{R} [(\mathbf{I}_{(3)} - \mathbf{e}_\alpha^i \mathbf{e}_\alpha^{i T}) \delta\mathbf{r}_i]^T \mathbf{B} \quad (2-4)$$

where:

R = range to satellite (computed using broadcast ephemeris)

\mathbf{I} = identity matrix where the number in parenthesis expresses dimension.

$\delta\mathbf{r}_i$ = SV position error from ephemeris discrepancy

This formula directly relates the single difference measurement error with the SV position error. As it is based on the error in the LOS unit vector, it is only concerned with differences that are orthogonal to this LOS; and that is what is needed. Recall that errors in the LOS will be removed with the correction transmitted to the aircraft from the LGF (see Fig 1.2).

2.2 The GPS Orbit Model and The Ephemeris Broadcast Parameters

The *GPS Orbit Model* and The *Ephemeris Broadcast Parameters* is what the user utilizes to obtain the satellite position \mathbf{r} . The complete formulas for the computation of \mathbf{r} in Earth Centered Earth Fixed (ECEF) X, Y, Z coordinates can be found in Table 2.1. Some particular concepts directly related to this research follow.

Ideally, once an orbit is defined, the same set of parameters can be used to compute the position by changing only the time. As has been said, the *GPS Orbit Model* is valid for a limited time only, which is why a new set of parameters is broadcasted every two hours.

Table 2.1. GPS Orbit Model Formulas and Ephemeris Parameters

Term/Parameter	Formula/Definition
n_o	$= (\mu/a^3)^{1/2}$
t_k	$= t-toe$
n	$= n_o + \Delta n$
M_k	$= M_o + n t_k$
M_k	$= E_k - e \sin(E_k)$
v_k	$= \tan^{-1}(\{[(1-e^2)^{1/2}] \sin(E_k)\} / [\cos(E_k) - e])$
ϕ_k	$= v_k + \omega$
δu_k	$= C_{us} \sin(2 \phi_k) + C_{uc} \cos(2 \phi_k)$
δr_k	$= C_{rs} \sin(2 \phi_k) + C_{rc} \cos(2 \phi_k)$
δi_k	$= C_{is} \sin(2 \phi_k) + C_{ic} \cos(2 \phi_k)$
u_k	$= \phi_k + \delta u_k$
i_k	$= i_o + \delta i_k + \dot{i} t_k$
x_k'	$= r_k \cos(u_k)$
y_k'	$= r_k \sin(u_k)$
Ω_k	$= \Omega_o + (\Omega \dot{\Omega} - \Omega E \dot{\Omega}) t_k - \Omega E \dot{\Omega} toe$
X	$= x_k' \cos(\Omega_k) + y_k' \cos(i_k) \sin(\Omega_k)$
Y	$= x_k' \sin(\Omega_k) + y_k' \cos(i_k) \cos(\Omega_k)$
Z	$= y_k' \sin(i_k)$
Δn :	mean motion difference from computed value
a :	semimajor axis
e :	eccentricity ($e = (1 - p/a)^{1/2}$)
i_o :	inclination at $t=toe$
Ω_o :	longitude of ascending node of orbit plane at $t=toe$
ω :	argument of perigee
M_o :	mean anomaly at $t=toe$
Toe :	reference time for ephemeris
\dot{i} :	rate of inclination angle
$\Omega \dot{\Omega}$:	rate of right ascension.
C 's :	amplitudes of sine and cosine harmonic correction terms for argument of latitude, orbit radius and angle of inclination.
μ	Earth gravitational parameter (constant)
$\Omega \dot{\Omega}$	Earth rotation rate (constant)

There are some parameters for which a two-hour wait for an update would be too long. These parameters are the *Mean Anomaly (M)*, the *Inclination (i)* and the *Longitude*

of the *Ascending Node* (Ω). Their change within those two hours can be easily and sufficiently approximated by simply introducing a rate, and multiplying it by the lapse between the time of interest, and a reference time *Time Of Ephemeris* (*toe*) for which the three mentioned parameters are exactly valid. These rates are Δn , \dot{i} and $\dot{\Omega}$ respectively.

The argument of latitude is the angle (in the plane of the orbit) with vertex at the center of the earth and the two arm directions determined by the ascending node (point where the orbit crosses the equatorial plane northbound) and the satellite position. It is determined by the sum of two parameters: the *argument of periapsis* or ω (angle from node to periapsis) and the *true anomaly* or ν (angle from periapsis to satellite) (Fig 2.1). If the orbit is circular, ω is undefined, so even though the argument of latitude is described by the model with the same accuracy, when the orbit is nearly circular, the distinction between the two parameters that define it is more difficult to achieve. This is not an issue for determining the satellite position at each time, but could be, if not properly considered, when trying to predict the parameter values using previously validated sets of ephemerides.

GPS works in ECEF coordinates. To get a better insight on the results, most errors or differences computed during this work, were converted to *Local Level* (LL) coordinates, that have their origin at the satellite position at each time, and consist of the *Intrack* component in the direction of the satellite motion, the *Radial* component, in the satellite to earth-center direction, and the *Crosstrack* component orthogonal to the other two.

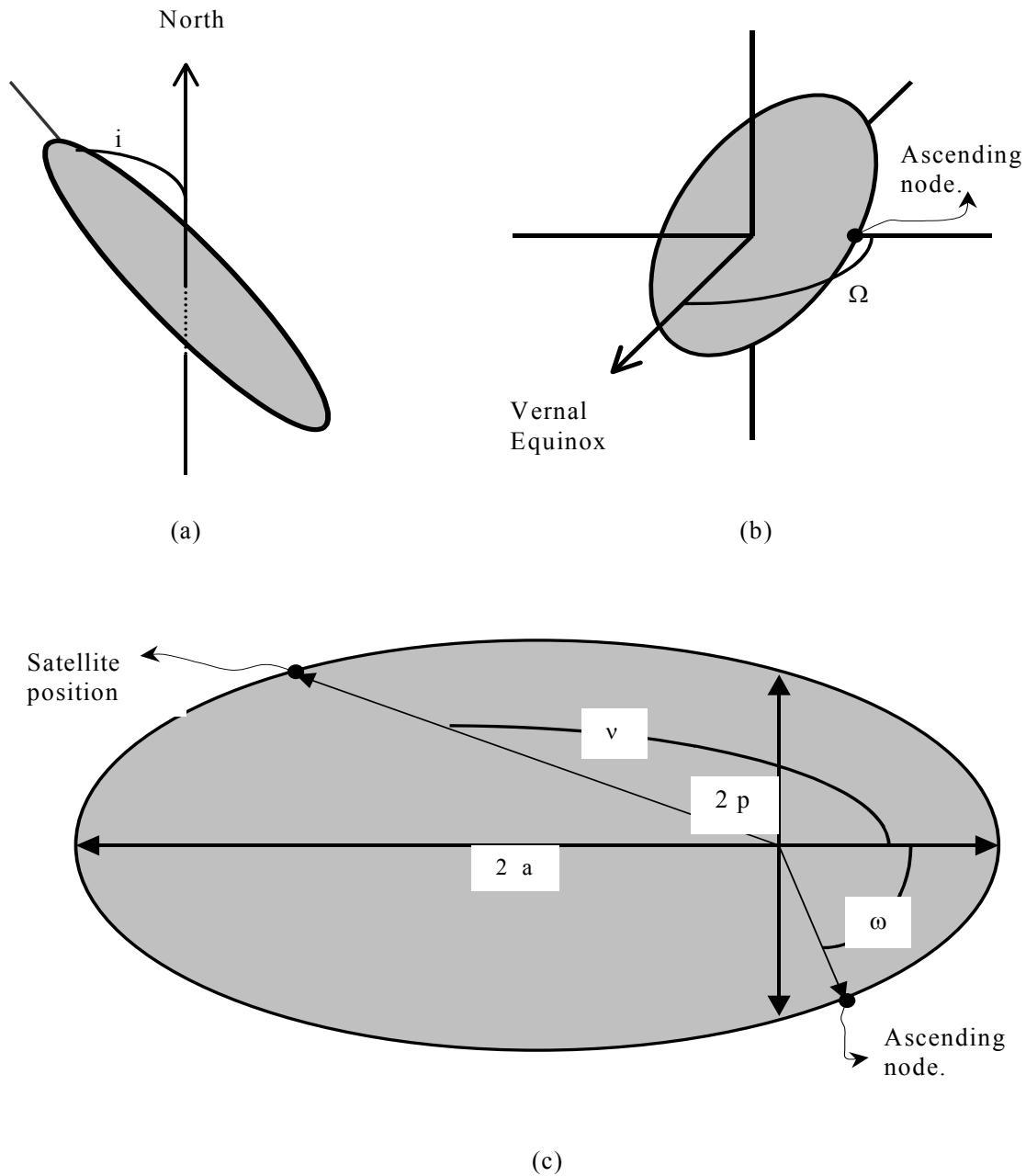


Figure 2.1 Keplerian Orbit Ephemeris Parameters: (a) Inclination i , (b) Longitude of Ascending Node Ω , (c) Parameters in Orbit Plane

2.3 Sensitivity Analysis

The data used, is the full set of ephemerides for all satellites, stored at the NASA's Crustal Dynamics Data Information System site, for the year 2002. The total number of ephemerides stored is 134,618.

The first thing observed is the distribution of the values for each parameter. This gives an approximate idea of how close the shape of the orbits is to the ideal circular orbit model.

Values are similar to the expected ones. Semi-major axis values around 26,562 km, inclinations are close to the 55° value, and the eccentricities are all smaller than 0.023. (Fig 2.2) Some expected characteristics can also be observed in the data, like the fact that the *inclination rate* has 0 mean because it is cyclic, while the *Longitude of Ascending Node rate* has a negative mean expected by the nodal regression caused by the earth's oblateness.

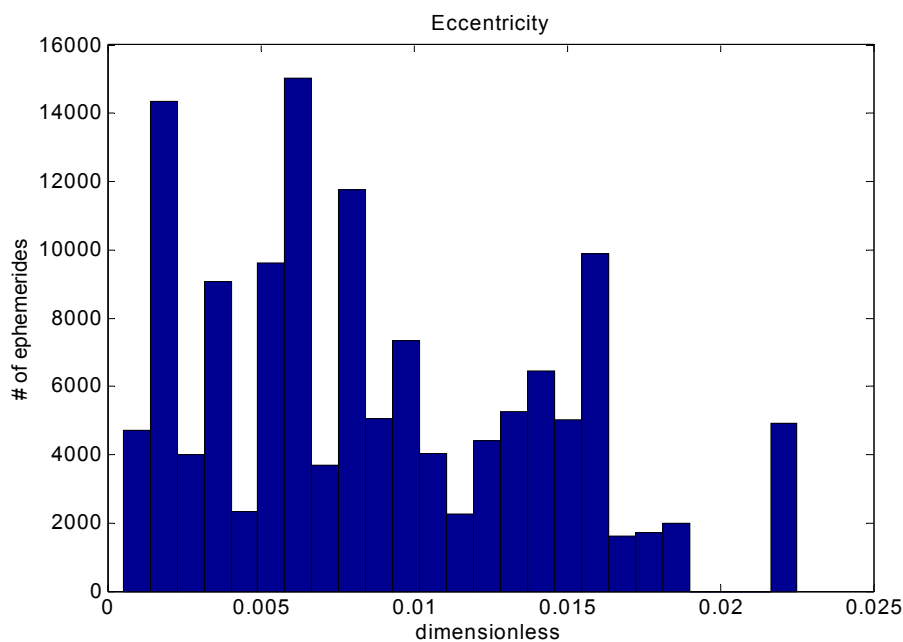


Figure 2.2 Distribution of Values for the Eccentricity

An important factor that emerges from observing the Keplerian parameters is that the variation from satellite to satellite is more significant than the variation of the values with time for each satellite. That explains the gaps and shape in some of the distributions (Fig 2.2). The plots for the whole set of data can be found in Appendix A.

After this first general check, and with an idea of how the ephemeris parameter values are distributed, the sensitivity of the position coordinates with respect to each broadcast parameter has to be established.

Given the time-of-ephemeris (t_{oe}) and the fifteen broadcast ephemeris parameters

$$[p_1, \dots, p_{15}] = [a, M_0, \Delta n, e, \Omega_0, I_0, IDOT, \dots] \quad (2-5)$$

the satellite position (x, y, z) can be computed at any time t :

$$\begin{bmatrix} x(t) \\ y(t) \\ z(t) \end{bmatrix} = \begin{bmatrix} f(p_1, \dots, p_{15}, t_{oe}, t) \\ g(p_1, \dots, p_{15}, t_{oe}, t) \\ h(p_1, \dots, p_{15}, t_{oe}, t) \end{bmatrix} = \begin{bmatrix} f(\mathbf{p}, t_{oe}, t) \\ g(\mathbf{p}, t_{oe}, t) \\ h(\mathbf{p}, t_{oe}, t) \end{bmatrix} \quad (2-6)$$

where \mathbf{p} is the parameter vector (15 elements), and the nonlinear functions f , g , and h are defined by the satellite position algorithms in Table 2-1.

Now consider sensitivity to parameter variations:

$$\begin{bmatrix} \delta x(t) \\ \delta y(t) \\ \delta z(t) \end{bmatrix} = \begin{bmatrix} \frac{\partial f(\mathbf{p}, t_{oe}, t)}{\partial p_1} & \dots & \frac{\partial f(\mathbf{p}, t_{oe}, t)}{\partial p_{15}} \\ \frac{\partial g(\mathbf{p}, t_{oe}, t)}{\partial p_1} & \dots & \frac{\partial g(\mathbf{p}, t_{oe}, t)}{\partial p_{15}} \\ \frac{\partial h(\mathbf{p}, t_{oe}, t)}{\partial p_1} & \dots & \frac{\partial h(\mathbf{p}, t_{oe}, t)}{\partial p_{15}} \end{bmatrix} \begin{bmatrix} \delta p_1 \\ \vdots \\ \delta p_{15} \end{bmatrix}. \quad (2-7)$$

In a more compact form:

$$\delta \mathbf{r}(t) = \mathbf{A}(\mathbf{p}, t_{oe}, t) \delta \mathbf{p}. \quad (2-8)$$

\mathbf{A} is the 3×15 *sensitivity matrix* computed by partial differentiation of f , g , and h .

The last equation is then a linearized expression directly relating parameter and position

variation. Each term in the sensitivity matrix is a function of 15 reference broadcast parameters and is also an explicit function of time.

The sensitivity matrix can be obtained in two different ways: analytically, or numerically.

The analytical version is more desirable, as it will be more precise, and requires no iteration, thus saving time when running the codes. The algorithm was obtained using Maple software, giving as a result formulas that add up to more than 200 pages.

To write the formulas in Maple, a value for E_k (eccentric anomaly) is needed (see Table 2-1). The Kepler equation states that E_k is given by

$$M_k = E_k - e \sin(E_k) \quad (2-9)$$

E_k and can only be solved by iteration. Formula (2-10) was used instead (M_k can be computed directly inserting the broadcast values of M_0 and Δn in the formula, see Table 2-1) as it is a valid approximation for near circular orbits:

$$E_k = M_k - e \sin(M_k) \quad (2-10)$$

Given the extensive typing involved, and the impossibility to check the lengthy results by hand, before running the codes using the partial derivatives computed with Maple, a numerical version was implemented to check the results.

$$\frac{\partial f}{\partial p_i} \approx \frac{f(\mathbf{p} + dp_i) - f(\mathbf{p})}{dp_i} \quad (2-11)$$

For a given ephemeris, each element of the sensitivity matrix was obtained by reducing dp_i in (2-11) until the variation of the derivative was insignificant.

For some sample cases the formulas obtained from Maple, were corroborated numerically. The curves of the evolution of each derivative with time, always showed the

same shape for both, and the biggest discrepancy was four orders of magnitude smaller than the values of the partial derivative itself. Thus, with the analytical version of the sensitivity matrix considered validated, it was the only one used from there on.

In parallel to the sensitivity matrix computation, a full year of ephemerides from all satellites was used to quantify the distribution of daily variations for each ephemeris parameter. Daily (24 hour) ephemeris variations are directly relevant to LAAS monitors that are based on the use of prior ephemeris data as will be shown in Chapter III. These distributions correspond to 132,880 differences (using the 134,618 ephemerides mentioned in section 2.3), after eliminating the cases involving a satellite maneuver.

For the three parameters expressed with respect to a reference time, and that have a known rate (M_0 , i_0 and Ω_0) the value was adjusted using the three rates given in the ephemeris, extrapolated to 24 hours later, to compensate for the known secular effects.

Before completing the sensitivity analysis it is worth mentioning some interesting facts that emerge from the distributions.

- All distributions have a mean close to zero, except for differences in eccentricity. That could be explained by the fact that perturbations will in general make a near circular orbit drift to a more elliptical shape rather than the opposite, so in average, the distribution of the eccentricity adjustments to describe the orbit (not involving a maneuver) will be shifted to the positive side.
- Some parameter difference distributions have a shape that resembles a normal distribution (Figure 2.6), while others resemble a bi-modal distribution (Figure 2.3)

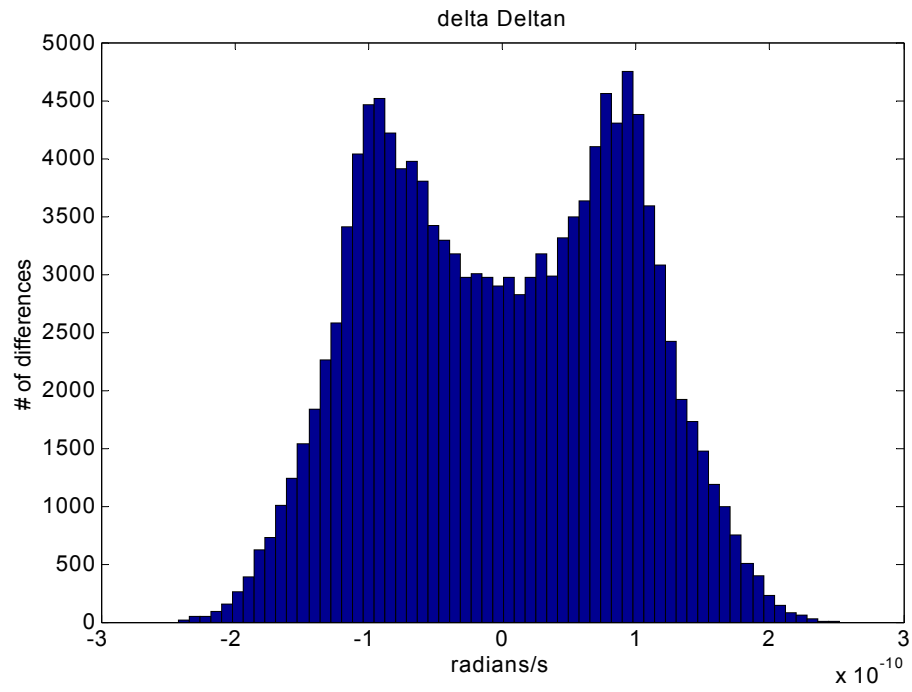
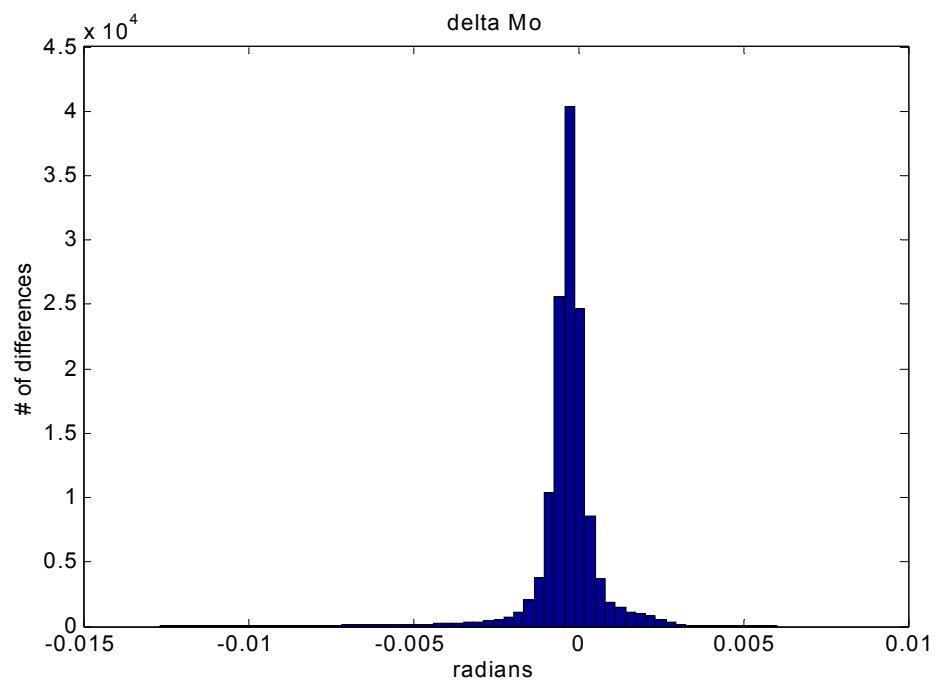
Figure 2.3 Differences in Δn 

Figure 2.4 Differences in Mean Anomaly

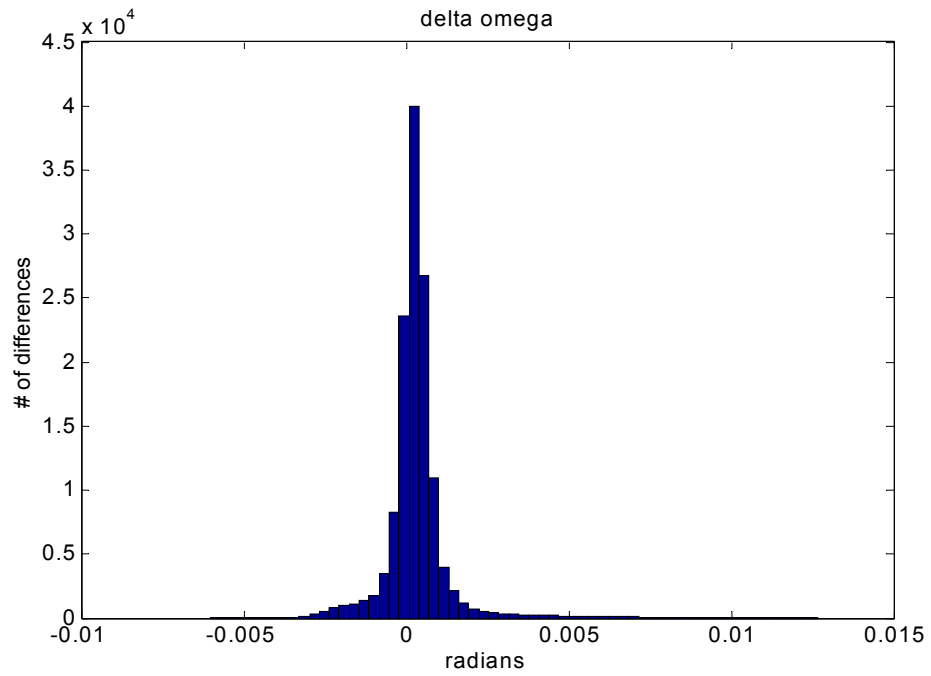


Figure 2.5 Differences in Argument of Perigee

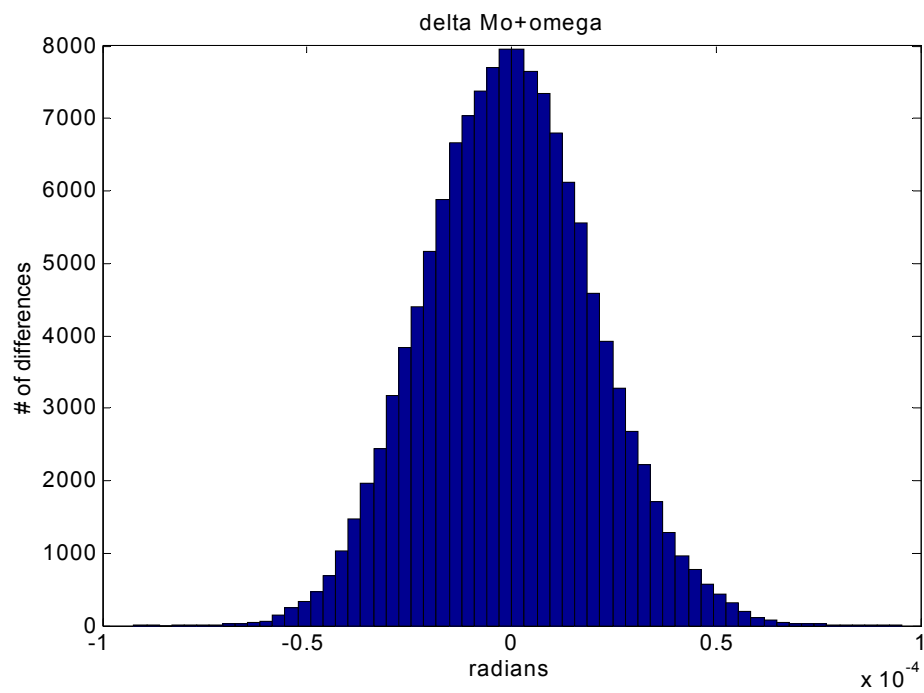


Figure 2.6 Differences in Mo+omega

- The distribution of the Mean Anomaly (Mo) is shifted to the left, and the distribution of the Argument of Perigee (ω) is shifted to the right. But when taken together, the distribution looks normal. (Figures 2.4 to 2.6), and the values are significantly smaller.

To complete the sensitivity analysis, the standard deviations of the daily parameter variations $\sigma(\delta p_i)$ are computed. Combining it with the corresponding elements of matrix A as shown in (2-8) it is possible to determine the 1-sigma satellite position variations $\sigma(\delta r_{pi})$ due to nominal daily variations on the individual ephemeris parameters. With i ranging from 1 to 15:

$$\sigma(\delta r_{pi}) = \left\{ \left(\frac{\partial f}{\partial p_i} \right)^2 + \left(\frac{\partial g}{\partial p_i} \right)^2 + \left(\frac{\partial h}{\partial p_i} \right)^2 \right\}^{.5} \sigma(\delta p_i) \quad (2-12)$$

Figure 2.7 shows an example, this results being typical and general. The time lapse is centered at toe, and the total interval is 24 hours. The actual time of broadcast of an ephemeris would be from $t=10$ to $t=12$ (toe) in the plot.

Several important things can be observed in this plot (the individual plots can be found in Appendix C for more detailed analysis).

- The sensitivity at toe is at its lowest point for parameter a and the three rates, diverging (linearly for a and Δn) before and after. For the rest of the parameters it shows a cyclic behavior.

- The position is most sensitive to errors in the angle formed by $Mo+\omega$, where it is of the order of 550 meters. This numbers were computed using the corresponding partial derivative for each parameter, but the standard deviation of the distribution of differences of the sum of both angles. This number is two orders of magnitude lower than the values

for the individual cases, and this is probably related to the method by which the two parameters are defined at the control segment, given that the closer to a circle the orbit is, the more difficult it is to distinguish what part of the total angle corresponds to each parameter. However, since it was well established how the sum behaves from day to day, it is beneficial to use this information in our analysis. The sensitivity using the individual σ 's for M_0 and ω is not plotted, as it is of no use.

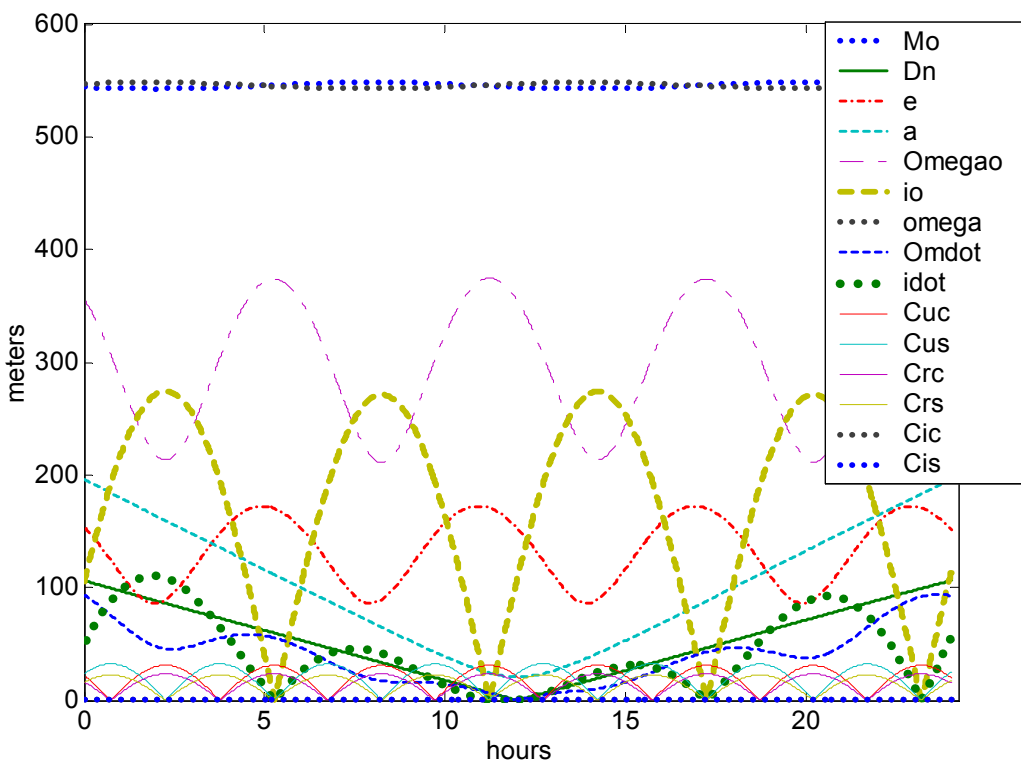


Figure 2.7 Position Sensitivity to Parameter Variations

- The least influential parameters are the six *C amplitudes*, specially C_{ic} and C_{is} , which look like a flat line at the bottom of the plot, and if seen in detail in the individual

plots in appendix C, never surpass the half a meter limit. This last fact is going to be advantageous in the implementation of the monitor as will be shown on Chapter IV.

2.4 Prior Work

To date, only a small amount of research effort has been focused on monitoring ephemeris anomalies. The two most significant proposed algorithms and their shortcomings are briefly described next.

Built-in LAAS Ephemeris Monitoring. In Category I LAAS ground systems, a standard set of monitoring procedures has been defined. They can be roughly categorized into three steps [Cha01]:

Step one – LGF receivers automatically confirm that the navigation messages of each satellite meet all requirements of the GPS SPS Interface Control Document [ICD-200]. This includes checking that satellite health bits and other health-related bits all indicate that message data is good.

Step two – Ephemeris/ephemeris check. After each changeover, the LGF compares satellite locations given by the old ephemeris and the new ephemeris to make sure that these two ephemeris messages are consistent. A checking standard of 250 m is set on the three-dimension satellite position difference.

Step three – Each broadcasted pseudorange correction and correction rate will be checked by LGF to confirm that they lie within $\pm 327.6\text{m}$ and $\pm 3.4\text{m/s}$, respectively. These limits represent not-to-exceed values for correction size.

DPR / DPDAS Method. An algorithm has been proposed by Shuichi Matsumoto, et al. [Cha01]. This algorithm uses the Differential Pseudorange Residual method (DPR)

to detect orbit error parallel to the LOS, and the Double Phase Difference with Ambiguity Search method (DPDAS) to detect orbit error perpendicular to the line-of-sight direction.

The first method does not consider the cases where the immediately previous ephemeris is not available: after a maneuver, or for a rising satellite.

For the second case, the orbit error detected by the DPR algorithm has no effect on LAAS DGPS users. The DPDAS algorithm is effective, but only when carrier phase cycle ambiguities can be correctly identified. The ambiguity search technique proposed in this regard is not sufficiently reliable.

In addition, for both methods, algorithm performance was not evaluated relative to LAAS integrity, availability or continuity requirements, making it difficult to quantify their efficiency.

The first two chapters described the shape of GPS satellite orbits, how accurately the ground segment can model them, the simplified formulas utilized by the users to compute satellite position, the values these parameters take, the distribution of their differences from day to day, and how sensitive the position estimation is to errors in each parameter. This was complemented with a description of the effect of these errors on LAAS users, the need of a monitor to detect them and the shortcomings of the methods proposed in prior works.

The following chapters deal specifically with the monitor algorithms, and can be summarized as an effort to determine two things. The first one is what data is necessary at the LGF to monitor the broadcast ephemeris and how to use it. The second one is the cost of implementing the proposed monitor in terms of current availability or necessary

changes in the LGF. To avoid availability loss, the algorithm has to be accurate and efficient. To avoid significant changes in the LGF, it has to be simple.

CHAPTER III

MONITOR BASED ON PREVIOUSLY VALIDATED EPHEMERIDES

There are two possible scenarios to be considered in the analysis. If there is no previously validated data available (for example after a maneuver), the monitor must be based on ranging measurements. This is the subject of Chapter IV. If we do have recent validated ephemerides, the monitor can be based on these. This is the subject of this chapter.

As each new ephemeris (with new or updated parameters) is received it must be validated prior to use. The last available validated ephemeris will usually be the previously transmitted one (two hours old). For a new rising satellite however, it will be the last ephemeris received at that particular LGF on the previous pass. The worst case will be for a pass that is shorter than 2 hours (24 hours difference between the two ephemerides). This limiting case is analyzed in this chapter.

Using the current ephemeris and time epoch k (where k is the relative time with respect to the toe of that ephemeris) the satellite position vector \mathbf{r}_k can be computed. Another satellite position, $\hat{\mathbf{r}}_k$ for the same k will be computed using our best estimate of the current ephemeris based on previous validated ephemerides.

3.1 The Test Statistic

The *Position Deviation Vector* is defined as:

$$\delta \mathbf{r}_i = \mathbf{r}_i - \hat{\mathbf{r}}_i \quad (3-1)$$

where i denotes an individual, as opposed to the whole set of vectors.

Under nominal conditions (no ephemeris anomalies) $\delta \mathbf{r}_i$ data may be collected over many days (in the results that follow we use the data set described in Chapter II) to generate empirical distributions and covariance matrices $\Sigma_{\delta \mathbf{r}}$.

As observed in the sensitivity analysis, parameter variations affect the position errors differently depending on the value of k , causing the covariance matrix to be an explicit function of time, consequently there will be a different covariance matrix $\Sigma_{\delta \mathbf{r}_k}$ for each relative time with respect to toe.

Before deriving the test statistic, it must be noted that there are different ways the monitor could be implemented. According to the present concept, and based on information volume and speed flow practical considerations, the LGF will only transmit the P -values along with the differential correction for each satellite in view. That is, the aircraft will receive no information on how significant the satellite position error found was, but only that it passed the monitor test. The user computation of the VPLe will thus be based on the maximum (non detectable) error rather than on the detected error. This explains why the derivation of the MDE starts from the specifications and will be independent of $\delta \mathbf{r}_i$.

Consider now a monitor that generates $\delta \mathbf{r}_i$ as discussed above, and has stored the covariance $\Sigma_{\delta \mathbf{r}_k}$ that corresponds to the fault free position differences (errors) for the particular method used to estimate $\hat{\mathbf{r}}_i$. Assuming the distribution of the errors for each position coordinate parameter is nearly Normal with:

$$\delta \mathbf{r} \sim N(\mathbf{0}, \Sigma_{\delta \mathbf{r}}) \quad (3-2)$$

Pre-multiplying $\delta \mathbf{r}$ by the constant matrix $\Sigma_{\delta \mathbf{r}}^{-1/2}$, a new variable χ can be defined:

$$\boldsymbol{\chi} = \boldsymbol{\Sigma}_{\delta\mathbf{r}}^{-1/2} \delta\mathbf{r} \quad (3-3)$$

Considering covariance matrices are symmetric:

$$\boldsymbol{\Sigma}_{\boldsymbol{\chi}} = \boldsymbol{\chi}\boldsymbol{\chi}^T = \boldsymbol{\Sigma}_{\delta\mathbf{r}}^{-1/2} \delta\mathbf{r} \left(\boldsymbol{\Sigma}_{\delta\mathbf{r}}^{-1/2} \delta\mathbf{r} \right)^T = \boldsymbol{\Sigma}_{\delta\mathbf{r}}^{-1/2} \delta\mathbf{r} \delta\mathbf{r}^T \boldsymbol{\Sigma}_{\delta\mathbf{r}}^{-1/2} = \mathbf{I}_{(3)} \quad (3-4)$$

Then

$$\boldsymbol{\chi} \sim N(0, \mathbf{I}_{(3)}) \quad (3-5)$$

A scalar test statistic can now be defined:

$$s = \delta\mathbf{r}_i^T \boldsymbol{\Sigma}_{\delta\mathbf{r}_k}^{-1} \delta\mathbf{r}_i \quad (3.6)$$

Given that $\mathbf{s} = \boldsymbol{\chi}_i^T \boldsymbol{\chi}_i$, under normal conditions it will be approximately Chi-Square distributed with 3 degrees of freedom. The test statistic will be compared to a threshold T to detect an anomalous ephemeris. The threshold, in turn, is defined to ensure a fault-free alarm probability that is consistent with the system availability requirements. In [Pul02] it is shown that for rising satellites a fault free alarm probability of 1.9×10^{-4} is sufficient for LAAS Category I. To determine the threshold, the value for a three degrees of freedom Chi-Square distribution that gives a cumulative probability $\text{Pr} = 1 - 1.9 \times 10^{-4}$ must be found. The corresponding formula is:

$$P_r = \int_0^T \frac{t^{(v-2)/2} e^{-t/2}}{2^{v/2} \Gamma_{(v/2)}} dt = \frac{1}{\sqrt{2\pi}} \int_0^T t^{1/2} e^{-t/2} dt \quad (3.7)$$

with:

v =degrees of freedom (3)

Γ = the Gamma function.

The resulting value is $T = 4.445637^2$ (Fig. 3.1)

T is then the most stringent threshold that complies with the current LAAS availability levels for the fault free analysis.

In case of an ephemeris anomaly, the test statistic will have a nearly Non-Central Chi Square distribution. It is necessary to determine the minimum non-centrality parameter (λ) for such a distribution that is consistent with the required integrity constraints for LAAS Cat I. It has been established in prior work by Shively that a Missed Detection probability $\Pr(\text{MD})=10^{-3}$ is sufficient to meet the specification[Shi01].

The Non Central Chi Square cumulative distribution function is given by:

$$F(S|v, \lambda) = \Pr(\text{MD}) = 10^{-3} = \sum_{j=0}^{\infty} \left(\frac{\left(\frac{1}{2}\lambda\right)^j}{j!} e^{-\frac{\lambda}{2}} \right) \Pr[\chi_{v+2j}^2 \leq S] = \sum_{j=0}^{\infty} \left(\frac{\left(\frac{1}{2}\lambda\right)^j}{j!} e^{-\frac{\lambda}{2}} \right) \Pr[\chi_{3+2j}^2 \leq T] \quad (3.8)$$

The value obtained is $\lambda=7.3618^2$ (Fig. 3.1).

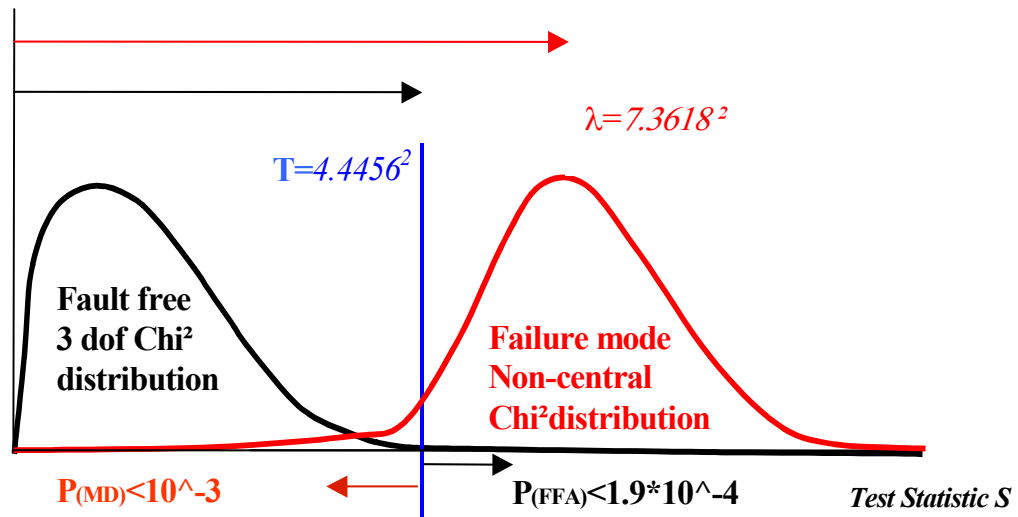


Figure 3.1: Threshold and Non-Centrality Parameter for S

3.2 The Minimum Detectable Error

Consider now a satellite position error $\delta \mathbf{r}_o$ caused by an ephemeris failure. The ephemeris monitor at the LGF will compare T with the value of the test statistic S corresponding to the total position error:

$$T \leq \delta \mathbf{r}_{\text{total}}^T \Sigma_{\delta \mathbf{r}_k}^{-1} \delta \mathbf{r}_{\text{total}} \quad (3-9)$$

with:

$$\delta \mathbf{r}_{\text{total}} = \delta \mathbf{r} + \delta \mathbf{r}_o \quad (3-10)$$

$\delta \mathbf{r}$ is the nominal position prediction error (the i subscript has been dropped). Depending on its orientation, it could compensate the ephemeris error, giving a smaller value of S . This can result in a missed detection. From the analysis in the previous section, to guarantee a misdetection smaller than the specified constraint (10^{-3}); $\delta \mathbf{r}_o$ has to be such that

$$\lambda \leq \delta \mathbf{r}_o^T \Sigma_{\delta \mathbf{r}_k}^{-1} \delta \mathbf{r}_o. \quad (3-11)$$

There is an infinite set of position error vectors $\delta \mathbf{r}_o$ that will give as a result λ in (3-11). The vector $\delta \mathbf{r}_o$ of maximum length for which the integrity specification can be met defines the MDE.

In the position domain, for a given $\delta \mathbf{r}_o$, the probability of $\delta \mathbf{r}_{\text{total}}$ being in a certain region of space is defined by an ellipse centered at $\delta \mathbf{r}_o$, and with a limiting surface consisting of all vectors $\delta \mathbf{r}_{\text{total}}$ that give a constant value of test statistic S :

$$S = \delta \mathbf{r}_{\text{total}}^T \Sigma_{\delta \mathbf{r}_k}^{-1} \delta \mathbf{r}_{\text{total}} \quad (3-12)$$

These surfaces are represented by the three small ellipses in Figure 3.2 for three different vectors $\delta \mathbf{r}_o$ that comply with (3-11). It can be seen in the same figure that the biggest value of $\delta \mathbf{r}_o$ that will give a $\delta \mathbf{r}_{total}$ distribution that meets the integrity specification corresponds to the one in the direction of the ellipsoid's major axis.

To find this maximum value of $\delta \mathbf{r}_o$, an eigenvalue decomposition is used. Starting from the limit equation (3-11), and making:

$$\lambda = \delta \mathbf{r}_o^T \mathbf{V}^T \mathbf{D}^{-1} \mathbf{V} \delta \mathbf{r}_o \quad (3-13)$$

where \mathbf{D}^{-1} is a diagonal matrix whose non-zero elements are the eigenvalues of $\Sigma_{\delta \mathbf{r}_k}^{-1}$. Since \mathbf{V} is an orthonormal modal matrix of $\Sigma_{\delta \mathbf{r}_k}^{-1}$:

$$|\mathbf{V} \delta \mathbf{r}_o| = |\delta \mathbf{r}_o^T \mathbf{V}^T| = |\delta \mathbf{r}_o| \quad (3-14)$$

As stated above, the maximum $\delta \mathbf{r}_o$ corresponds to an error aligned with the ellipse's major axis, which corresponds to the direction of the eigenvector with minimum eigenvalue for $\Sigma_{\delta \mathbf{r}_k}^{-1}$.

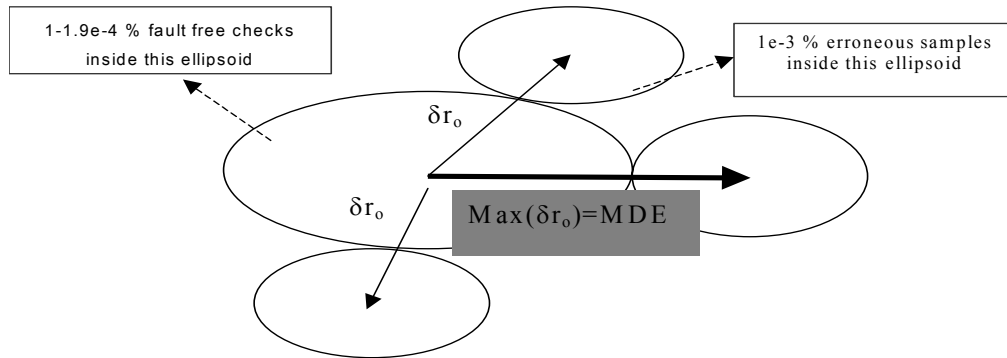


Figure 3.2: Fault Free and Failure $\delta \mathbf{r}_{total}$ Probability Space

In that case:

$$\lambda = |\max \delta \mathbf{r}_o|^2 \min(\text{eig} \Sigma_{\delta \mathbf{r}}^{-1}) = |\max \delta \mathbf{r}_o|^2 \{\max(\text{eig} \Sigma_{\delta \mathbf{r}})\}^{-1} \quad (3-15)$$

finally obtaining the MDE as:

$$\text{MDE} = |\max \delta \mathbf{r}_o| = \sqrt{\lambda \max(\text{eig} \Sigma_{\delta \mathbf{r}})} \quad (3-16)$$

3.3 Satellite Position Estimate

The values obtained in the previous section come from applying the system constraints to theoretical statistics formulas. Now the actual data that concerns this work has to be introduced. In order to do that, the way to estimate the satellite position $\hat{\mathbf{r}}_k$ must be defined. $\hat{\mathbf{r}}_k$ will always be computed using the *GPS orbit model*, so the different methods of estimation will differ only in the way the ephemeris parameters are estimated.

To make the notation more practical some definitions are made based on the nature of the *Broadcast Parameters*.

$\mathbf{P}=[\Delta n \ e \ a \ \omega \ \Omega \ \dot{\omega} \ \dot{\Omega} \ Cus \ Cuc \ Crs \ Crc \ Cis \ Cic]^T$, are the parameters from vector \mathbf{p} that invariant during the time of ephemeris validity.

$\mathbf{P}_0=[M_0 \ i_0 \ \Omega_0]^T$, are the parameters referenced to the toe, that need to be permanently adjusted with the rates.

The subscript expresses time: \mathbf{P}_k or \mathbf{P}_k means at time k (relative to toe), \mathbf{P}_{k-1d} is at k minus one solar day, and \mathbf{P}_{k-2d} is at k minus two solar days, etc.

The error between the actual satellite position and the estimate can be modeled as a random variable, allowing the use of statistical tools and integrity related quantifications.

But by studying the actual parameter behavior with time, the prediction can be made more accurate, thus reducing the estimate error variance. As an example let's observe the values for parameter a for one satellite over 45 days in Figure 3.3.

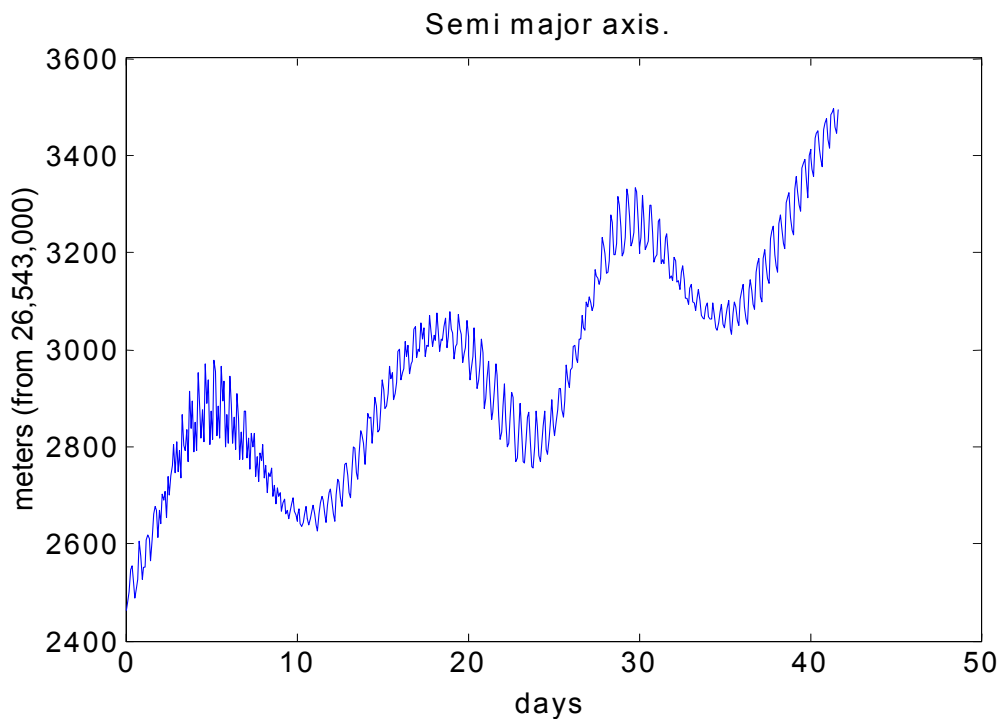


Figure 3.3 Values of Parameter a With Time

To better observe how this pattern can help predict the value for the first ephemeris at rise-time, short period effects are removed by taking 24 hours intervals between readings (Fig 3.4).

In appendix D the curves for all parameters are shown. These plots show that using recent validated values will be more precise than using the mean, or the theoretical GPS as an estimate of the parameters.

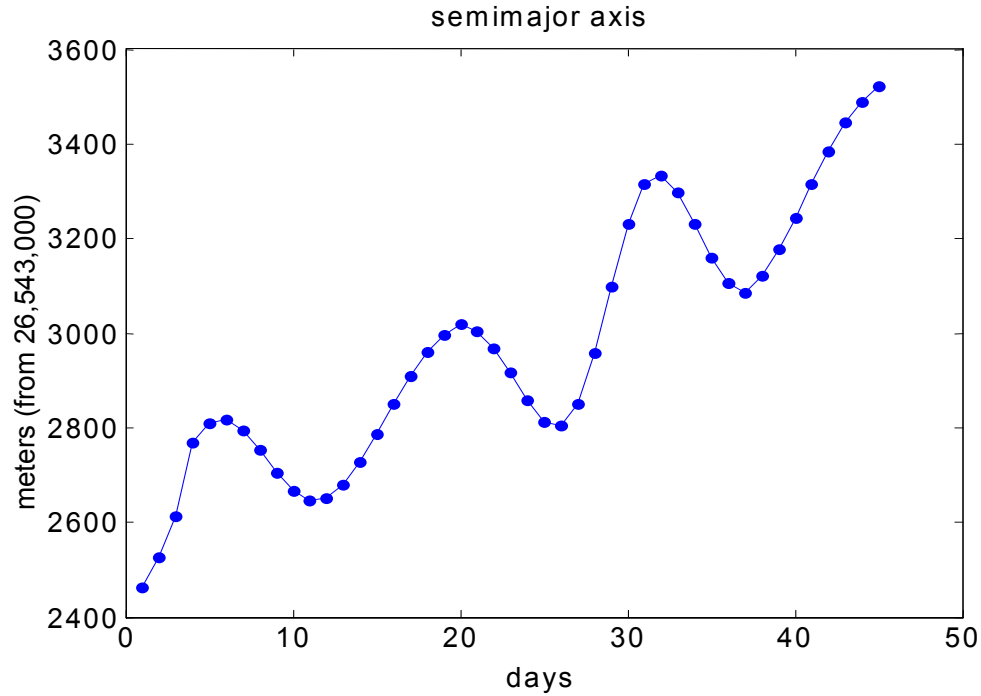


Figure 3.4 Values of Parameter a at 24 hs Intervals

Zero Order Hold (ZOH): The first estimation method considered assumes the previous ephemeris is broadcasted during the validity time of the *Ephemeris To Be Validated* (Etbv), thus the estimated ephemeris parameters $\hat{\mathbf{P}}$ and $\hat{\mathbf{P}}_0$ are:

$$\hat{\mathbf{P}}_k = \mathbf{P}_{k-1d}, \quad \hat{\mathbf{P}}_0^j = \mathbf{P}_0^j + \text{rate}_{k-1d}^j \times 24 \text{ h} \quad (3-17)$$

where j corresponds to each of the three different parameters conforming \mathbf{P}_0 and the corresponding rate for each one (included in \mathbf{P}). The actual updating process is slightly more complicated, and the formulas used can be found in Appendix E.

First Order Hold (FOH): The only cases in which there will only be one previous pass of data available, is when there has been a maneuver. [Note: The orbit's period is 12 *sidereal* hours and ephemeris changeovers are every 2 *solar* hours, so the 4 minutes/day time difference might in certain cases cause a 24 h old or a 48 h old match not be found for

certain LGF locations]. So in general two or more days of validated ephemerides will be available.

The prediction model is:

$$\hat{\mathbf{P}}_k = \mathbf{P}_{k-1d} + (\mathbf{P}_{k-1d} - \mathbf{P}_{k-2d}) \tag{3-18}$$

$$\hat{P}o_k^j = P o_{k-1d}^j + [rate_{k-1d}^j \times 24 \text{ h} + (P o_{k-1d}^j - (P o_{k-2d}^j + rate_{k-2d}^i \times 24 \text{ h}))] \tag{3-19}$$

Figure 3.4 shows ZOH and FOH parameter prediction concepts schematically.

These are the only two methods utilized to generate the results presented in this chapter.

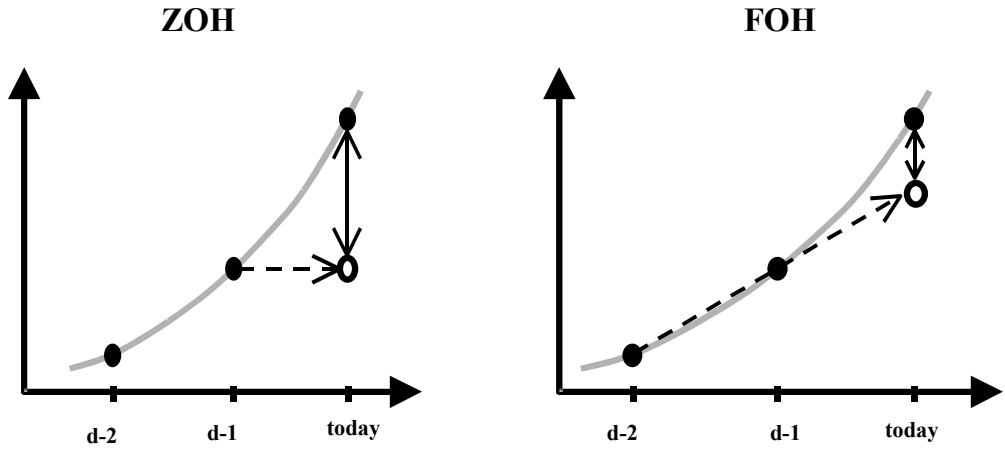


Figure 3.5 ZOH and FOH Parameter Prediction Concepts

To better visualize the advantages of a FOH, it is useful to observe the plots of the differences in parameter values from day to day. Figure 3.6 is an example corresponding to differences in the value of the inclination angle. The plots for all parameters can be found in appendix F. The FOH assumes the difference in parameter value remains

constant from the previous day. These (plotted) values are equivalent to the term in brackets in (3-19)

Comparing with the ZOH (where the prediction of the plotted value is always zero), this method will be generally more accurate. The exception is when the value crosses the zero line, or is approaching it. The figure shows the FOH prediction will always be better than the ZOH except for the 3 marked cases. So in a statistical sense the FOH prediction is expected to be more accurate.

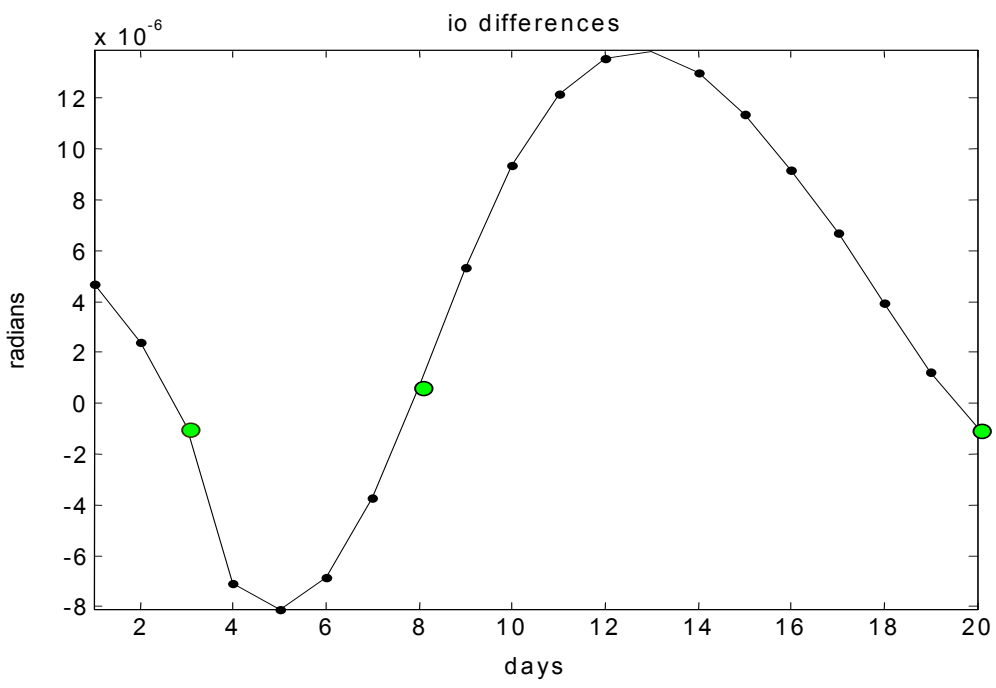


Figure 3.6 24hs Differences in Value of Inclination Angle

In Figure 3.7, the position errors using one method and the other for the same set of data can be appreciated.

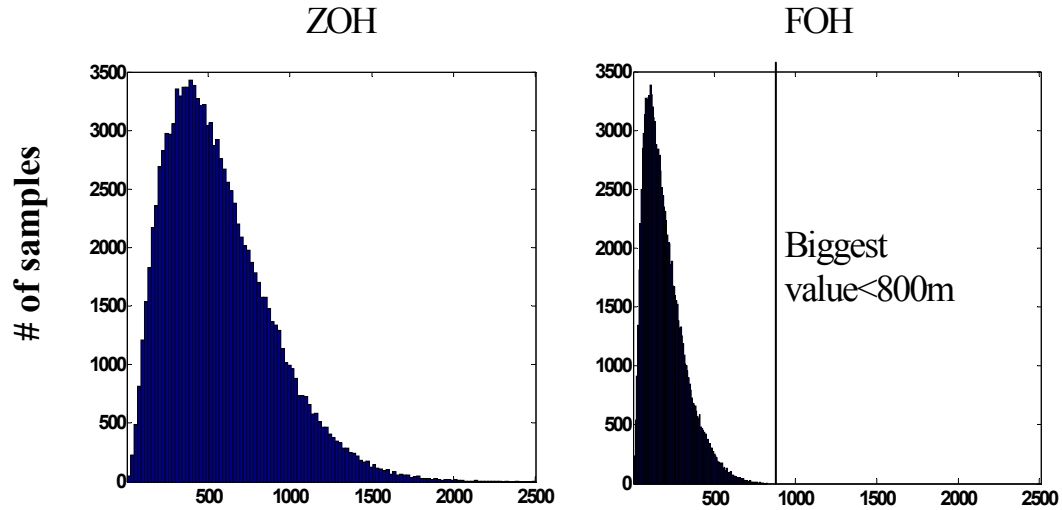


Figure 3.7 ZOH and FOH Position Error Distribution

Other Methods: Two other prediction methods were considered. They were not used to generate the final results in this work so they are described only briefly. The first one is a Second Order Hold (SOH). Assuming the variation of the rate of change of the parameters is constant:

$$\hat{\mathbf{p}} = \mathbf{p}_{k-1d} + [(\mathbf{p}_{k-1d} - \mathbf{p}_{k-2d}) + \{(\mathbf{p}_{k-1d} - \mathbf{p}_{k-2d}) - (\mathbf{p}_{k-2d} - \mathbf{p}_{k-3d})\}] = 3\mathbf{p}_{k-1d} - 3\mathbf{p}_{k-2d} + \mathbf{p}_{k-3d}$$

The results were significantly better. For example for the prediction of $\text{Mo}+\omega$, the standard deviation of the error from truth was reduced to $\sigma=2.65\text{e-}6$ radians (compared with $\sigma=4.33\text{ e-}6$ for the FOH and $\sigma=1.16\text{ e-}5$ for the ZOH); but given that an extra day of data is necessary, and FOH results are sufficient to meet the requirements (as will be shown shortly) the SOH analysis was not further pursued.

Another model initially considered was a sinusoidal one. Assuming an amplitude and a frequency could be determined for each parameter, the possibility of predicting the

parameter values in this way was studied. The study was stopped for the same reasons, plus the questionable validity of the assumed model for some parameters.

3.4 Results

For the same 2002 set of data specified before, the distributions of test statistic S at toe (equivalent to $k=0$) for the ZOH and FOH position estimation methods are shown in Figure 3.7. (Plots for other values of k can be found in appendix G).

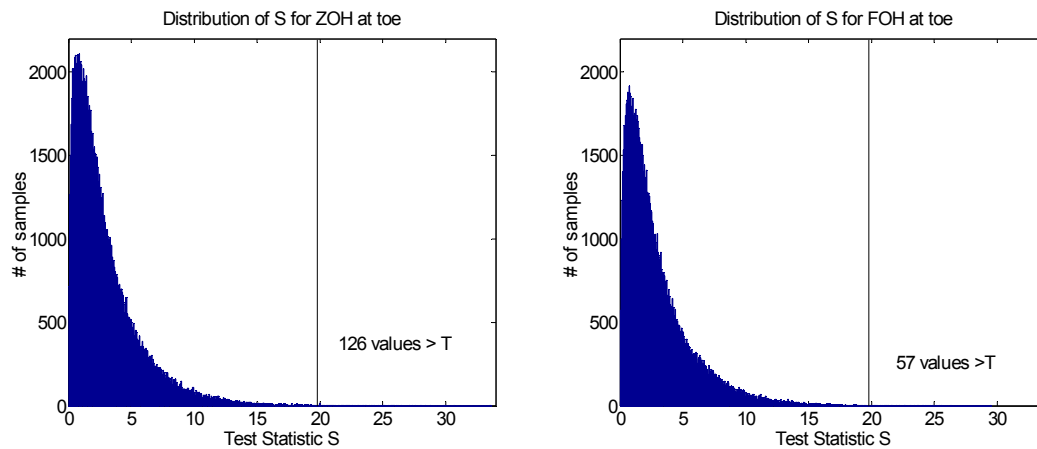


Figure 3.8 Distribution of Test Statistic S

For this set of samples, the allowable number of values bigger than T is given by:

$$\text{Num} = P_{\text{FF}} \text{Samples} = 1.9e^{-4} 117,380 = 22.3 \approx 23 \quad (3.20)$$

Num represents the number of FF cases that can fail the test without affecting availability for this set of data. From plot 3.8 it can be observed that the number is bigger in both cases (126 for the ZOH and 57 for the FOH). This is caused by the fact that the distribution of the test statistic S is only approximately Chi Square distributed. To avoid

this problem, the covariance matrices must be inflated, reducing the number of FF alarms below Num . The adjusted test statistic will be:

$$s = \delta \mathbf{r}^T (C \Sigma_{\delta \mathbf{r}_k})^{-1} \delta \mathbf{r} \quad (3-21)$$

with C being the necessary inflation factor.

To verify that the assumed Chi^2 distribution being used is conservative, the Cumulative Distribution Function (CDF) of the data must be compared to the theoretical Chi^2 distribution CDF for the same values of S .

All plots observed during this analysis have the general shape of Figure 3.9, in which it can be observed that the dashed curve of the theoretical CDF at the bottom does not surpass the value of the upper empirical curve. The region of the tail on the right has to be observed in detail to make sure that for all values of S in the data set:

$$\frac{L_s}{T_0} > \frac{1}{\sqrt{2\pi}} \int_0^s t^{1/2} e^{-t/2} dt \quad (3.22)$$

where L_s is the number of samples smaller or equal to S , T_0 is the total number of samples (in this case $T_0=117,380$), and the right hand side comes from (3-7). This guarantees that the probability of a sample having a value bigger than S is always smaller than $P_{(s)}$ theoretical, and thus the data is safely overbound.

Figures 3.10 and 3.11 show that the conditions of (3-22) are met for ZOH by inflating the covariance matrix with a factor of 1.356, while $C=1.19$ is good enough to overbound the FOH data CDF. (Similar plots for k different than 0 can be found in appendix H).

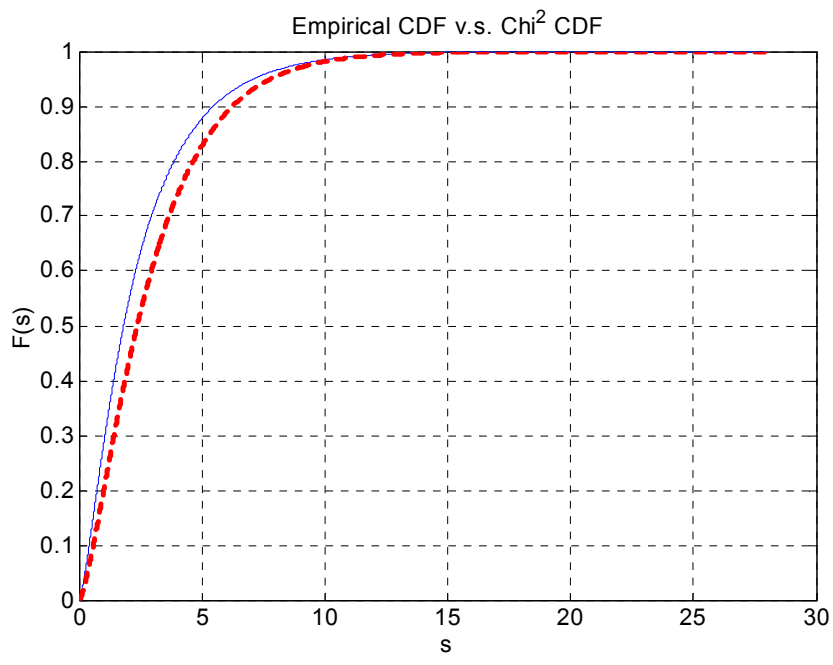


Figure 3.9 CDF of Test Statistic S

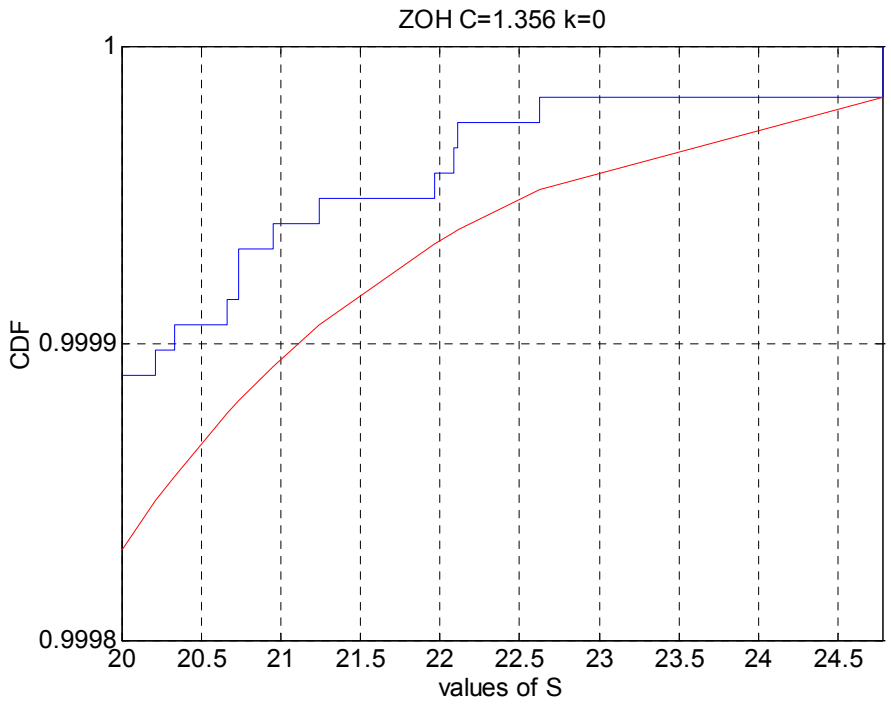


Figure 3.10 Tail overbounding of CDF for ZOH

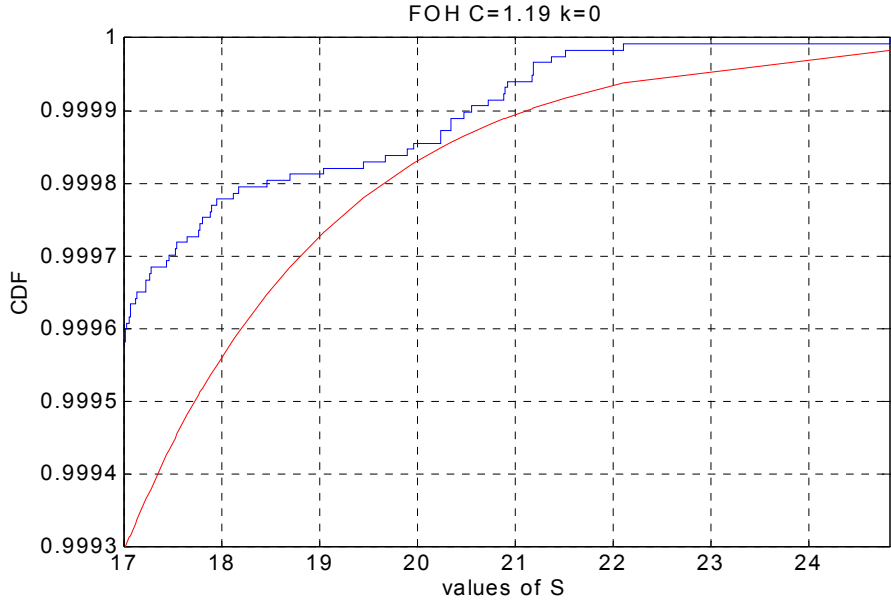


Figure 3.11 Tail overbounding of CDF for FOH

It is possible now to compute the MDE using formula (3.16), by using the modified covariance ($C\Sigma_{\delta_k}$). The results, for three representative epochs of ephemeris broadcast (beginning, middle and end) are presented in Figure 3.12.

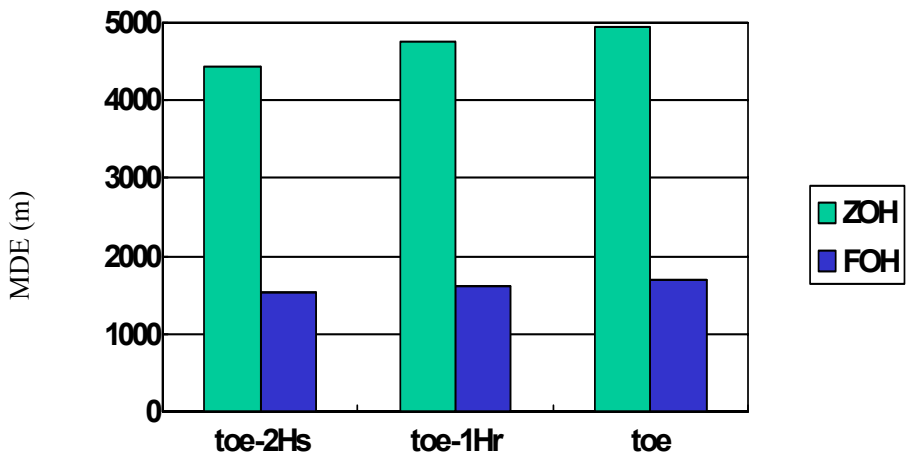


Figure 3.12 Minimum Detectable Error Results

At $k=0$: $MDE_{ZOH} = 4984$ m, and $MDE_{FOH} = 1744$ m.

Consistent with all the computations shown up to now, the worst results are at $k=0$. [Note: A detailed analysis of this fact has not been done in this work, but this result is not unexpected. Considering that both estimation methods (ZOH and FOH) are based on comparing previous ephemerides with the **Etbv**, the effects of orbit model errors of the three rate parameters will affect the estimation differently at different k 's. For the ZOH, the more favorable time will be midpoint between the two ephemerides, and worst at the two toe's. For the FOH it is more complicated to evaluate, but it is still obvious that at $k=0$ the effect will be larger than at $k=-2$ h].

Even though the monitor will most likely be applied in a unified way for all satellites, the MDE was also computed on an individual basis for each SV with the same methodology. The results for $k=0$ are shown in Figure 3.13. In general higher values of MDE correspond to larger nominal orbit eccentricities.

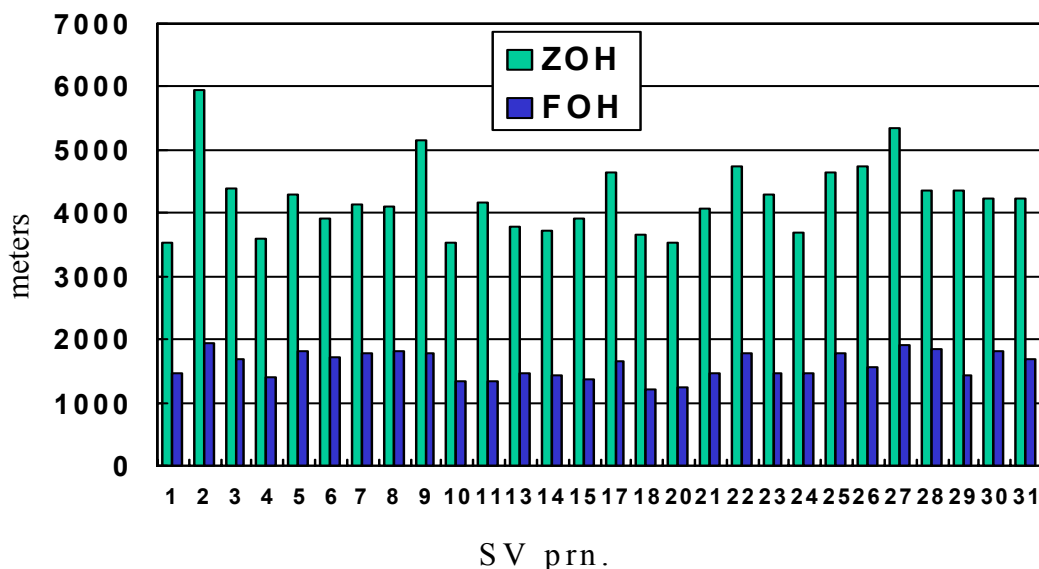


Figure 3.13 MDE values for individual SV at $k=0$

Given the 3500 m desired maximum MDE value stated in Chapter I, it is clear that the FOH is sufficient to ensure LAAS availability, whereas the ZOH is not. The principle drawback of the FOH is that it requires two prior days of ephemerides, in contrast to the ZOH, which needs only one. However this is not a significant liability because two prior days are always available except after a station-keeping maneuver. Such maneuvers happen on average less than once per year per satellite. In this case, on the second day following a maneuver, the FOH implementation cannot be used since only one prior day's worth of ephemeris is available.

3.5 Experimental Verification

To verify the MDE results experimentally, the following process was followed:

By observing the distribution of the magnitudes of the elements of the sensitivity matrix (2-8) for all ephemerides, approximate values for errors in each parameter were found, such as to cause errors in the satellite position of a magnitude similar to the derived MDE values. For each ephemeris parameter i :

$$\delta p_i \approx \frac{\text{MDE}}{\left(\text{mean} \left(\frac{\partial X}{\partial p_i} \right) + \sigma \left(\frac{\partial X}{\partial p_i} \right) \right)} \quad (3-23)$$

For all ephemerides in the set of data, position coordinates were generated with the formulas of Table 2.1 but, introducing (one parameter at a time) error δp_i , (with $k=0$), and then comparing it with the fault free ephemeris, to compute a position error:

$$\Delta \mathbf{r} = \mathbf{r} - \mathbf{r}_{\text{faulty}} = \mathbf{r}(\mathbf{p}, \text{toe}) - \mathbf{r}(\mathbf{p}, p_i + \delta p_i, \text{toe}). \quad (3-24)$$

An estimated position error was also computed:

$$\Delta \mathbf{r}_{\text{est}} = \mathbf{r}_{\text{est}} - \mathbf{r}_{\text{faulty}} = \mathbf{r}(\mathbf{p}_{\text{est}}, \text{toe}) - \mathbf{r}(\mathbf{p}, p_i + \delta p_i, \text{toe}) \quad (3-25)$$

with $p_{est}=p_{ZOH}$ or p_{FOH} depending on the estimation method used.

By introducing Δr_{est} in place of δr in (3.6), and comparing the resulting value of s with the threshold T , the detection or misdetection of the position error is determined.

Analyzing the relation between the misdetections and the values of Δr for those cases gives an idea of the correctness of the MDE values derived in this chapter.

Table 3.1

Missed Detection Experimental Verification Results

Estimation Method	Total # of erroneous positions generated	Errors > MDE	Magnitude of Maximum Undetected Error(MUX)	Undetected Errors >MDE	# Undetected errors between MUX and 2xMDE-MUX
ZOH	5,634,420	3,367,151	5035m	9	14/115,718
FOH	5,634,420	1,117,901	1763m	2	7/41,442

Table 3-1 shows results that agree with the derived MDE values.

For the ZOH, the highest undetected error was 5035 meters, 51 meters larger than the MDE value. To get a more complete idea of the rate of missed detection on the MDE value borderline, the bin with values between MDE-51 meters and MDE+51 meters was observed. The total number of undetected errors is in the last column along with the number of total position errors in that bin. Only 14 out of 115,718 position errors were misdetections.

Similar analysis was performed for the FOH, with the maximum undetected error being 1763 m, 19 meters above the MDE. In the bin between MDE-19 m and MDE+19 m, 7 out of 41,442 errors were not detected.

In both cases the percentage is significantly below the allowed 10^{-3} integrity constraint. That is a significant comparison, since part of the samples in that bin are inside the fault free ellipse, and the part outside of it includes 100% of undetected errors larger than the MDE.

CHAPTER IV

MEASUREMENT BASED MONITOR

After a scheduled maneuver, the orbit parameters change significantly, making previous ephemerides useless for validation. In this event, a potential solution is to verify the post-maneuver broadcast ephemeris directly by the use of LGF code and carrier measurements. To verify whether or not such an approach is effective and realizable, it is assumed that a whole day is available immediately following the maneuver (during which corrections will not be broadcasted) to verify the current ephemeris. Once verified, this ephemeris may be used on the following day in the manner described in the previous chapter.

There is also another need for this implementation. The methods described in Chapter III assume that previously validated ephemerides are error free. The likelihood of a hazardous ephemeris error not being detected by the GPS Control Segment for a full day (minimum time that will elapse for an ephemeris to be used in the ZOH or FOH methods for a rising satellite) is very low, but as long as a limiting number is not provided by the DoD this detection function should be included at the LGF. In this case the measurement-based monitor would not only be used for after maneuver validation, but on a daily basis for all satellites.

The basic idea behind such a monitor implementation is to fit the LGF ranging measurements to an orbit model and then compare the satellite positions generated with this model to the positions generated using the broadcast ephemeris (E_{TBV})

4.1 The Orbit Model

Selection of the proper orbit model for the monitor is based on a tradeoff between complexity and accuracy. In this section, the accuracy of four different models is presented by way of a representative example. In each case, fault-free satellite position data for an entire satellite pass was fit via least squares to the candidate models, and the residual position errors (model fit minus true position) were generated.

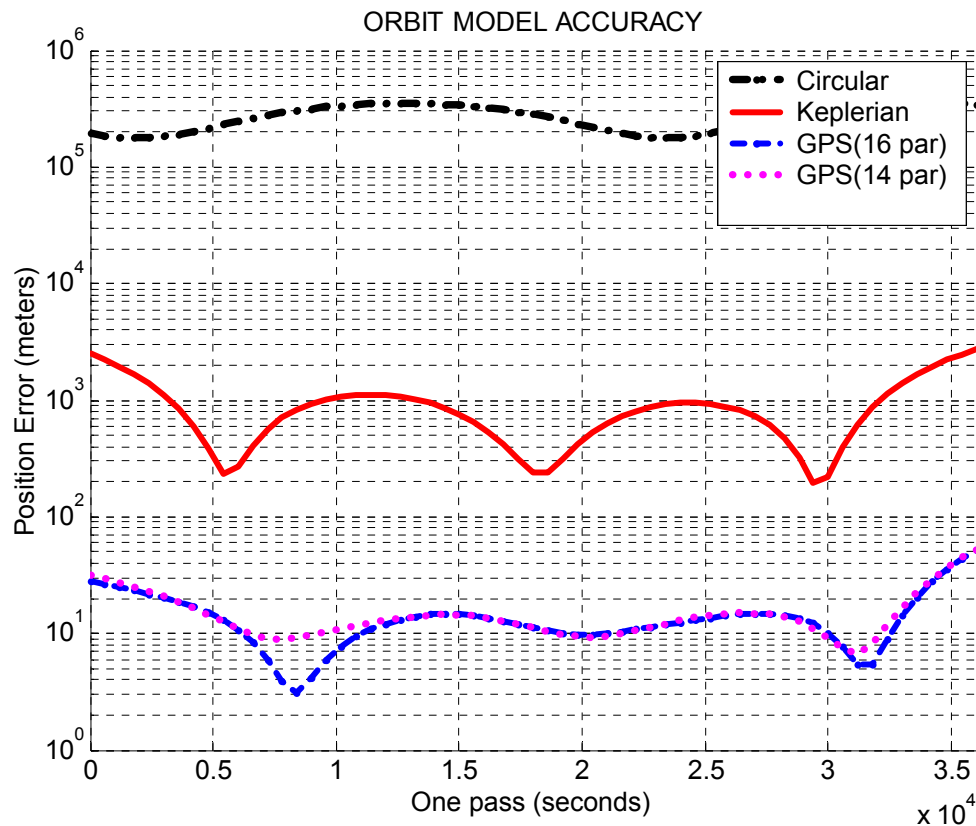


Figure 4.1: Satellite Position Residuals for Different Orbit Models

The *Circular Orbit* model is shown for comparison, given that it is the simplest possible. The six-parameter *Keplerian Orbit* model has been proposed in previous works

as suitable, and is the second candidate, as it is the simplest after the circular one. As can be seen in figure 4.1, this model is not acceptable, since it has errors of the same magnitude as the MDE values needed.

The third model is the *GPS orbit* model. It has already been stated in Chapter I that this model is very precise; but what needs to be determined is if its error when utilized for the whole satellite pass (instead of the normal 2 hours period of broadcast) is still small enough for this implementation. It can be observed in figure 4.1 that the deviation from the true position is comfortably below 100 meters, with maximum values close to 60 meters. This is sufficiently good for the needs of this work because it is much smaller than the required MDE.

Using the knowledge of the sensitivity analysis from Chapter II, one last model is considered. It consists of the *GPS orbit* model, simplified by omission of the two least influential parameters (C_{is} and C_{ic}). Figure 4.1 shows the results are still accurate enough. This slightly simpler model has the advantage of having two fewer parameters to estimate using the ranging data. This model is the one utilized in the rest of this chapter. [Note: In subsequent sections of this Chapter, ephemeris parameters vector \mathbf{p} refers to the reduced parameter set without amplitudes C_{ic} and C_{is}].

4.2 LGF Measurements

Two measurement types available at the LGF are analyzed for use in orbit estimation. These are the standalone pseudorange residual (the broadcast pseudorange correction), and the differential carrier phase across the LGF reference receiver baselines.

(a) The *standalone pseudorange residual* (z_k^p) measures the orbit error over time (k) projected into the satellite's line-of-sight direction (\mathbf{e}_k).

It is computed by subtracting the pseudorange measurement defined in (1-5) from the computed antenna-satellite range magnitude (the estimate of the range) $\hat{R} = |\hat{\mathbf{r}} - \mathbf{r}_u|$ where $\hat{\mathbf{r}}$ and \mathbf{r}_u are the satellite and the LGF antenna position vectors in ECEF coordinates and $\hat{\mathbf{r}}$ is computed using the ephemeris parameters.

$$z_k^p = \hat{R}_k - \rho_k \quad (4-1)$$

The computed magnitude will only be affected by satellite position errors ($\delta\mathbf{r}_k$) in the direction of the LOS unit vector \mathbf{e}_k [Cha01], while the magnitude of the measured pseudorange will differ from the actual range R_k by the measurement noise (v_k^p).

$$z_k^p = R_k + \mathbf{e}_k^T \delta\mathbf{r}_k - (R_k - v_k^p) \quad (4-2)$$

where the noise was arbitrarily given a negative sign for notation convenience. Replacing the satellite position error with its linearized version from (2-8) the final expression for the measurement is:

$$z_k^p = \mathbf{e}_k^T \mathbf{A}_{(p,k)} \delta\mathbf{p} + v_k^p \quad (4-3)$$

(b) The second measurement type, the *differential carrier residual* (z_k^ϕ), measures orbit errors orthogonal to the line-of-sight and projected into the known direction of the baselines formed by the antenna pairs in the LGF.

The basic components of this measurement are the standalone carrier measurements defined in (2-2) (ϕ)

By differencing the measurement from antenna ‘‘A’’ (ϕ_A) with the measurement from antenna ‘‘B’’ (ϕ_B) at each time, the single difference carrier measurement is obtained:

$$\Delta\phi\lambda_k = R_{Ak} - R_{Bk} + c[\delta t_{uAk} - \delta t_{uBk}] + (N_A - N_B)\lambda + v_{SDk} \quad (4-4)$$

The single difference noise v_{SD} is larger than v_{ϕ} but the total error will be smaller given the common error sources (I, T, etc.) eliminated by differencing.

A second difference is made to eliminate the remaining significant common error, the clock offset between the two receivers. Subtracting the single difference carrier to a satellite “ α ” ($\Delta\phi_{\alpha k}$), from one to a satellite “ β ” ($\Delta\phi_{\beta k}$) the *Double Difference Carrier Measurement* ($\Delta^2\phi$) is obtained:

$$\Delta^2\phi_k\lambda = R_{A\alpha k} - R_{B\alpha k} - R_{A\beta k} - R_{B\beta k} + (N_{A\alpha} - N_{B\alpha} - N_{A\beta} + N_{B\beta})\lambda + v_{DD\phi k} \quad (4-5)$$

The noise of this measurement $v_{DD\phi}$ (from multipath and receiver noise) will again be larger than the single difference noise v_{SD} but it is the sole component of the measurement error.

The individual values of the cycle ambiguities (Ns inside the parenthesis) are of no interest for the monitor that only needs the sum, itself an integer N, giving the final formula:

$$\Delta^2\phi_k\lambda = R_{A\alpha k} - R_{B\alpha k} - R_{A\beta k} - R_{B\beta k} + N\lambda + v_{DD\phi k} \quad (4-6)$$

The measurement residual used in the algorithm is:

$$z_k^\phi = [(\hat{R}_{A\alpha k} - \hat{R}_{B\alpha k}) - (\hat{R}_{A\beta k} - \hat{R}_{B\beta k})] - \Delta^2\phi_k\lambda \quad (4-7)$$

In this case, the magnitude of the range estimates double difference residual will only be affected by the projection of satellite position errors orthogonal to the LOS unto the antennas baseline [Cha01]. Canceling the true double differences ranges on the right hand side, and again expressing the satellite position error in linearized version, the residual is:

$$z_k^\phi = \ell \frac{\mathbf{B}^T \mathbf{F}_k}{R_k} \mathbf{A}_{(p,k)} \delta \mathbf{p} + N \lambda + v_k^\phi \quad (4-8)$$

were:

ℓ is the baseline length

\mathbf{B} is the baseline unit vector, and

$\mathbf{F}_k = \mathbf{I}_{(3)} - \mathbf{e}_k \mathbf{e}_k^T$ (This term extracts the position error component orthogonal to the LOS).

4.3 Covariance Analysis and the MDE

Consider a *Residuals Vector* (\mathbf{Res}), related to a set of unknown parameters $\delta \mathbf{P}_{ar}$ by the formula:

$$\mathbf{Res} = \mathbf{H} \delta \mathbf{P}_{ar} + \mathbf{v} \quad (4-9)$$

\mathbf{H} is an observation matrix that linearly relates the state vector $\delta \mathbf{P}_{ar}$ with vector \mathbf{Res} , and \mathbf{v} is a measurement noise vector.

To obtain the estimate ($\hat{\delta \mathbf{P}}_{ar}$) of the state vector with a *Least Squares Fit* (LSF) criteria, the scalar cost function

$$J = (\mathbf{Res} - \mathbf{H} \hat{\delta \mathbf{P}}_{ar})^T \mathbf{W} (\mathbf{Res} - \mathbf{H} \hat{\delta \mathbf{P}}_{ar}) \quad (4-10)$$

must be minimized, where the weighting matrix \mathbf{W} is introduced to account for different (known a priori) quality in the measurements.

Setting

$$\frac{\partial J}{\partial \hat{\delta \mathbf{P}}_{ar}} = 0 \quad (4-11)$$

gives

$$\mathbf{H}^T \mathbf{W} \mathbf{H} \delta \hat{\mathbf{P}}_{\text{ar}} = \mathbf{H}^T \mathbf{W} \mathbf{Res} \quad (4-12)$$

and multiplying both sides by $(\mathbf{H}^T \mathbf{W} \mathbf{H})^{-1}$ yields

$$\delta \hat{\mathbf{P}}_{\text{ar}} = (\mathbf{H}^T \mathbf{W} \mathbf{H})^{-1} \mathbf{H}^T \mathbf{W} \mathbf{Res} \quad (4-13)$$

The objective of the covariance analysis is to determine how good this estimate is.

By inserting (4.9) into (4.13):

$$\delta \hat{\mathbf{P}}_{\text{ar}} = (\mathbf{H}^T \mathbf{W} \mathbf{H})^{-1} \mathbf{H}^T \mathbf{W} \mathbf{H} \delta \mathbf{P}_{\text{ar}} + (\mathbf{H}^T \mathbf{W} \mathbf{H})^{-1} \mathbf{H}^T \mathbf{W} \mathbf{v} = \delta \mathbf{P}_{\text{ar}} + (\mathbf{H}^T \mathbf{W} \mathbf{H})^{-1} \mathbf{H}^T \mathbf{W} \mathbf{v} \quad (4-14)$$

The *Parameter Residual Vector* (\mathbf{v}_{Par}) is defined as:

$$\mathbf{v}_{\text{Par}} = \delta \hat{\mathbf{P}}_{\text{ar}} - \delta \mathbf{P}_{\text{ar}} = (\mathbf{H}^T \mathbf{W} \mathbf{H})^{-1} \mathbf{H}^T \mathbf{W} \mathbf{v} \quad (4-15)$$

The value of $\delta \mathbf{P}_{\text{ar}}$ is not available, but if the statistical nature of the measurement noise \mathbf{v} is well known, a measure of the uncertainty in $\delta \hat{\mathbf{P}}_{\text{ar}}$ can be obtained by looking at the covariance of \mathbf{v}_{Par} :

$$\Sigma_{\mathbf{v}_{\text{Par}}} = E[\mathbf{v}_{\text{Par}} \mathbf{v}_{\text{Par}}^T] = E[\{(\mathbf{H}^T \mathbf{W} \mathbf{H})^{-1} \mathbf{H}^T \mathbf{W} \mathbf{v}\} \{(\mathbf{H}^T \mathbf{W} \mathbf{H})^{-1} \mathbf{H}^T \mathbf{W} \mathbf{v}\}^T] \quad (4-16)$$

where $E[\]$ expresses the *expected value*.

The covariance can then be written as:

$$\Sigma_{\mathbf{v}_{\text{Par}}} = (\mathbf{H}^T \mathbf{W} \mathbf{H})^{-1} \mathbf{H}^T \mathbf{W} E[\mathbf{v} \mathbf{v}^T] \{(\mathbf{H}^T \mathbf{W} \mathbf{H})^{-1} \mathbf{H}^T \mathbf{W}\}^T \quad (4-17)$$

In the case being studied, matrix \mathbf{Res} from (4-9) consists in a set of z_k^p residuals and two sets of z_k^ϕ residuals from two different, orthogonal baselines of equal length.

$$\mathbf{Z} = \begin{bmatrix} z_1^p & \cdots & z_n^p & z_{1a}^\phi & \cdots & z_{na}^\phi & z_{1b}^\phi & \cdots & z_{nb}^\phi \end{bmatrix}^T \quad (4-18)$$

From (4-9):

$$\mathbf{H}_k^\phi = \begin{bmatrix} \ell \frac{\mathbf{B}_a^\top \mathbf{F}_{ak}}{\Gamma_k} \mathbf{A}_{(p,k)} & \lambda & 0 \\ \ell \frac{\mathbf{B}_b^\top \mathbf{F}_{bk}}{\Gamma_k} \mathbf{A}_{(p,k)} & 0 & \lambda \end{bmatrix} \quad (4-19)$$

Where subscripts a and b identify the baseline

Using (4-3) and adding two zero vectors to account for the cycle ambiguity states in the carrier difference measurement:

$$\mathbf{H}_k^\rho = [\mathbf{e}_k^\top \mathbf{A}_{(p,k)} \quad 0 \quad 0] \quad (4-20)$$

The final observation matrix is then:

$$\mathbf{H}_{\text{data}} = \begin{bmatrix} \mathbf{H}_1^\rho \\ \vdots \\ \mathbf{H}_n^\rho \\ \mathbf{H}_1^\phi \\ \vdots \\ \mathbf{H}_n^\phi \end{bmatrix} \quad (4-21)$$

The measurement errors are distributed as

$$\mathbf{v}_k^\rho \sim \mathcal{N}(0, \sigma_\rho^2) \quad (4-22)$$

and

$$\mathbf{v}_k^\phi \sim \mathcal{N}(0, \sigma_\phi^2) \quad (4-23)$$

with $\sigma_\rho \approx 10$ m and $\sigma_\phi \approx 0.05$ m, corresponding to the performance of the MLA used in the LAAS prototypes.

The data measurement noise vector is then:

$$\mathbf{v}_{\text{data}} = [\mathbf{v}_1^\rho \quad \cdots \quad \mathbf{v}_n^\rho \quad \mathbf{v}_{1a}^\phi \quad \cdots \quad \mathbf{v}_{na}^\phi \quad \mathbf{v}_{1b}^\phi \quad \cdots \quad \mathbf{v}_{nb}^\phi]^\top \quad (4-24)$$

Replacing \mathbf{Res} , \mathbf{H} and \mathbf{v} with the elements from (4-18), (4-21) and (4-24) and introducing the state vector $\delta\mathbf{pint}$ (consisting of the ephemeris parameters minus Cic and Cic , plus one integer ambiguity for each baseline) as follows:

$$\delta\mathbf{pint} = \begin{bmatrix} \delta Mo \\ \delta a \\ \vdots \\ \delta Crs \\ \delta Crc \\ N_a \\ N_b \end{bmatrix} \quad (4-25)$$

the version of formula (4-9) corresponding to the data observed by the monitor is obtained:

$$\mathbf{Z} = \mathbf{H}_{data} \delta\mathbf{pint} + \mathbf{v}_{data} \quad (4-26)$$

The measurement noise v_k^ϕ is composed mainly of receiver noise and multipath.

Because receiver noise is white and multipath errors typically have time constants of about one minute, samples taken two minutes or more apart, are typically uncorrelated. In contrast the ionospheric delay dominates v_k^ρ , which makes it possible for noise from measurements hours apart to be highly correlated. For example, using a sample interval of four minutes, z_k^ϕ measurements can be considered totally uncorrelated as the noise is effectively “whitened” by the sampling interval, while z_k^ρ 's time correlation must be taken into account in the orbit estimation process.

The noise distribution is modeled as:

$$v_{data} \sim N(0, \mathbf{V}) \quad (4-27)$$

where

$$\mathbf{V} = \begin{bmatrix} \mathbf{V}^\rho & | & \mathbf{0} \\ \hline \mathbf{0} & | & \mathbf{I}_{(2n)} \sigma_\phi^2 \end{bmatrix} \quad (4-28)$$

To account for the correlation of the pseudorange measurement noise, assuming its evolution with respect to time can be described with a First Order Gauss Markov process, each element of \mathbf{V}^p is defined by:

$$V_{ij}^p = \sigma_p^2 \exp(-|i - j| \Delta t / \tau) \quad (4.29)$$

where Δt is the four minute sample interval, and τ is the correlation of the ionospheric delay.

By replacing \mathbf{H} with \mathbf{H}_{data} , and $E[\mathbf{v}\mathbf{v}^T]$ with \mathbf{V} ; from (4-15), the covariance of

$$\mathbf{v}_{\delta\text{pint}} = \delta\hat{\mathbf{p}}\text{int} - \delta\mathbf{p}\text{int} \quad (4.30)$$

is:

$$\Sigma_{\mathbf{v}_{\delta\text{pint}}} = E[\mathbf{v}_{\delta\text{pint}} \mathbf{v}_{\delta\text{pint}}^T] = (\mathbf{H}_{\text{data}}^T \mathbf{W} \mathbf{H}_{\text{data}})^{-1} \mathbf{H}_{\text{data}}^T \mathbf{W} \mathbf{V} \{ (\mathbf{H}_{\text{data}}^T \mathbf{W} \mathbf{H}_{\text{data}})^{-1} \mathbf{H}_{\text{data}}^T \mathbf{W} \}^T \quad (4.31)$$

To obtain the *best linear unbiased estimate* [Gel74] minimizing the trace of $\Sigma_{\mathbf{v}_{\delta\text{pint}}}$, the weighting matrix is defined as

$$\mathbf{W} = \mathbf{V}^{-1} \quad (4.32)$$

Introducing (4-32) into (4-31):

$$\Sigma_{\mathbf{v}_{\delta\text{pint}}} = (\mathbf{H}_{\text{data}}^T \mathbf{V}^{-1} \mathbf{H}_{\text{data}})^{-1} \quad (4.33)$$

To obtain a meaningful measurement of the estimate accuracy in the position domain the upper left 14x14 sub-matrix of $\mathbf{v}_{\delta\text{pint}}$ (i.e. excluding the cycle ambiguity terms) is defined as the *Ephemeris Parameters Residual* $\mathbf{v}_{\delta\text{p}}$. Pre and post multiplying it at each time by the corresponding sensitivity matrix from (2-8) the covariance for the satellite position error is:

$$\Sigma_{\delta\mathbf{r}} = \mathbf{A}_{(p,k)} \Sigma_{\mathbf{v}_{\delta\text{p}}} \mathbf{A}_{(p,k)}^T \quad (4.34)$$

For an initial evaluation of the impact of the measurement-based monitoring on the overall performance of the monitor, the MDE is defined as in (3-16), maintaining the non-centrality parameter λ derived for the specifications for a rising satellite, and replacing the position error covariance with (4-34).

4.4 Sensitivity Analysis

The parameters of the error model described in the previous section will vary from site to site, and some, like the pseudorange time constant, do not have a universally accepted value in the related literature. Therefore, it is necessary to study the sensitivity of the MDE to these parameters. In this sensitivity analysis, only one parameter at a time was varied, keeping the other ones constant at the following values:

$$\sigma_p = 10 \text{ m}$$

$$\sigma_\phi = 0.05 \text{ m}$$

$$\tau = 12 \text{ hours}$$

$$\ell = 100 \text{ m}$$

$$\text{LGF latitude: } 41.98^\circ$$

$$\text{LGF longitude: } -87.90^\circ$$

The LGF location corresponds to the Chicago O'Hare airport. All plots in this and subsequent sections were generated using ephemerides from the almanac corresponding to the same day for all satellites. In all figures the rise time is set to zero for each SV.

The sensitivity to the time constant τ is particularly important because it is difficult to obtain a precise number for it. In figure 4.2 it can be observed that the sensitivity to this

parameter is not significant for values varying from three hours to a whole day. This gives ample margin for the adopted value of 12 hours.

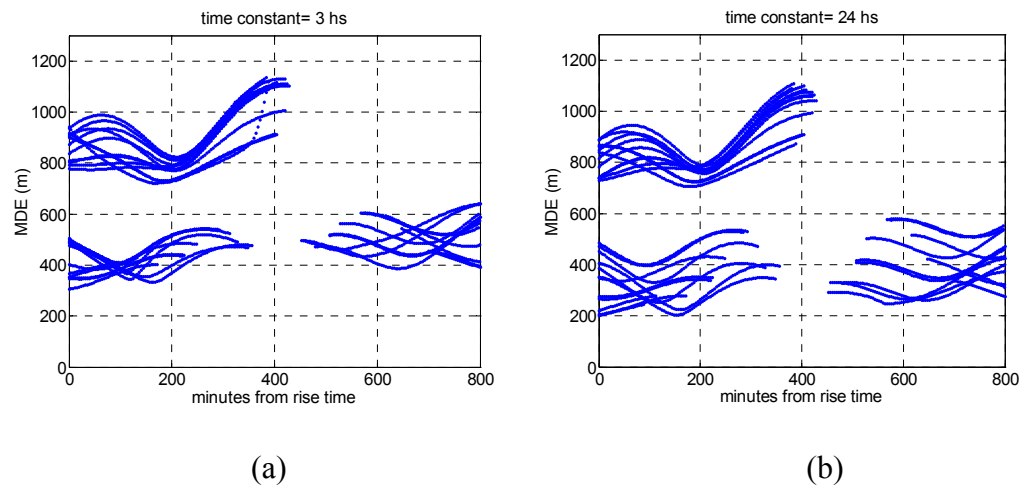


Figure 4.2 MDE Values for Different Time Constants τ : (a) $\tau= 3$ hours, (b) $\tau= 24$ hours

The second element considered is the LGF location. For each site, satellite passes describe different paths, varying in length and geometry. Values of the MDE vary accordingly with the specific combination of latitude and longitude. In general, it can be said that the longer the pass the smaller the MDE. The value is also related to the geometry; usually satellites with two different passes on the same day have measurements corresponding to totally different parts of their orbit, and thus yield lower values of MDE. The exception is when the second part of the path is very short; in this case the smaller segment was eliminated, since the cost of having to estimate two extra parameters (one

more cycle ambiguity for each baseline) is higher than the benefit in measurement geometric diversity. A guideline of worst MDE values for sample LGF latitudes can be seen in Table 4-1. The best results are between 60° and 70° , and the worst locations are in the 30° to 40° region.

Table 4.1 Approximate Maximum MDE Value at Different LGF Latitudes.

Latitude (deg)	0	15	30	45	60	75	90
Max MDE (m)	590	570	650	600	340	350	420

Figures 4.3 and 4.4 show examples of sensitivity to latitude and longitude respectively. A more extensive set of examples for different latitudes can be found in Appendix I.

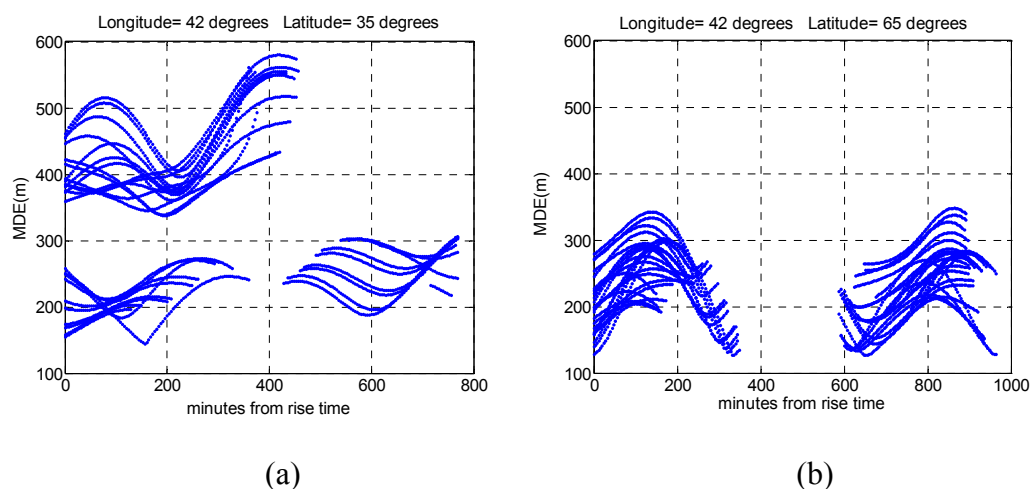


Figure 4.3 Variation of MDE with Latitude: (a) Latitude = 35° , (b) Latitude = 65°

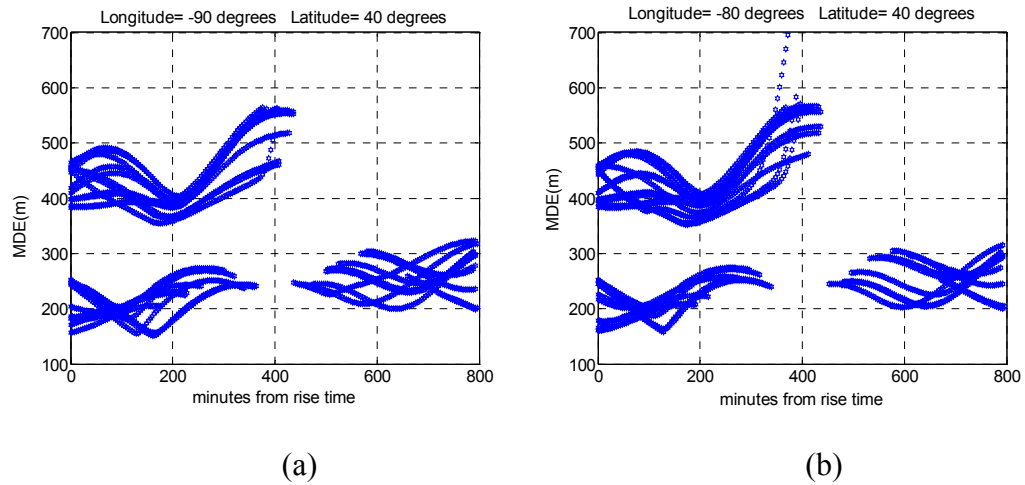


Figure 4.4 Variation of MDE with Longitude: (a) Latitude = -90° , (b) Latitude = -80°

The precision of the estimation is directly proportional to accuracy of the main measurement $\Delta^2\phi_k$. This fact can be observed in Figure 4.5 that shows that MDE values are highly sensitive to variations in the double difference carrier measurement standard deviation σ_ϕ . The results are not as sensitive to the pseudorange accuracy but this measurement serves as an absolute reference (the carrier measurement is only composed of differences), and it is needed in the estimation process.

In figure 4.6 the sensitivity to variations in σ_p is shown. Results show that proportionally bigger variations have a smaller impact in the MDE values. The impact of completely eliminating the pseudorange measurement is also shown.

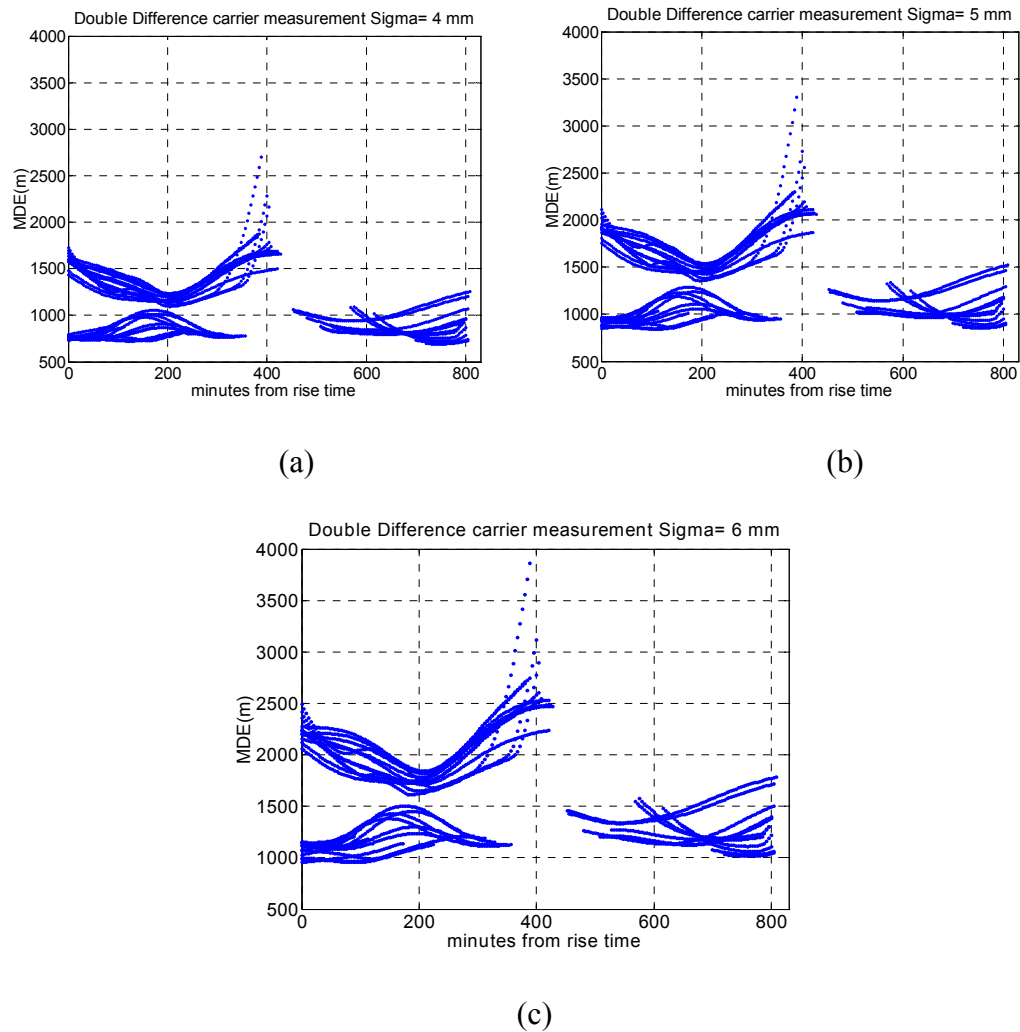
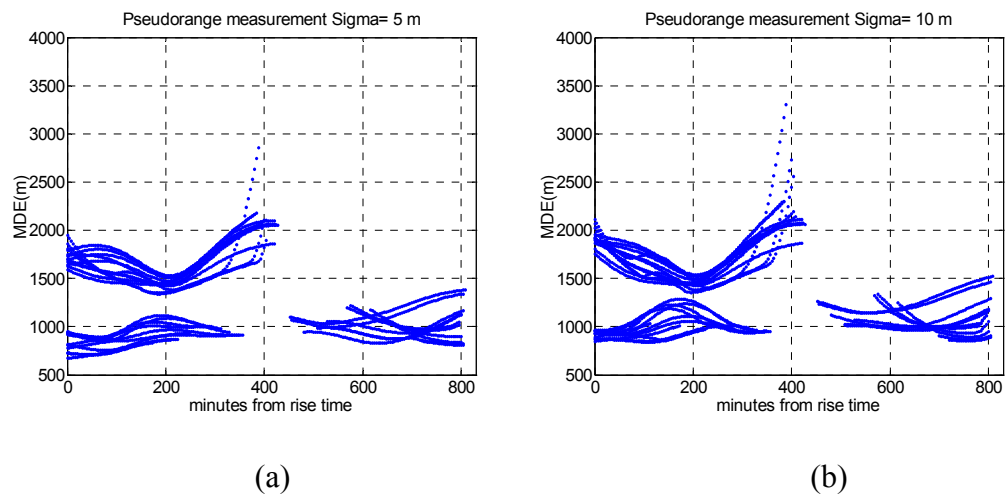


Figure 4.5 MDE Sensitivity to σ_ϕ : (a) $\sigma_\phi = 4$ mm, (b) $\sigma_\phi = 5$ mm, (c) $\sigma_\phi = 6$ mm



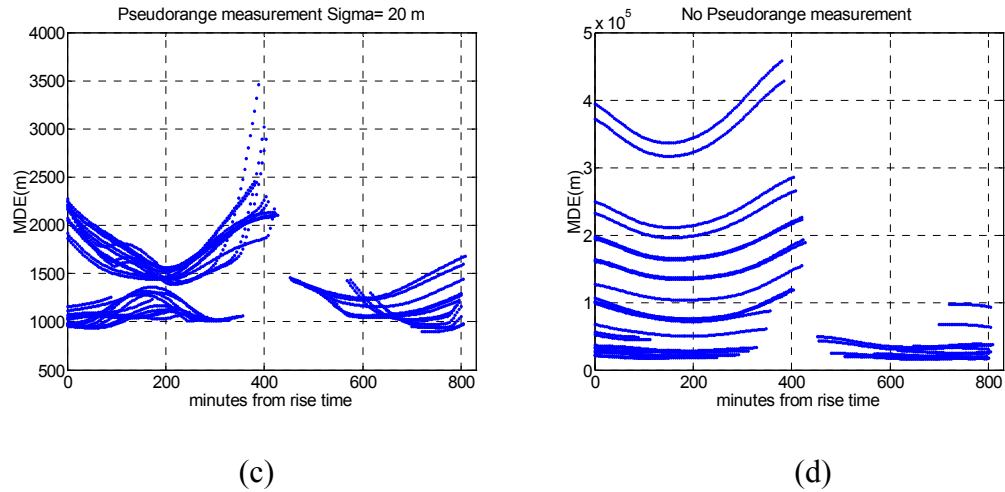


Figure 4.6 MDE Sensitivity to σ_ρ : (a) $\sigma_\rho = 5$ m, (b) $\sigma_\rho = 10$ m, (c) $\sigma_\rho = 20$ m,
 (d) $\sigma_\rho = \infty$

4.5 Cycle Ambiguity Resolution

Depending on the number of segments of a satellite's pass as seen from the LGF, the monitor needs to estimate two or four extra nuisance parameters: the cycle ambiguities (N 's) of the $\Delta^2\phi$ measurement for each baseline. This worsens the monitor's estimation capabilities for the ephemeris parameters. If the error in the different N 's is small enough, the fact that these numbers necessarily must be integers (they represent full carrier frequency cycles) will allow rounding. Given that the measurement based monitor is not executed in real time, but rather by batch processing at the end of the pass, this allows the estimation to be done in two phases. First the vector $\delta\mathbf{p}_{int}$ is computed using (4-13). Then the values for the N 's are rounded, and inserted into (4-8). Finally a second estimation, now including only the ephemeris parameter error vector ($\delta\mathbf{p}$) is performed by using again (4-13):

$$\delta \hat{\mathbf{p}} = (\mathbf{H}_{\text{data}}^T \mathbf{V}^{-1} \mathbf{H}_{\text{data}})^{-1} \mathbf{H}_{\text{data}}^T \mathbf{V}^{-1} \mathbf{Z} \quad (4-35)$$

To verify if the rounding process is safe, the standard deviations of parameters N derived in the covariance analysis must be studied.

For a failure in the rounding process to occur, the absolute value of the error in the cycle ambiguity estimation has to be equal or bigger than 0.5 cycles, (equivalent to 9.5 cm). This type of error is not an integrity concern, as the 19 cm wavelength bias introduced in all $\Delta^2 \phi$ measurements would make the monitor test to trigger the alarm, but these are fault free alarms that could affect availability.

Figure 4.7 shows the σ 's from the covariance analysis corresponding to cycle ambiguity numbers, for all satellites, for the two baselines, and including the two passes in the cases were they occurred. Basing the analysis on the worst case in the figure, and conservatively rounding the error standard deviation to a value of 10^{-2} cycles, the error magnitude of 0.5 (necessary to cause an error in the cycle ambiguity rounding), corresponds to 50 times the standard deviation. There will be no impact on availability from errors in the cycle ambiguity estimation.

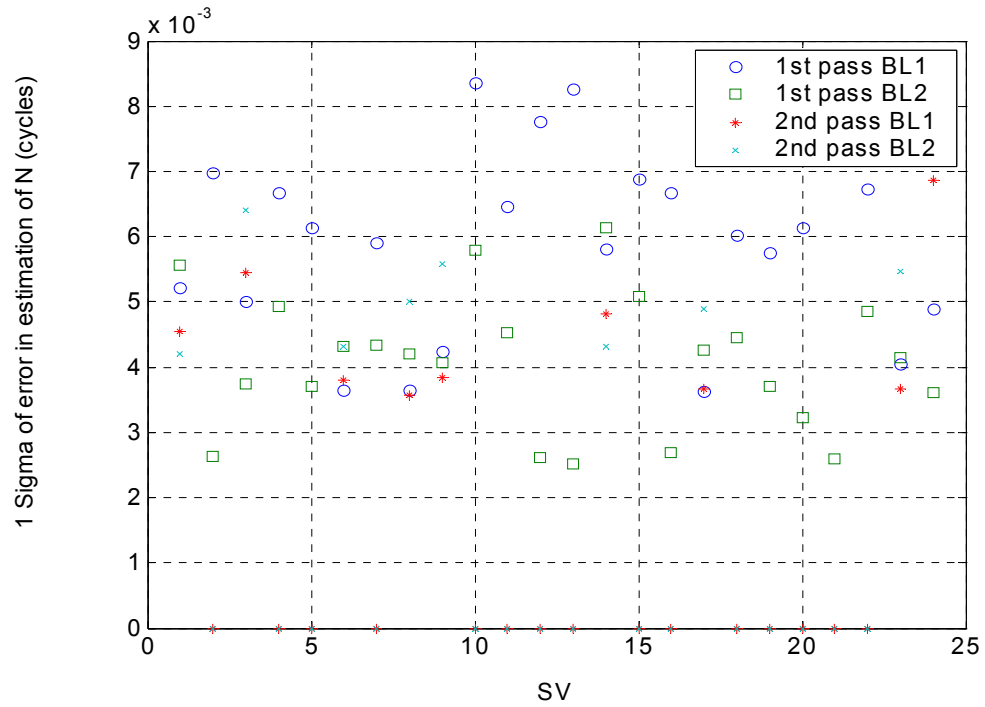


Figure 4.7 Standard Deviation on Cycle Ambiguity Estimation for All Satellites

4.6 MDE Values

The final sensitivity results of this chapter are presented with respect to baseline length because this is a major aspect of the LGF structure that has not yet been defined. Determining the necessary distance between the antennas that form the baselines is very important, as the airports have physical constraints regarding their siting.

Figure 4.8 shows that for a baseline length of 400 meters the maximum value computed is smaller than 950 meters. For baselines of 800 meters (not shown in plot), maximum MDE values are below 470 meters.

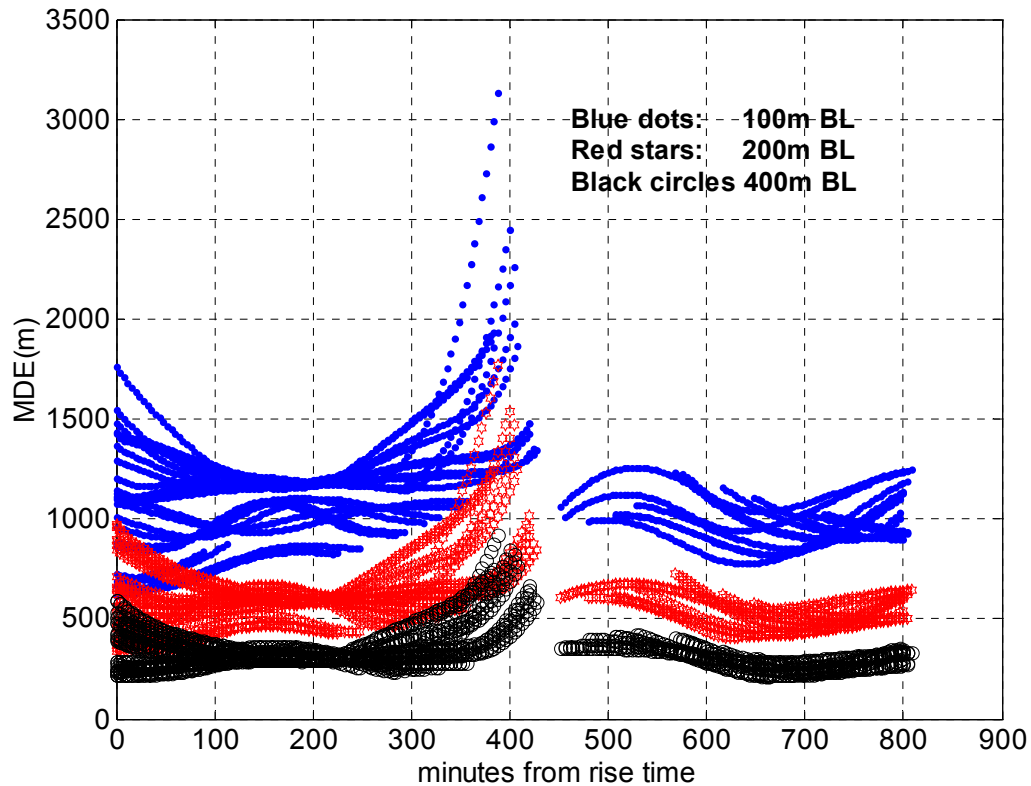


Figure 4.8 MDE Values for Different Baseline Lengths

These results still need to be verified experimentally, but the values obtained through the covariance analysis in this chapter suggest this is a suitable means to validate after maneuver broadcast. For baseline lengths as short as 200 m values of MDE are significantly smaller than the ones derived in Chapter III with FOH ephemeris parameter estimation.

Regarding the use of measurement based monitoring on a regular basis to account for errors in previously validated ephemerides, a first qualitative measure of the impact on the total MDE of implementing this procedure can be seen in Table 4.2. The total MDE was computed with (4-36) by combining the MDE_{meas} from the measurement based

monitor (taking maximum values from Figure 4.8) with the MDE_{FOH} derived for the FOH in Chapter III as:

$$MDE = \sqrt{MDE_{meas}^2 + MDE_{FOH}^2} \quad (4-36)$$

Results show that for baseline lengths as short as 200 m the value is still below the desirable limit of 3500m.

Table 4.2 Total MDE Values for Different Baseline Lengths

Baseline Length	MDE_{meas}	MDE_{FOH}	Total MDE
100 m	3200 m	1744 m	3645 m
200 m	1800 m	1744 m	2563 m

CHAPTER V

CONCLUSIONS

The Global Positioning System operated by the DoD has numerous widespread applications within the civilian part of society. Its accuracy and reliability are significantly improved by the use of DGPS. The FAA is transitioning the National Airspace System from ground based to satellite based navigational aids, by implementing its version of DGPS, the Local Area Augmentation System (LAAS), that will allow precision approach and landing to be safer and less expensive.

LAAS has strict specifications regarding accuracy, integrity, availability and continuity that have to be met. For one of the failure sources in user positioning, the *satellite ephemeris*, the integrity requirement is not satisfied by the current single frequency (Cat I structure) proposed monitors (like the *Built-in LAAS Ephemeris Monitoring* or the *DPR / DPDAS Method*). It is desirable to implement a monitor that meets this requirement, without affecting the current navigation availability and continuity levels of LAAS, or its hardware structure.

There are two ephemeris anomaly threat models: *Type A*, where the error is caused by a satellite maneuver, and *Type B* when the broadcast ephemeris data is erroneous, with no satellite maneuver involved. Type B errors can be detected by comparing the *ephemeris to be validated* with an estimate based on previously verified ephemerides. For Type A failure monitoring the estimate can only be based on measurements.

The responsibility to detect anomalous ephemeris errors lies exclusively on the LAAS Ground Facility (LGF). The user must be notified of the ability of the LGF to rule out such a failure. For that purpose, along with the ranging correction, the P-value is

transmitted to the aircraft, that uses it to compute its *Vertical Protection Level for an Ephemeris failure hypothesis*. The P-value is directly proportional to the Minimum Detectable Error. MDE values below 3500 m will not affect the current navigation availability or continuity levels.

In Chapter III an algorithm to monitor ephemerides (type B threats) is provided, showing that if using the ZOH estimation method for a rising satellite, the MDE is 4984 m. Using the FOH estimation method the MDE is 1744 m. As the FOH will always be possible if there is no maneuver in the previous two days, results suggest the desired integrity is achieved without affecting current continuity or availability levels.

Type A failure analysis in Chapter IV shows that a measurement based monitor using the current LAAS configuration can achieve MDE values smaller than 3500 m with baselines as short as 100 m, and obtaining maximum values smaller than 1000 m for a baseline length of 400 m. The experimental verification of results from Chapter IV is currently being executed.

APPENDIX A
BROADCAST PARAMETER VALUES DISTRIBUTIONS

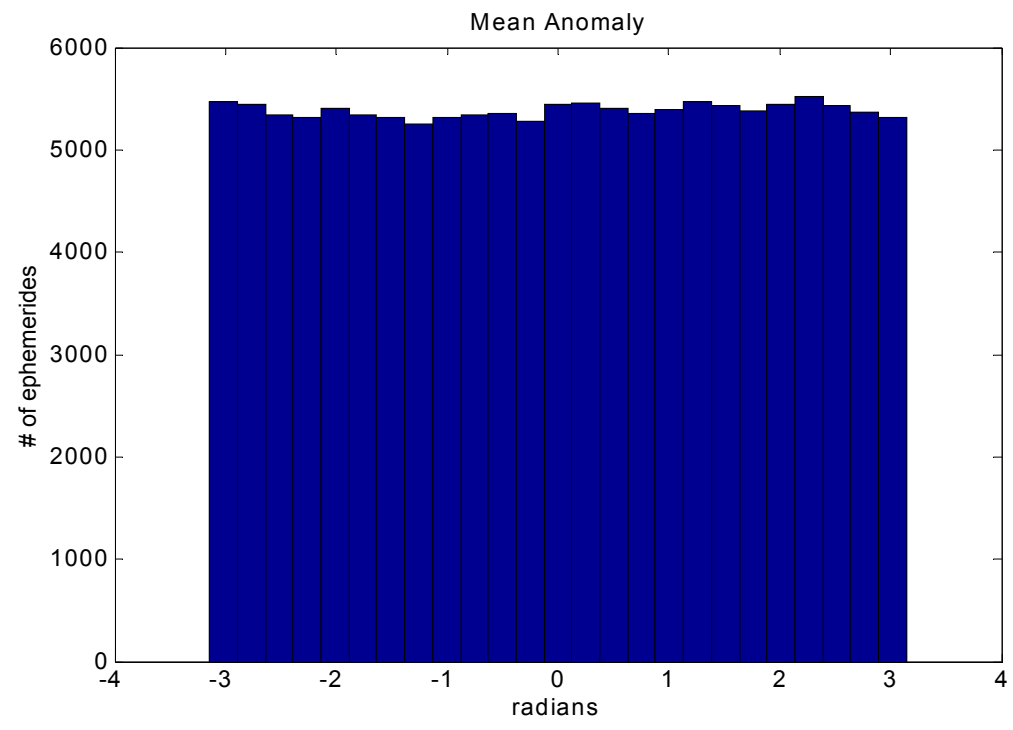


Figure A.1 Distribution of Values for the Mean Anomaly

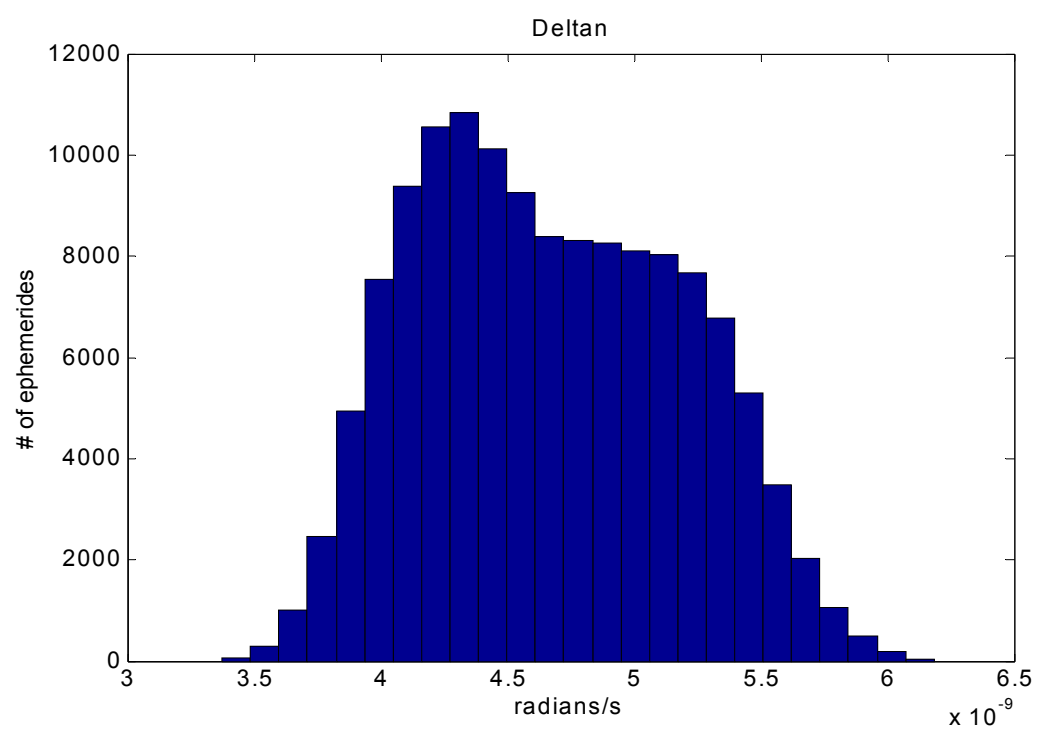


Figure A.2 Distribution of Values for Mean Motion Difference From Computed Value

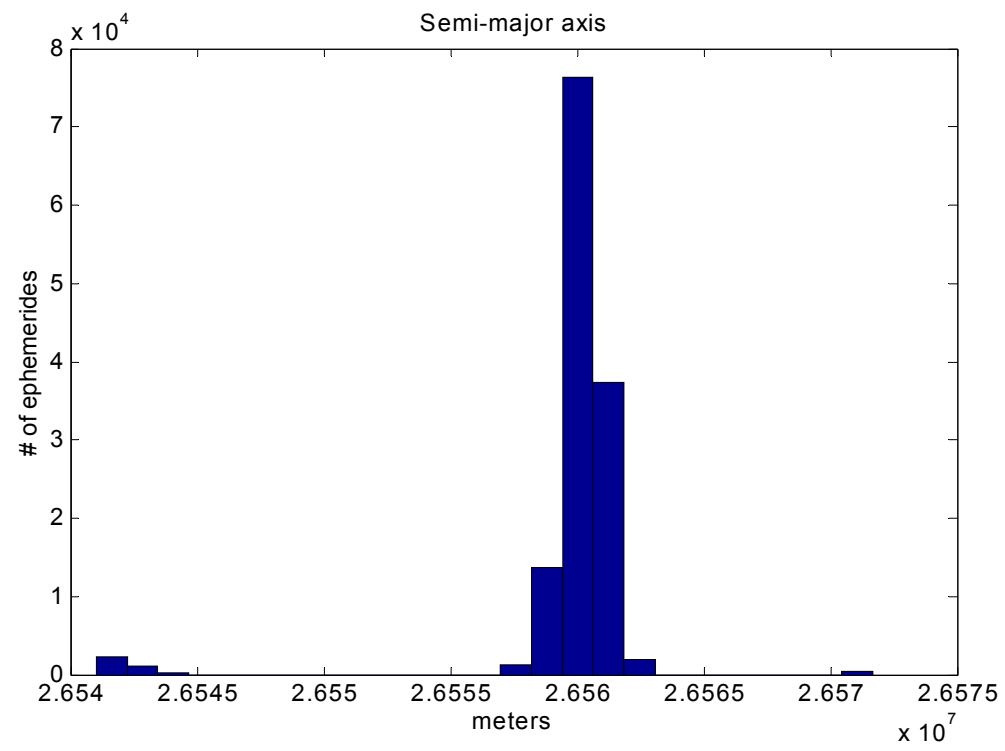


Figure A.3 Distribution of Values for Semi-Major Axis

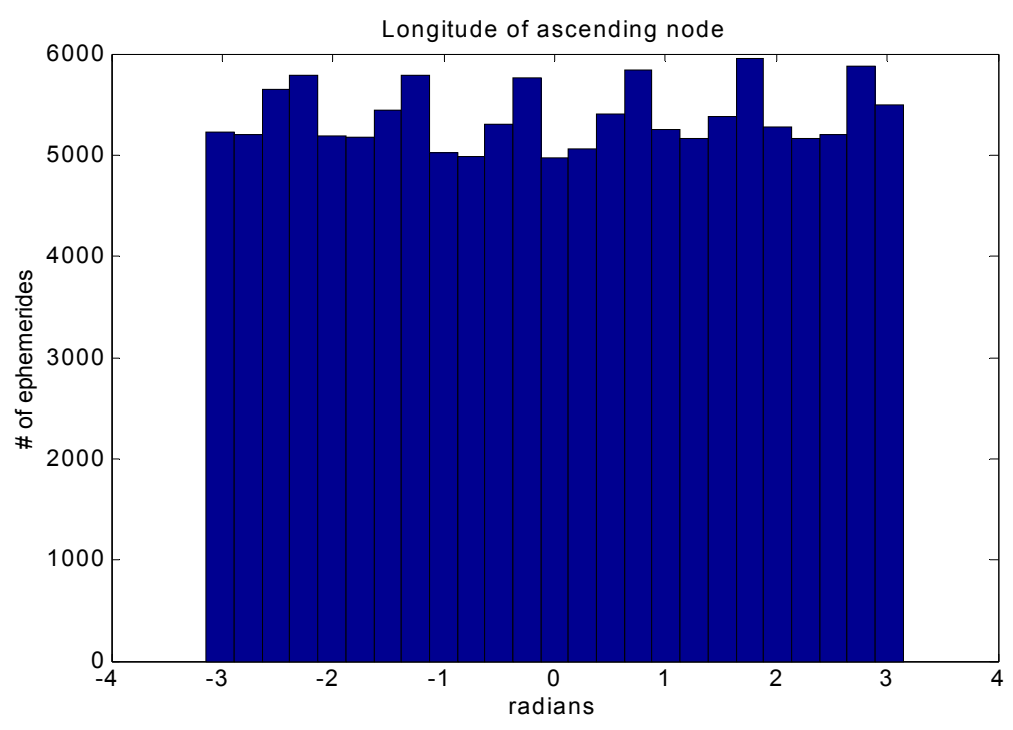


Figure A.4 Distribution of Values for Longitude Of Ascending Node of Orbit Plane at toe

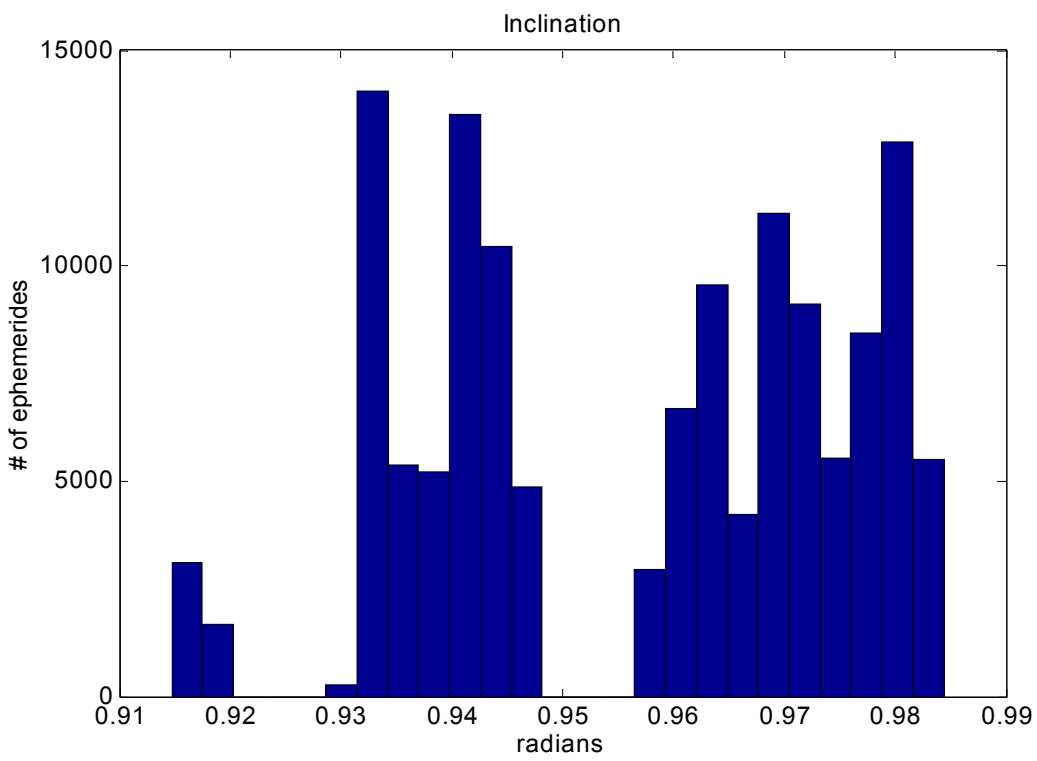


Figure A.5 Distribution of Values for Inclination Angle at toe

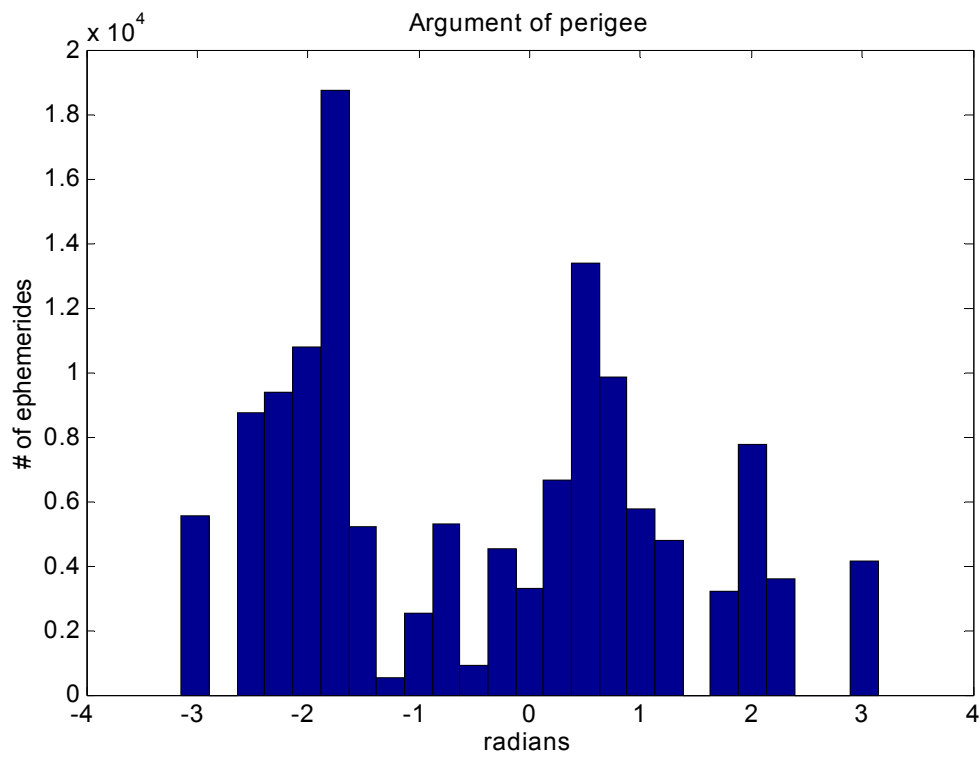


Figure A.6 Distribution of Values for Argument of Perigee

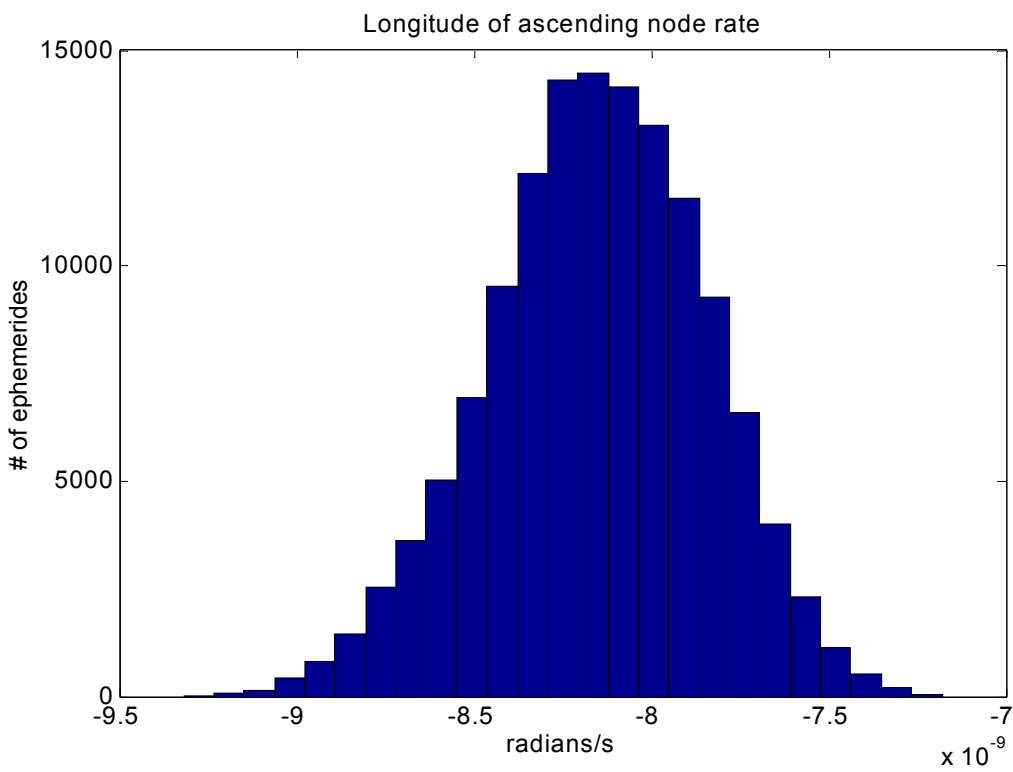


Figure A.7 Distribution of Values for Rate of Right Ascension

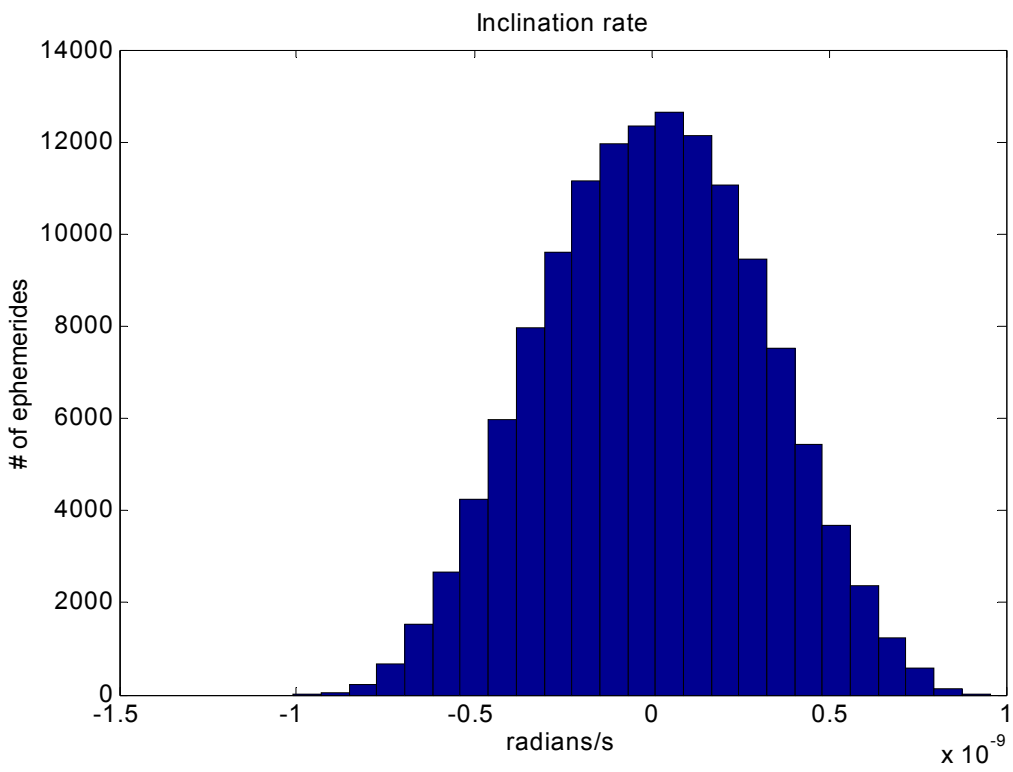


Figure A.8 Distribution of Values for Rate of Inclination Angle

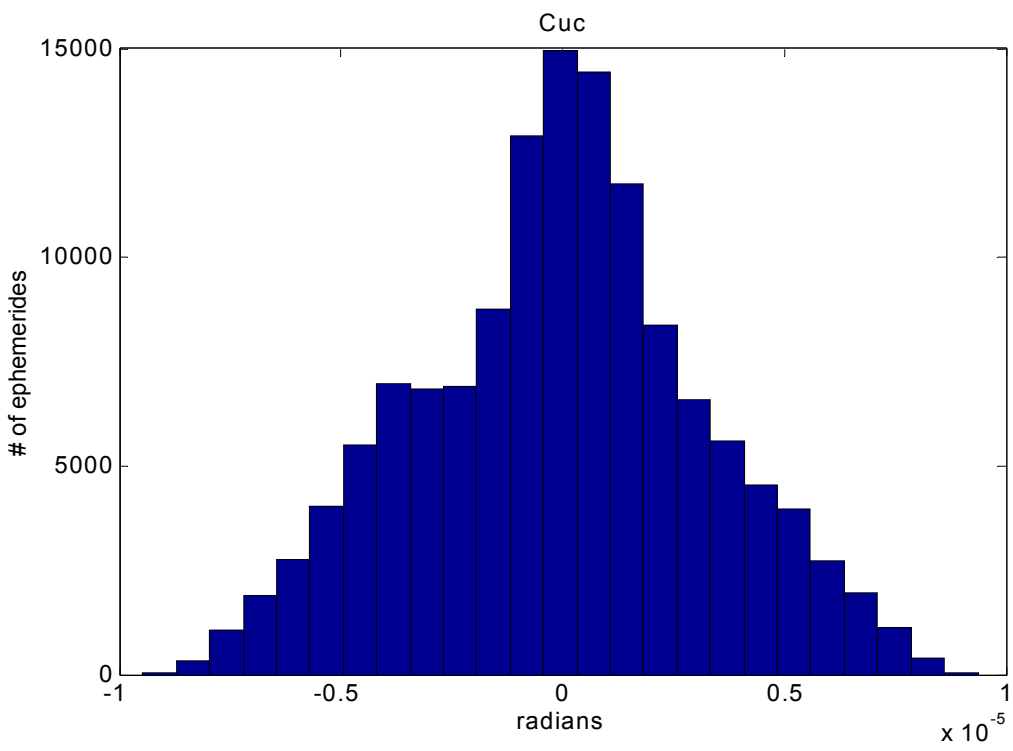


Figure A.9 Distribution of Values for the Amplitude of the Cosine Harmonic Correction Term to the Argument of Latitude

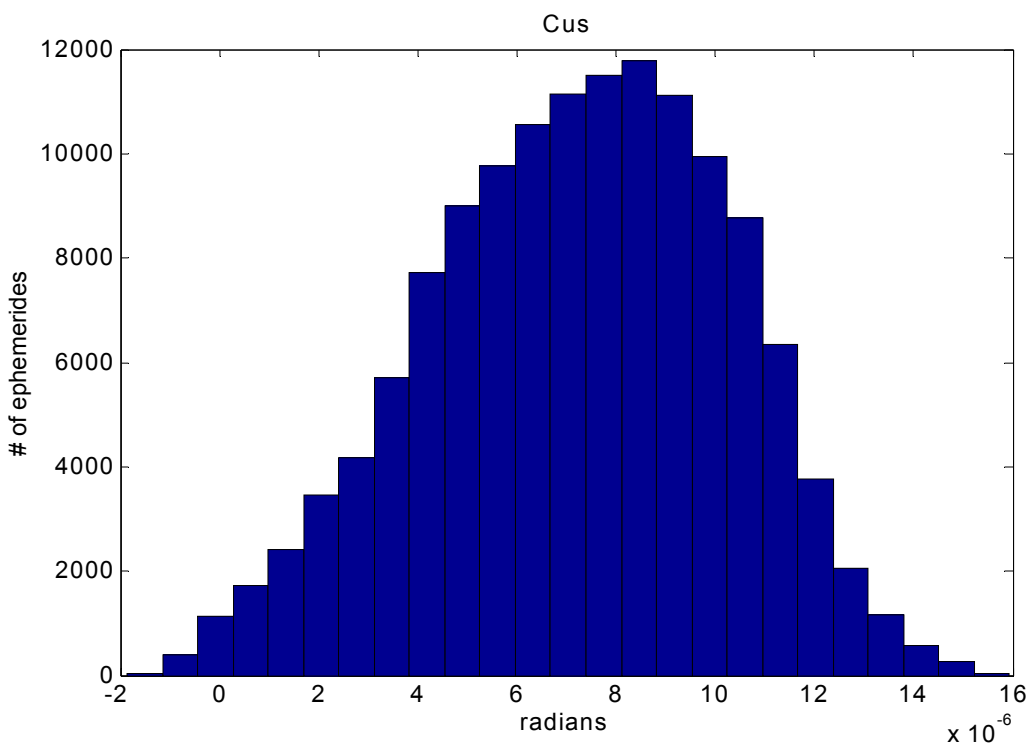


Figure A.10 Distribution of Values for the Amplitude of the Sine Harmonic Correction Term to the Argument of Latitude

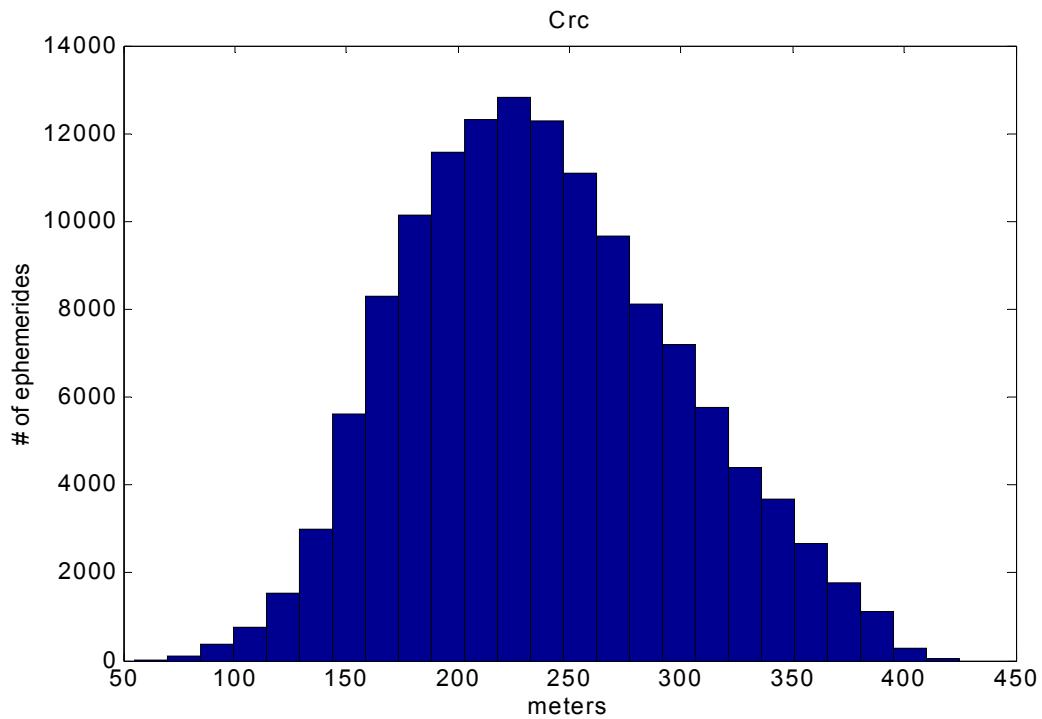


Figure A.11 Distribution of Values for the Amplitude of the Cosine Harmonic Correction Term to the Orbit Radius

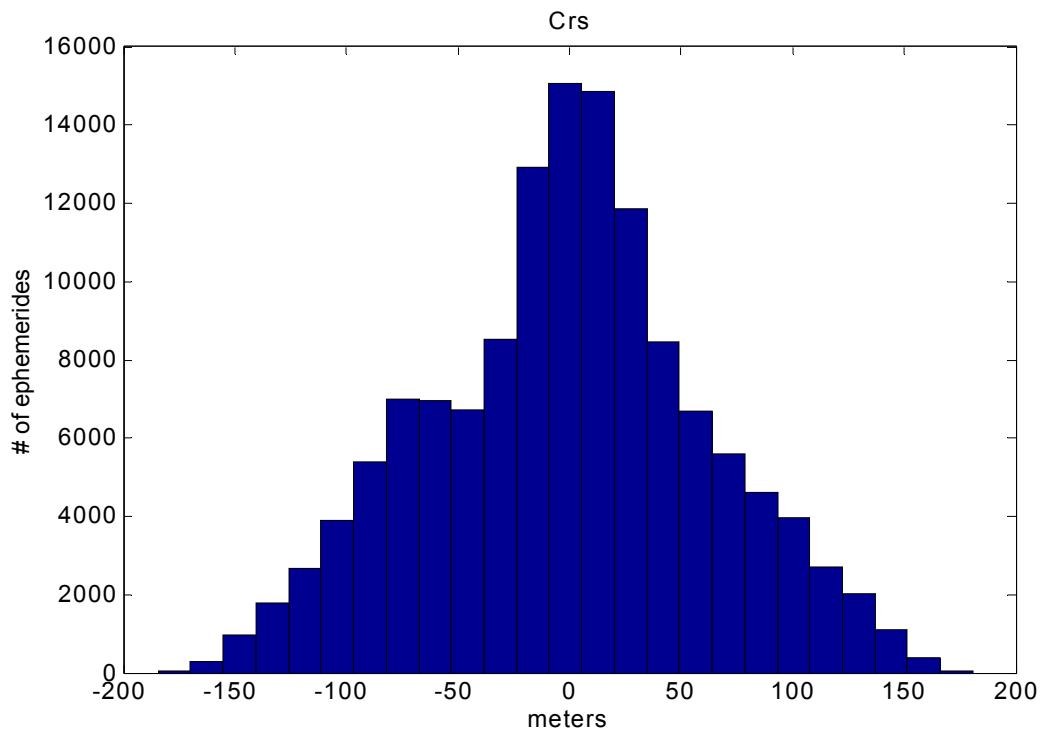


Figure A.12 Distribution of Values for the Amplitude of the Sine Harmonic Correction Term to the Orbit Radius

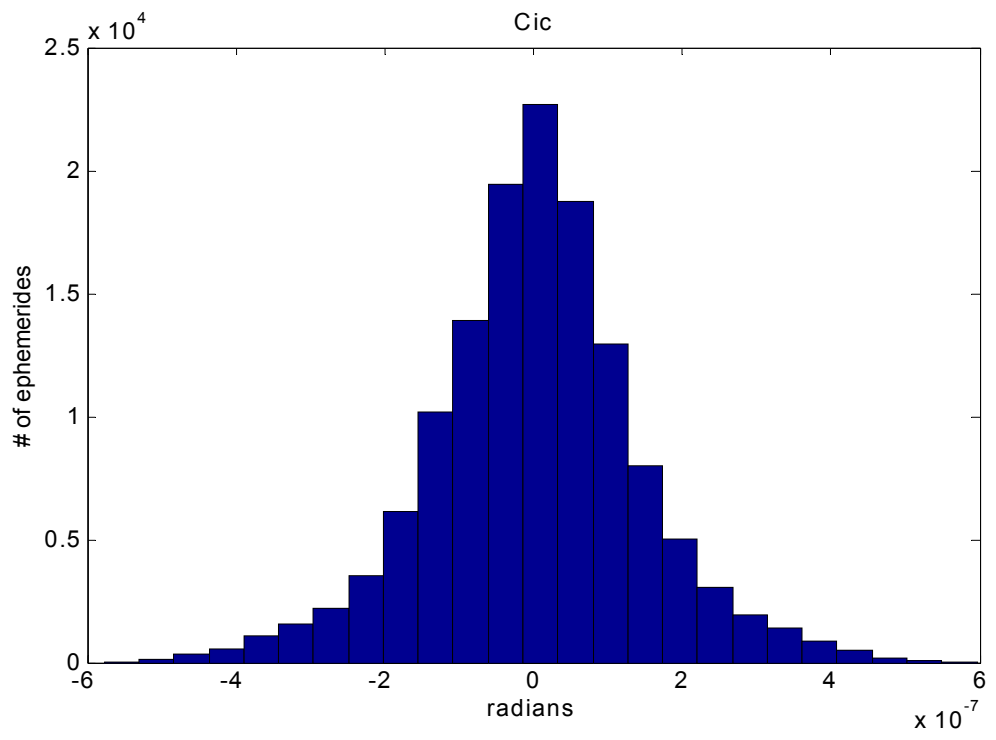


Figure A.13 Distribution of Values for the Amplitude of the Cosine Harmonic Correction Term to the Angle of Inclination

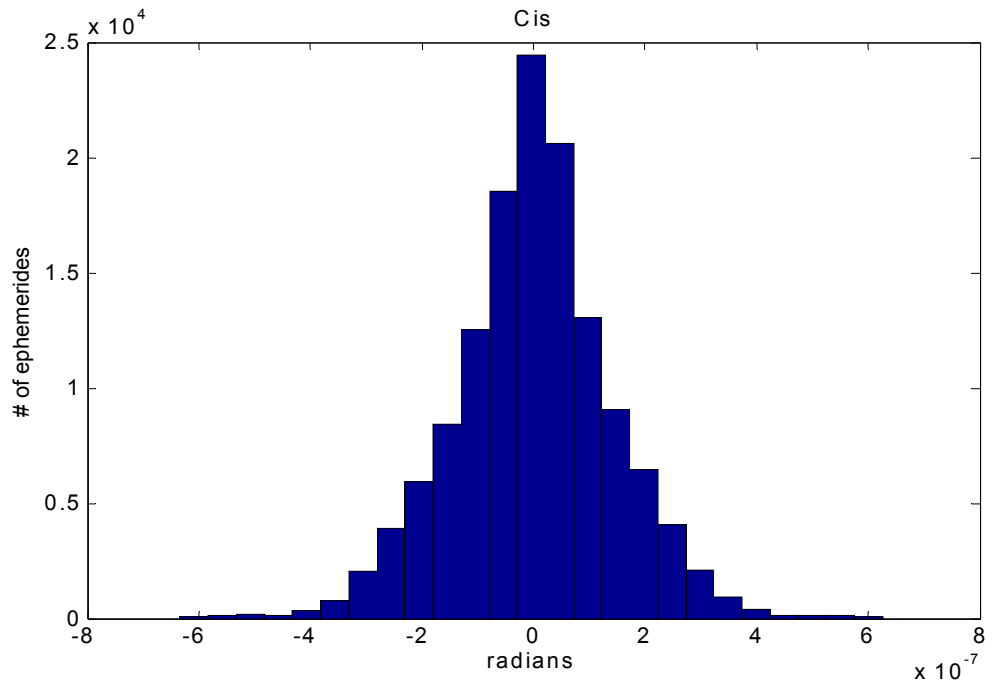


Figure A.14 Distribution of Values for the Amplitude of the Sine Harmonic Correction Term to the Angle of Inclination

APPENDIX B
BROADCAST PARAMETER DIFFERENCES FROM DAY TO DAY
DISTRIBUTIONS.

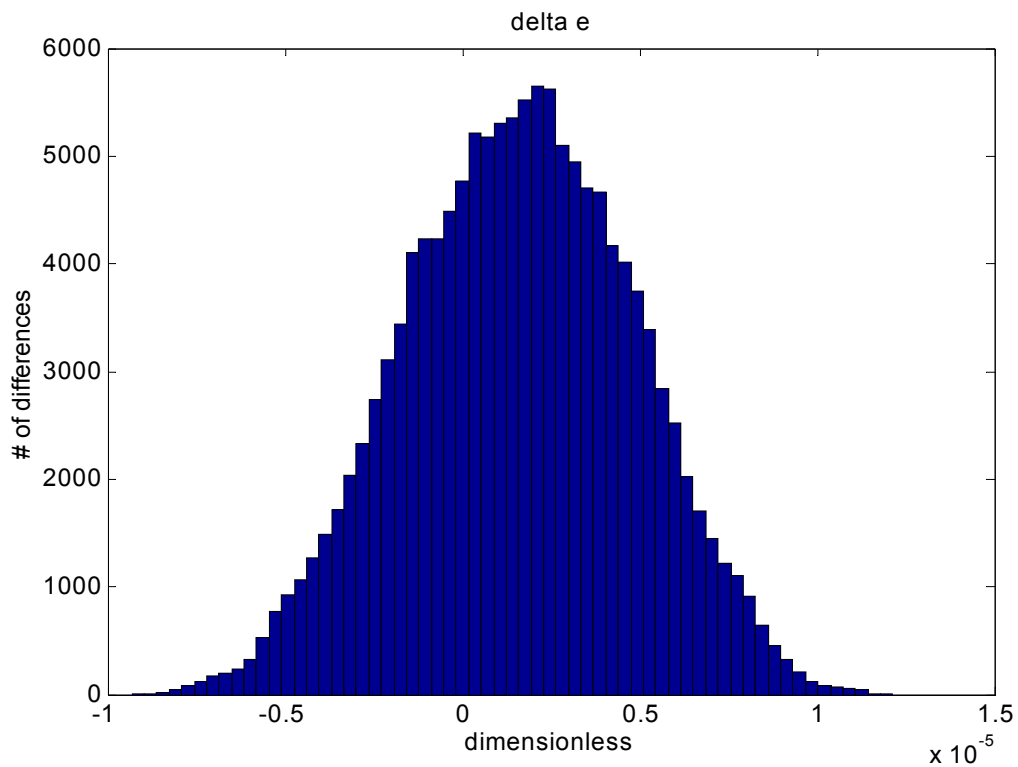


Figure B.1 Distribution of Differences in Eccentricity From Day to Day

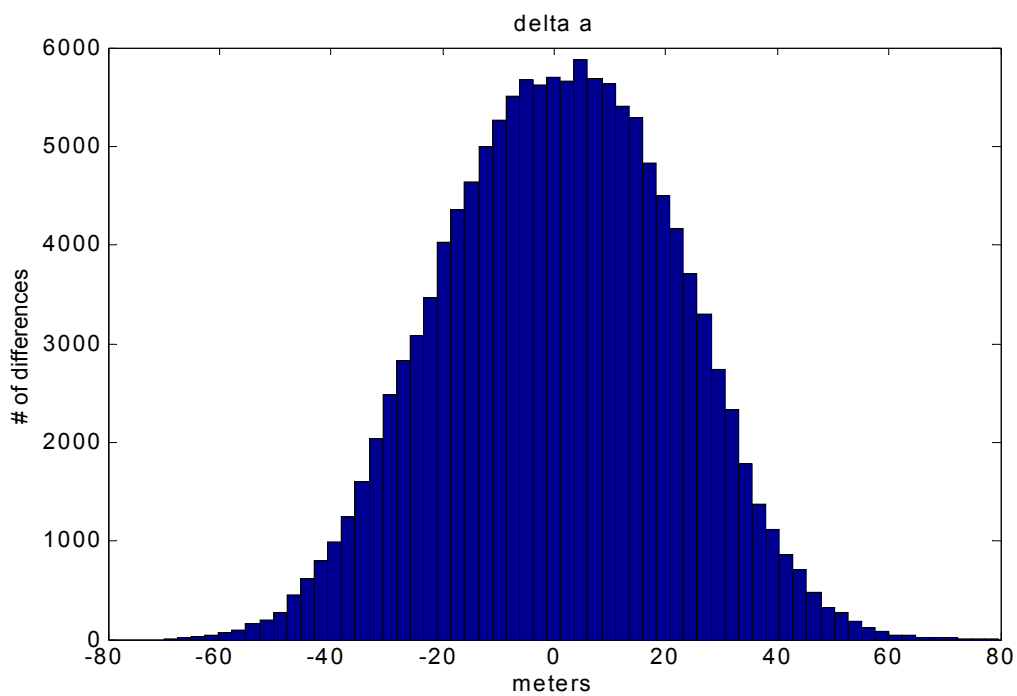


Figure B.2 Distribution of Differences in Semi-Major Axis From Day to Day

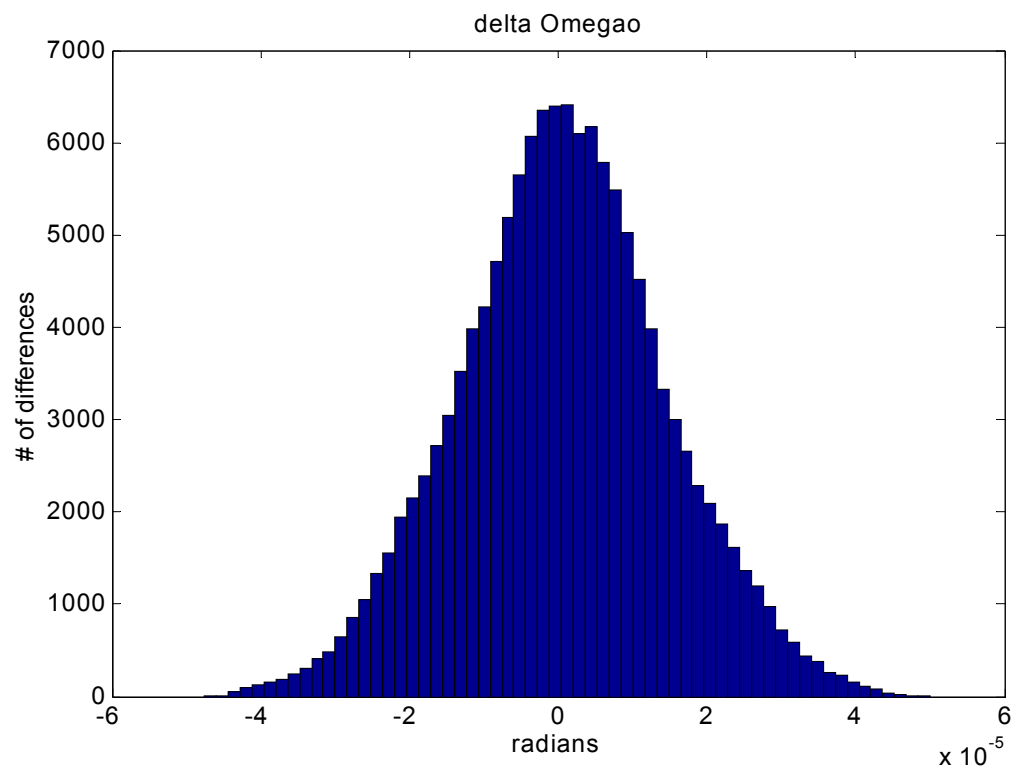


Figure B.3 Distribution of Differences in Longitude of Ascending Node From day to Day

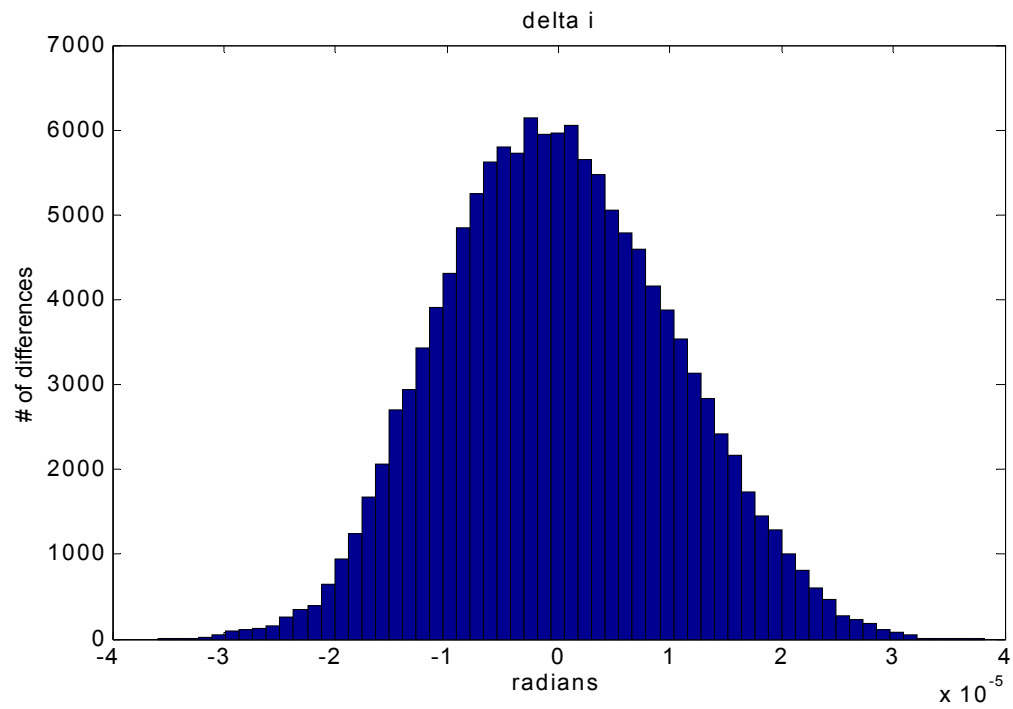


Figure B.4 Distribution of Differences in Inclination Angle From Day to Day

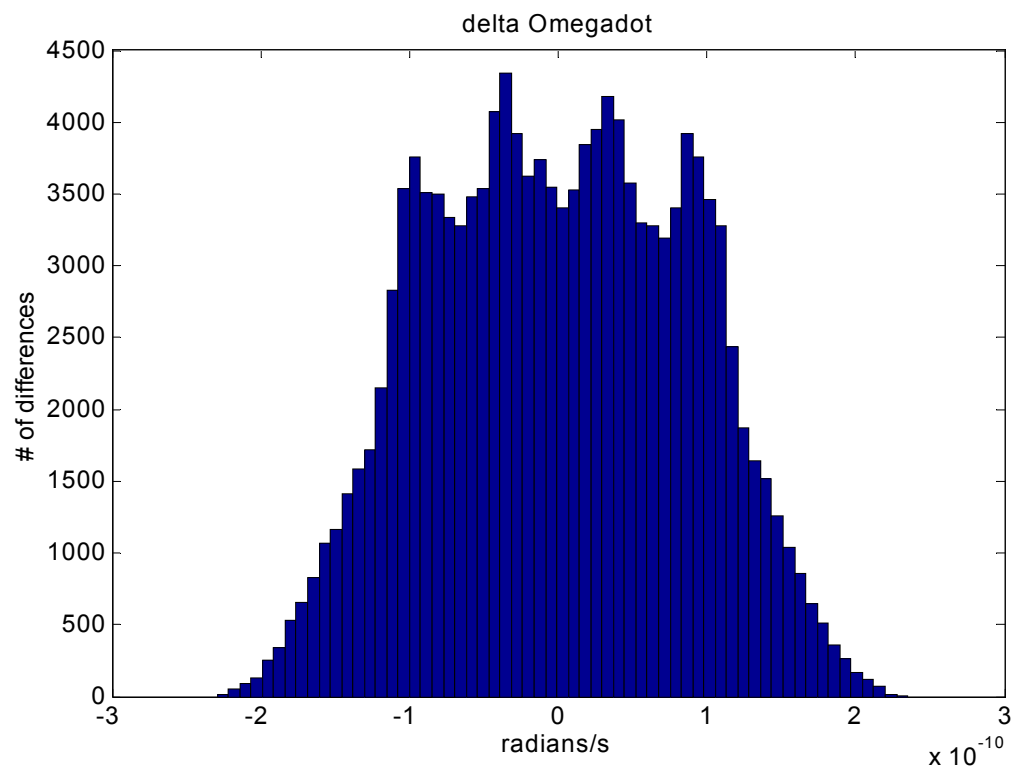


Figure B.5 Distribution of Differences in Rate of Right Ascension From Day to Day

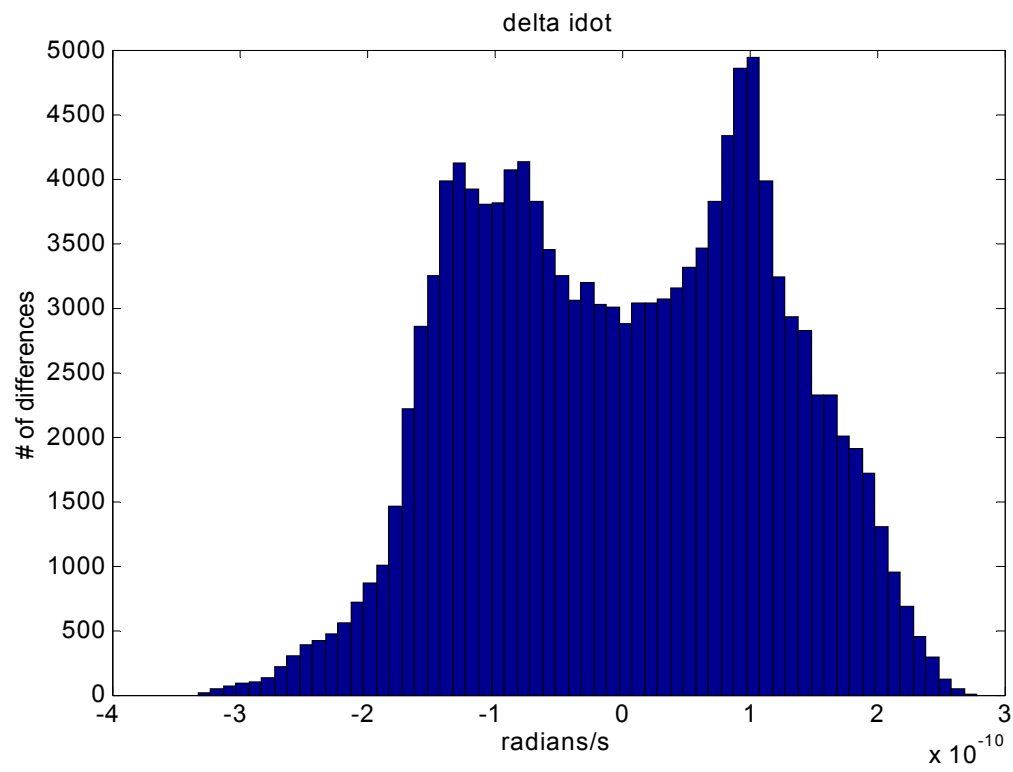


Figure B.6 Distribution of Differences in Rate of Inclination Angle From Day to Day

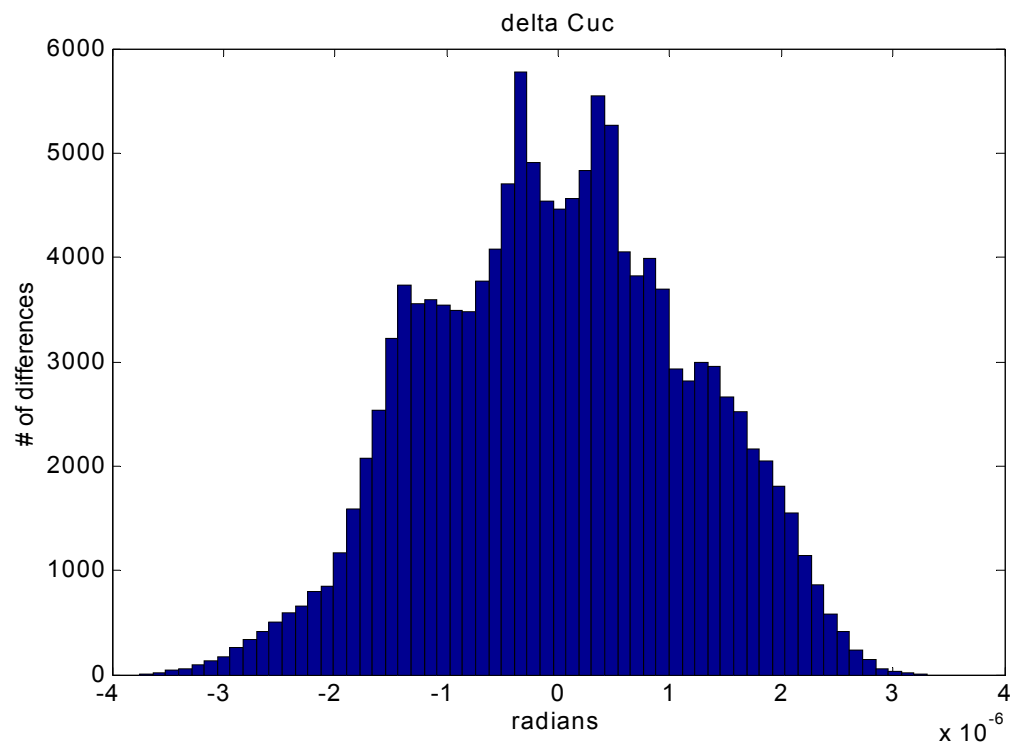


Figure B.7 Distribution of Differences in Cuc From Day to Day

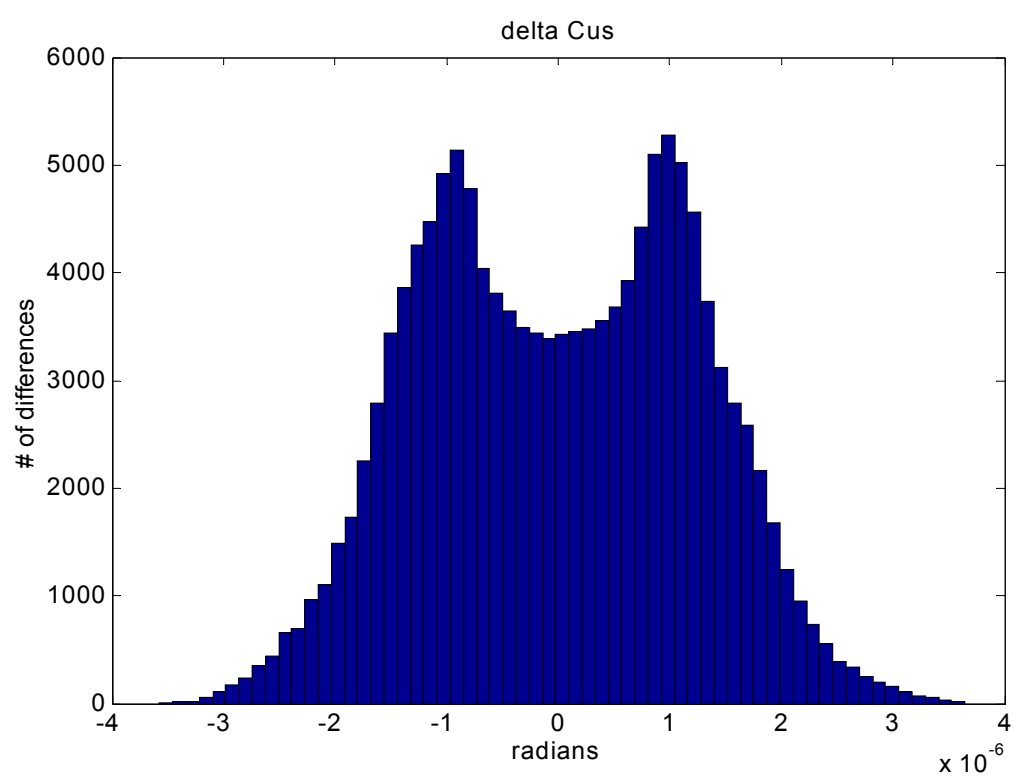


Figure B.8 Distribution of Differences in Cus From Day to Day

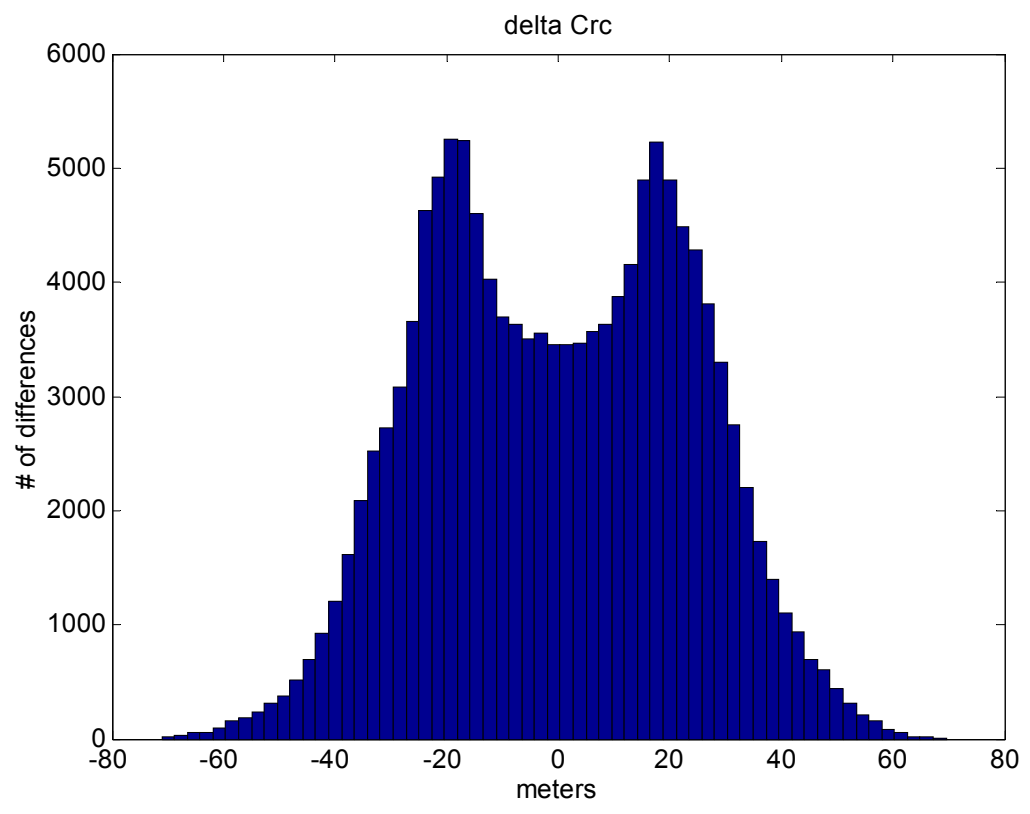


Figure B.9 Distribution of Differences in Crc From Day to Day

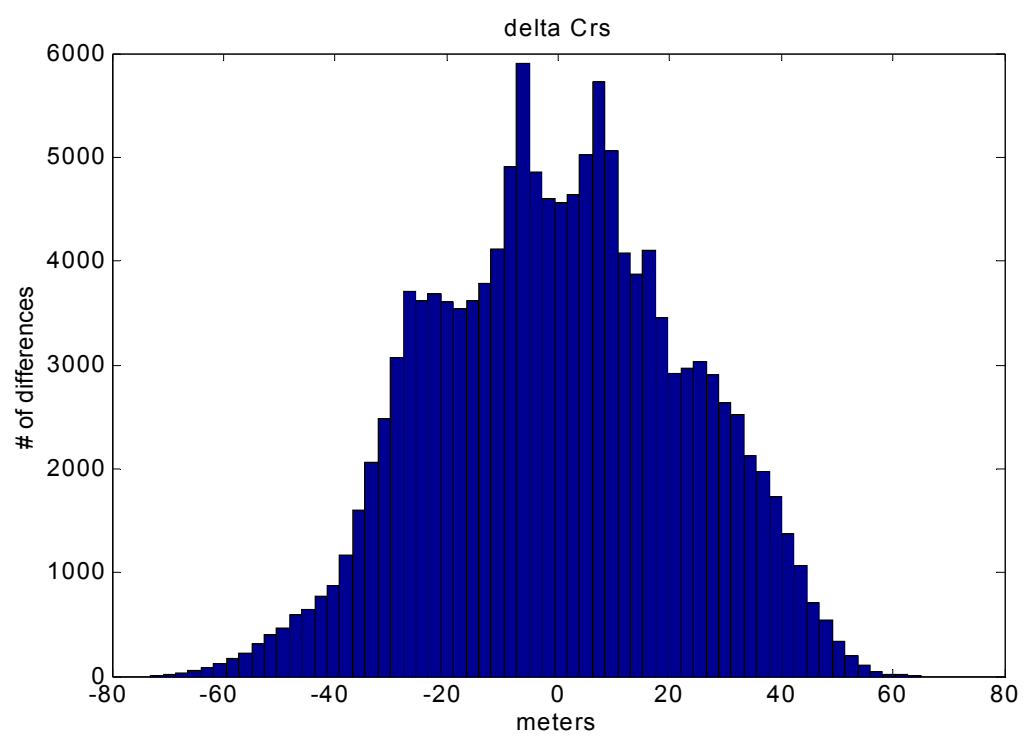


Figure B.10 Distribution of Differences in Crs From Day to Day

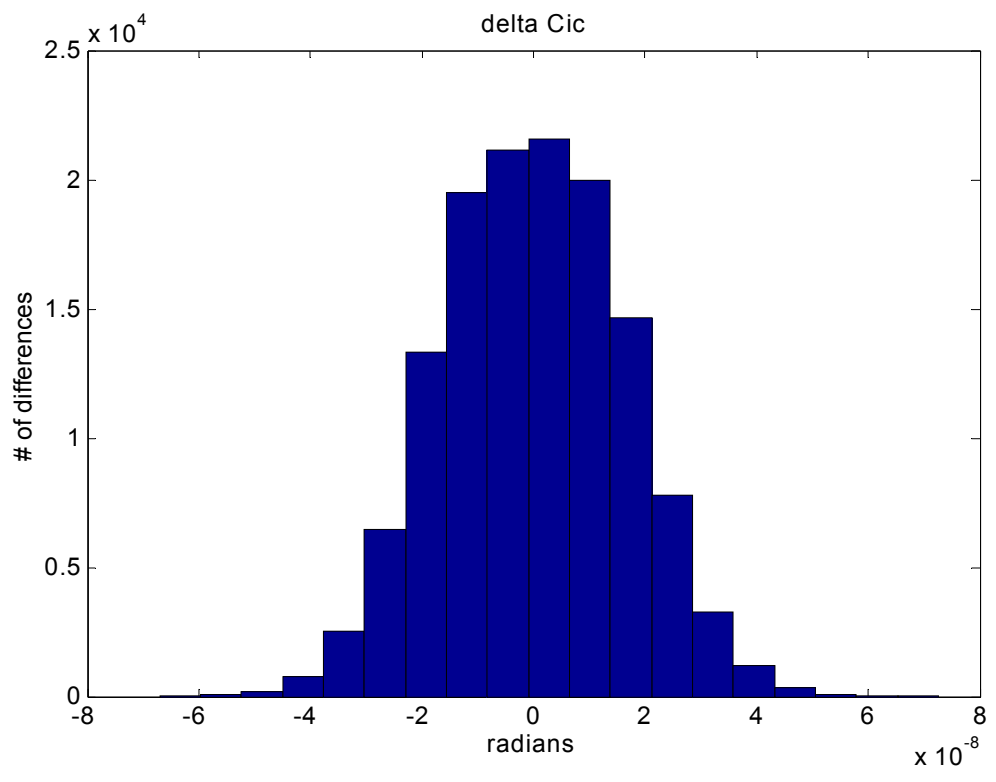


Figure B.11 Distribution of Differences in Cic From Day to Day

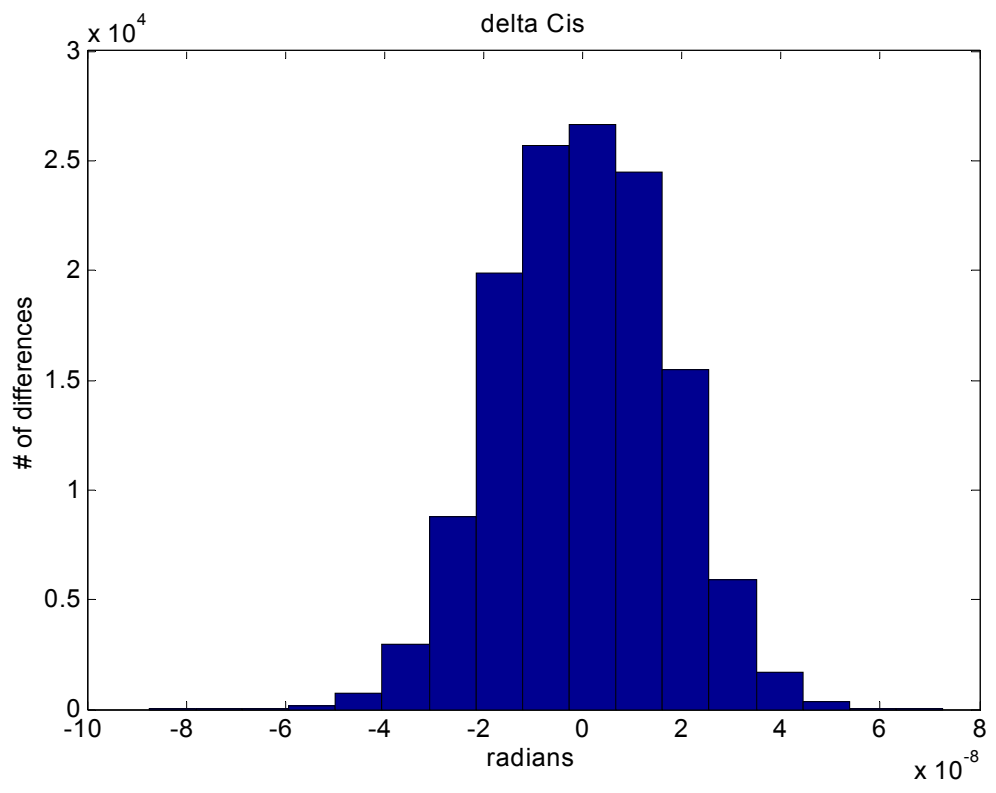


Figure B.12 Distribution of Differences in Cis From Day to Day

Standard Deviation Values for the difference of ephemeris parameters broadcasted 24 hs apart:

Mo	Deltan	e	a	Ω_0
1.1312e-003	9.2780e-011	3.2413e-006	2.0707e+001	1.4088e-005
io	ω	$\Omega \text{ dot}$	i dot	Cuc
1.0267e-005	1.1311e-003	8.5925e-011	1.1565e-010	1.1687e-006
Cus	Crc	Crs	Cic	Cis
1.2167e-006	2.3449e+001	2.2529e+001	1.6446e-008	1.6538e-008
Mo+ω				
2.0535e-005				

APPENDIX C

SATELLITE POSITION SENSITIVITY TO BROADCASTED EPHEMERIS PARAMETERS VARIATIONS

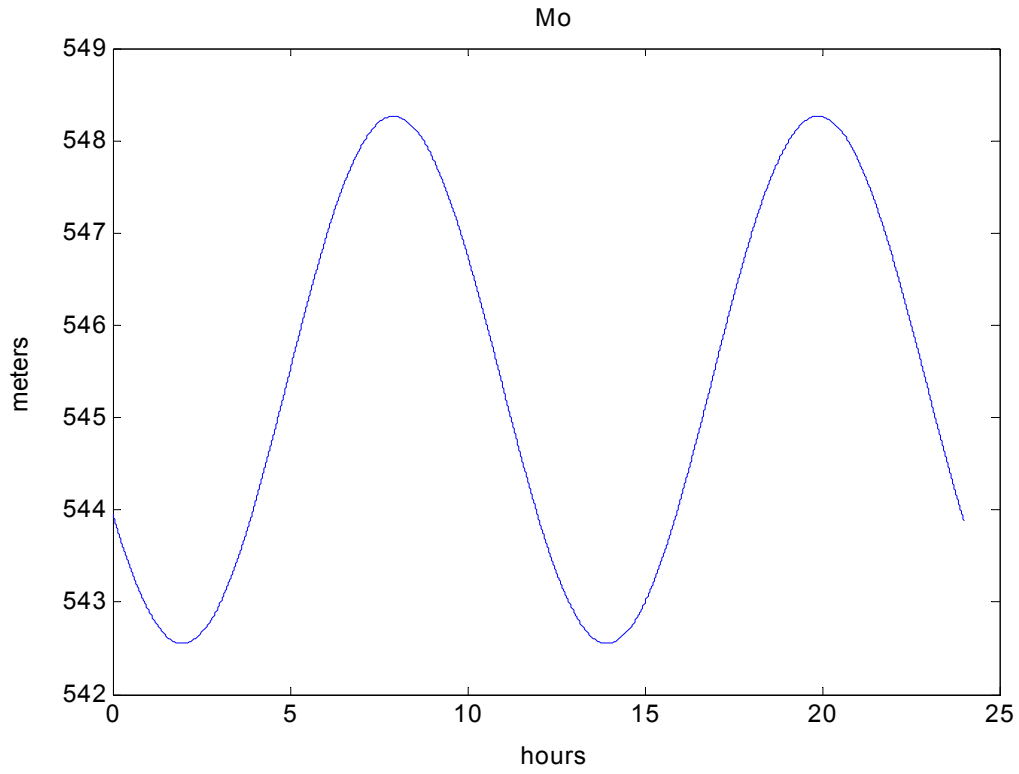


Figure C.1 One Sigma Position Difference due to Day to Day Changes in M_o

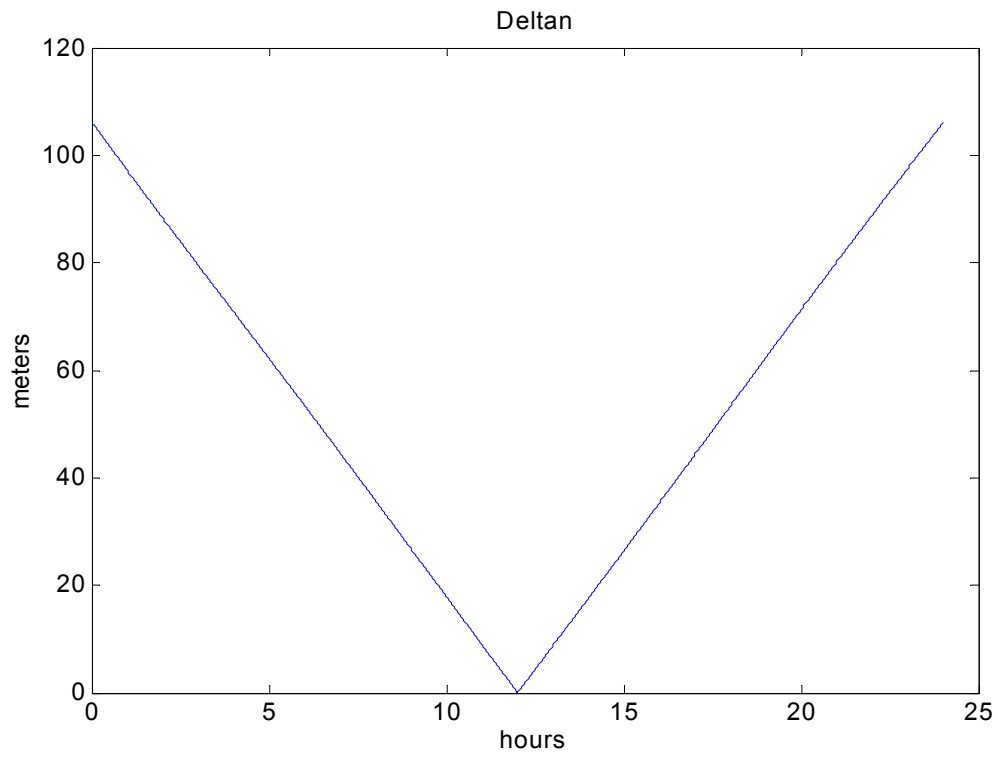


Figure C.2 One Sigma Position Difference due to Day to Day Changes in Δn

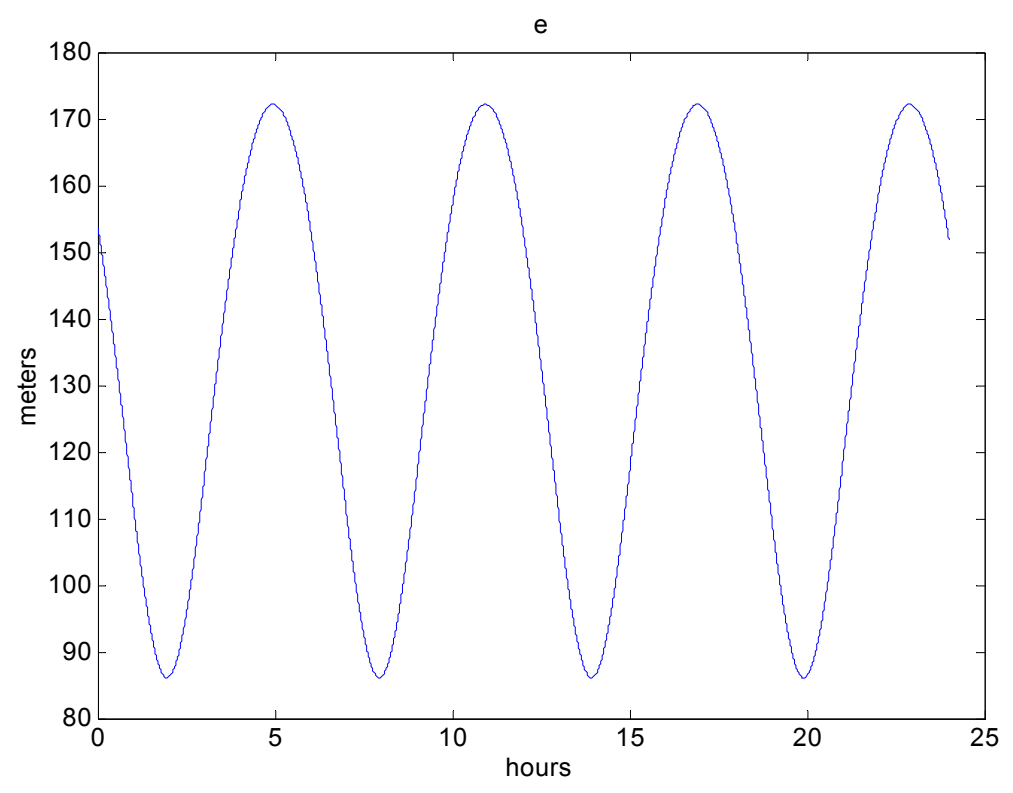


Figure C.3 One Sigma Position Difference due to Day to Day Changes in e

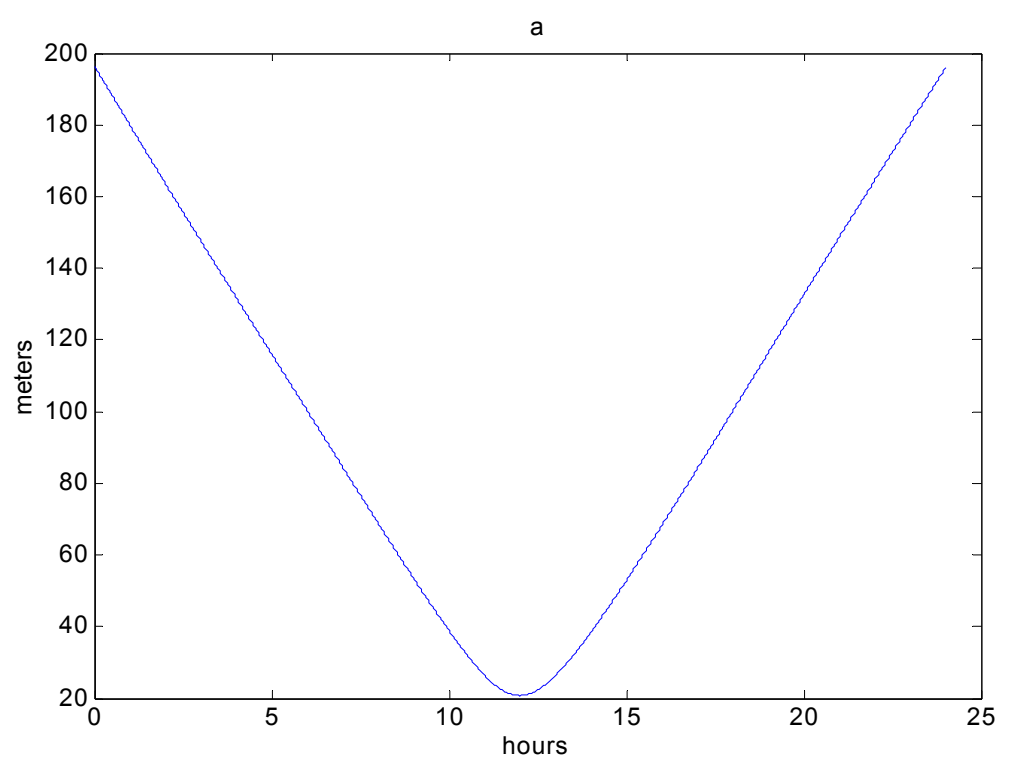


Figure C.4 One Sigma Position Difference due to Day to Day Changes in a

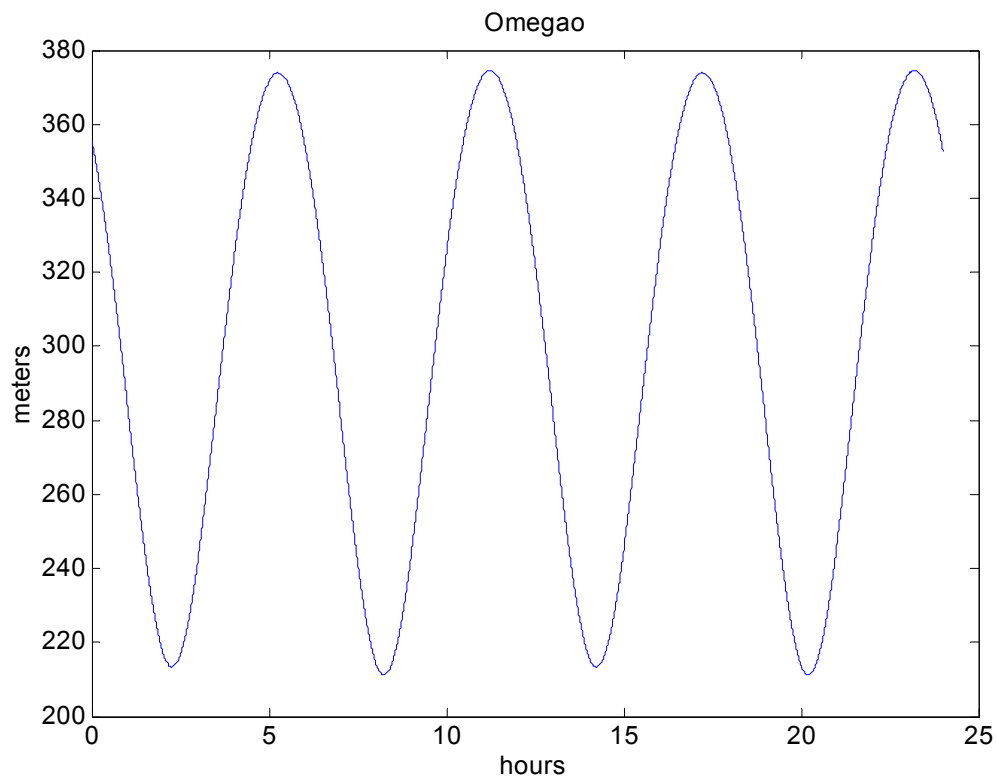


Figure C.5 One Sigma Position Difference due to Day to Day Changes in Ω_0

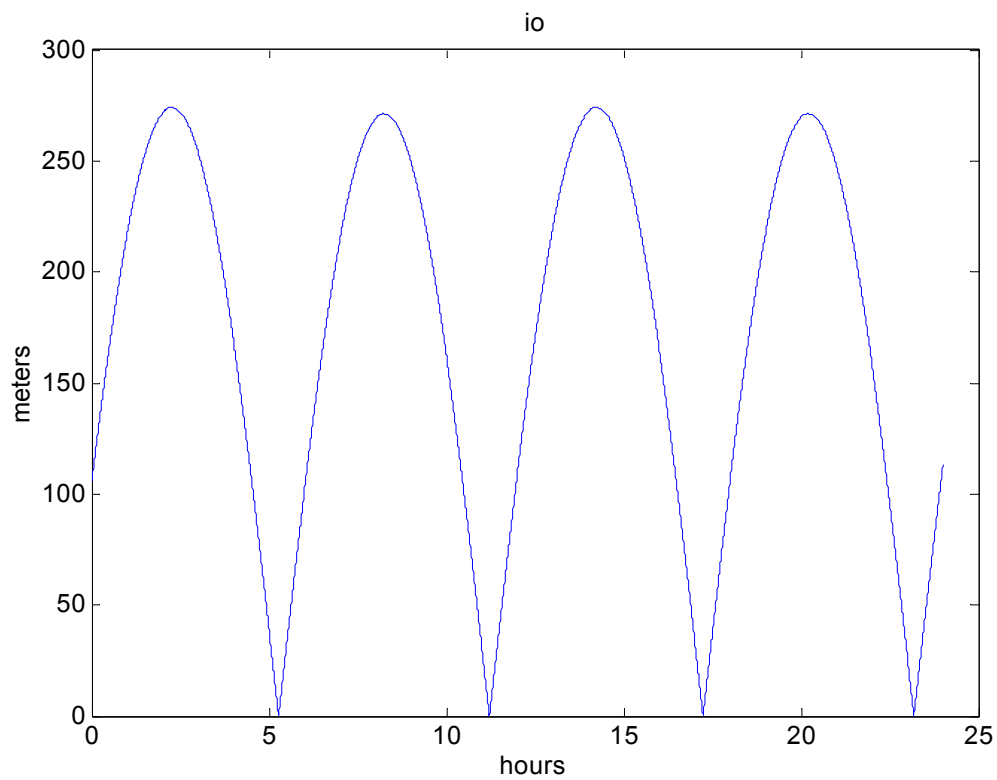


Figure C.6 One Sigma Position Difference due to Day to Day Changes in i_0

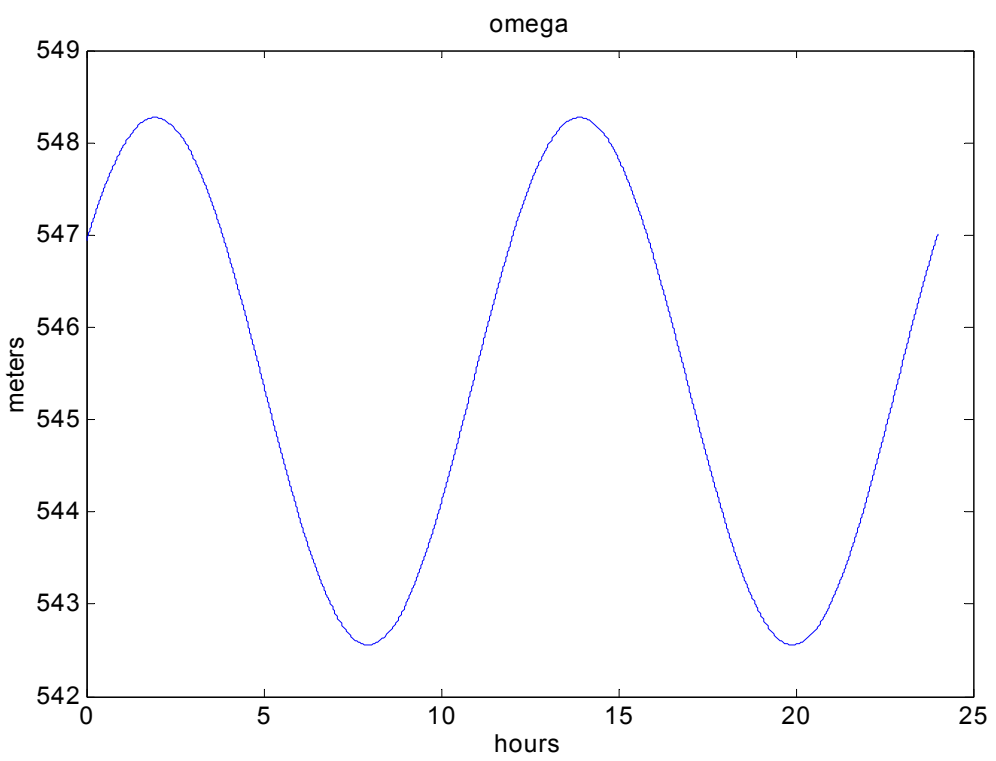


Figure C.7 One Sigma Position Difference due to Day to Day Changes in ω

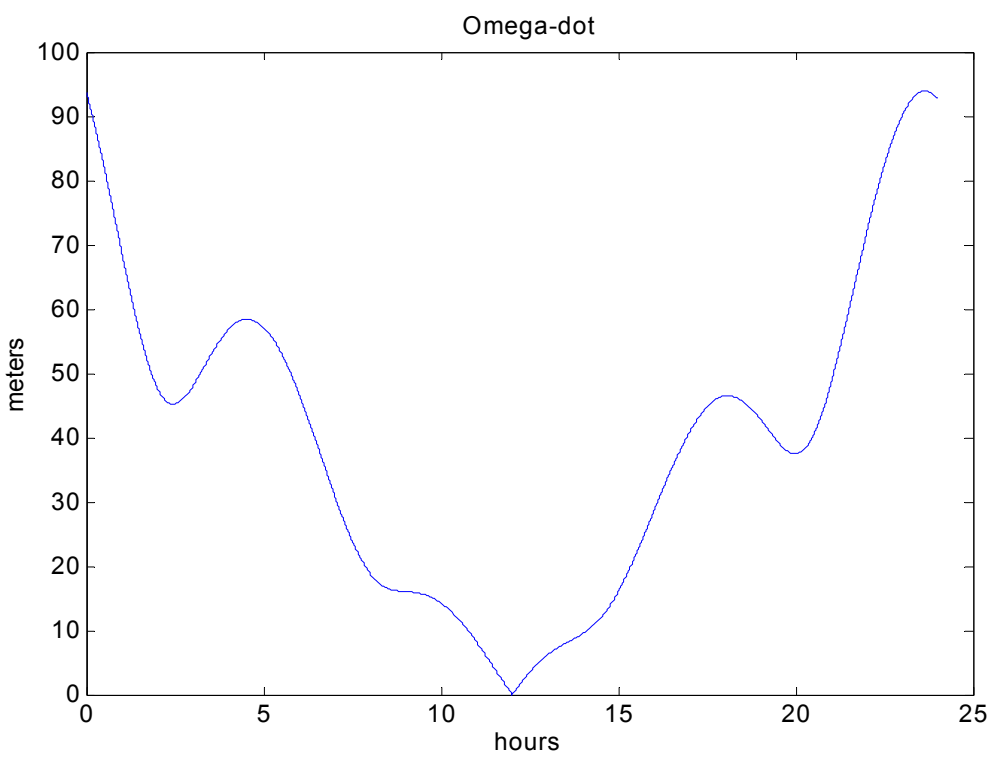


Figure C.8 One Sigma Position Difference due to Day to Day Changes in $\Omega\dot{\omega}$

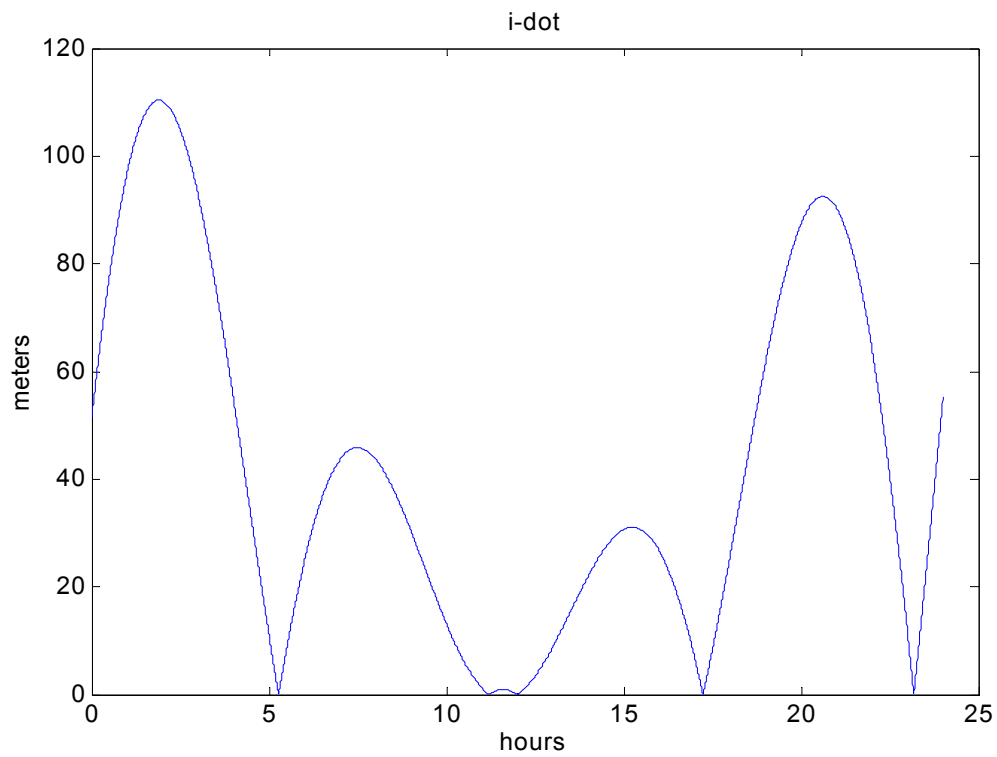


Figure C.9 One Sigma Position Difference due to Day to Day Changes in $i\text{-dot}$.

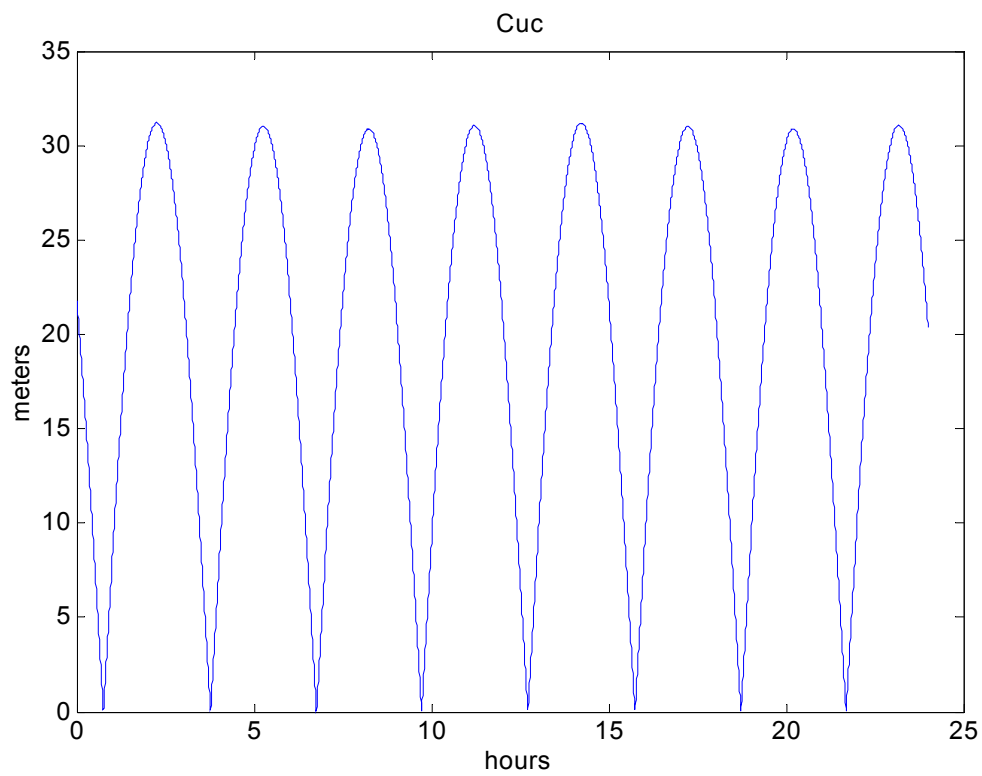


Figure C.10 One Sigma Position Difference due to Day to Day Changes in Cuc

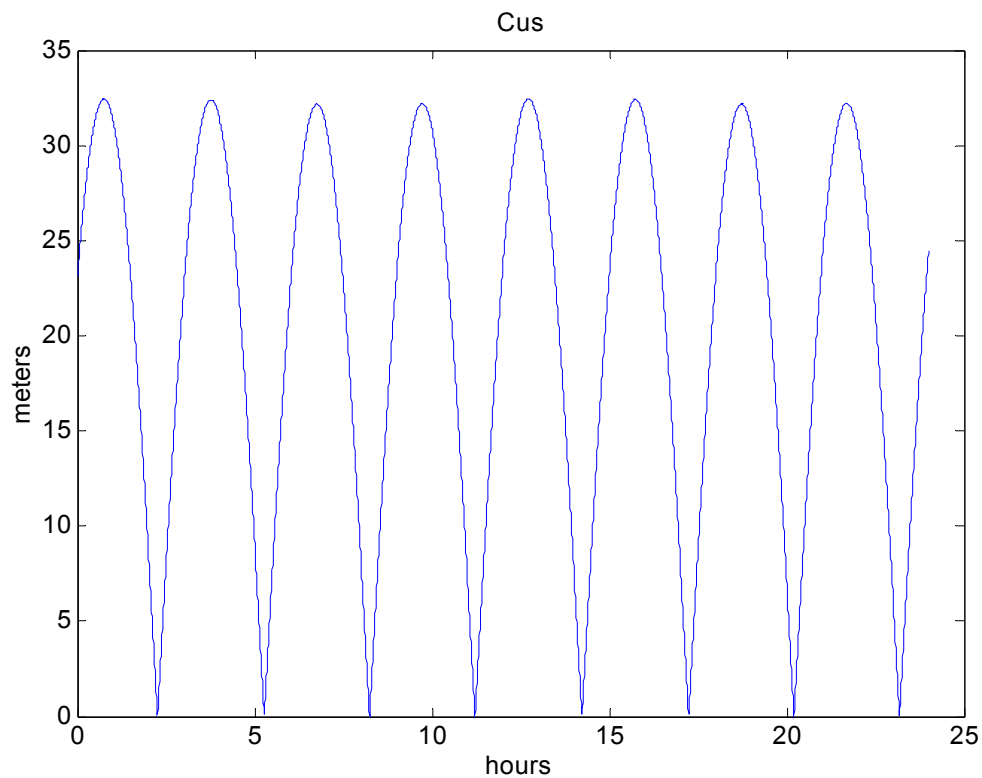


Figure C.11 One Sigma Position Difference due to Day to Day Changes in Cus

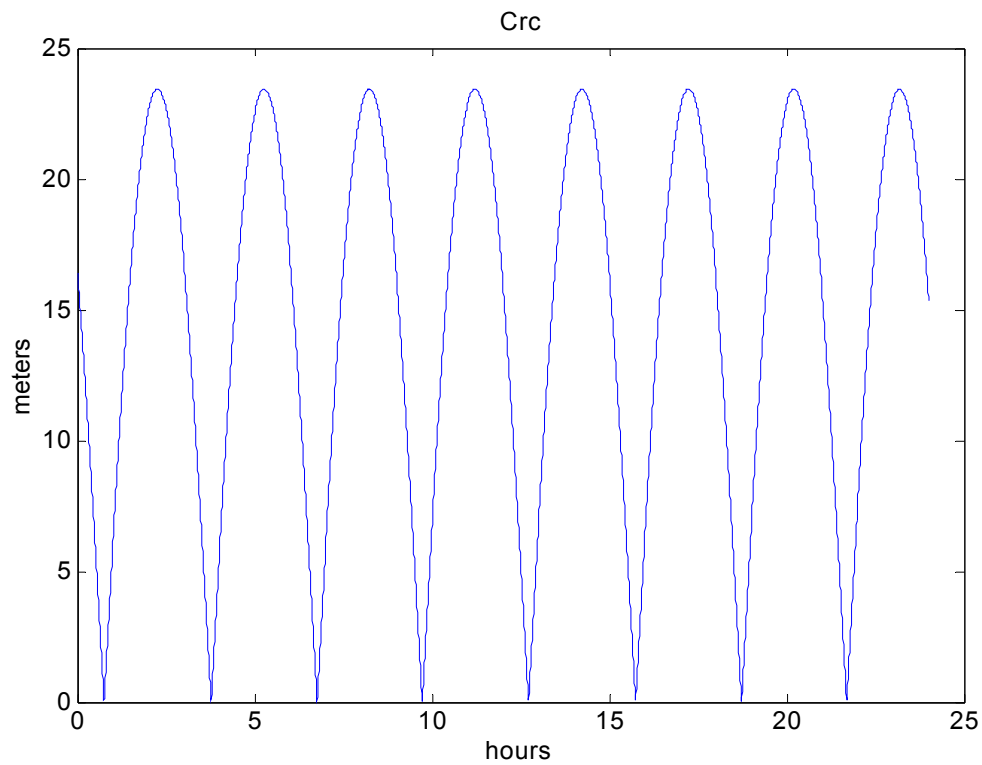


Figure C.12 One Sigma Position Difference due to Day to Day Changes in Crc

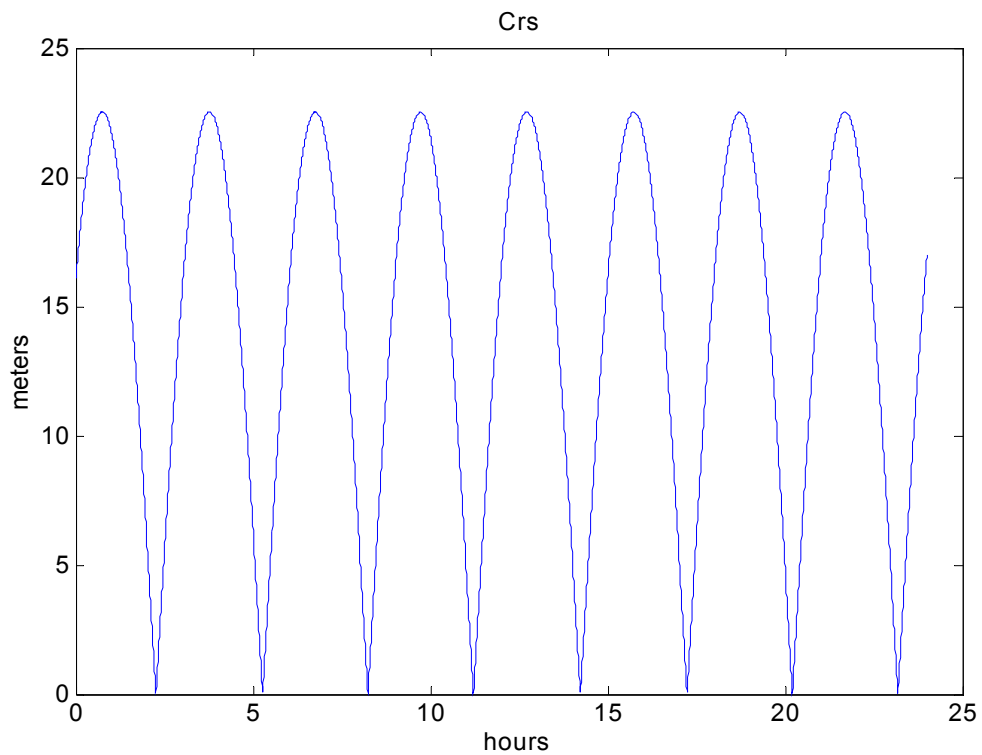


Figure C.13 One Sigma Position Difference due to Day to Day Changes in Crs

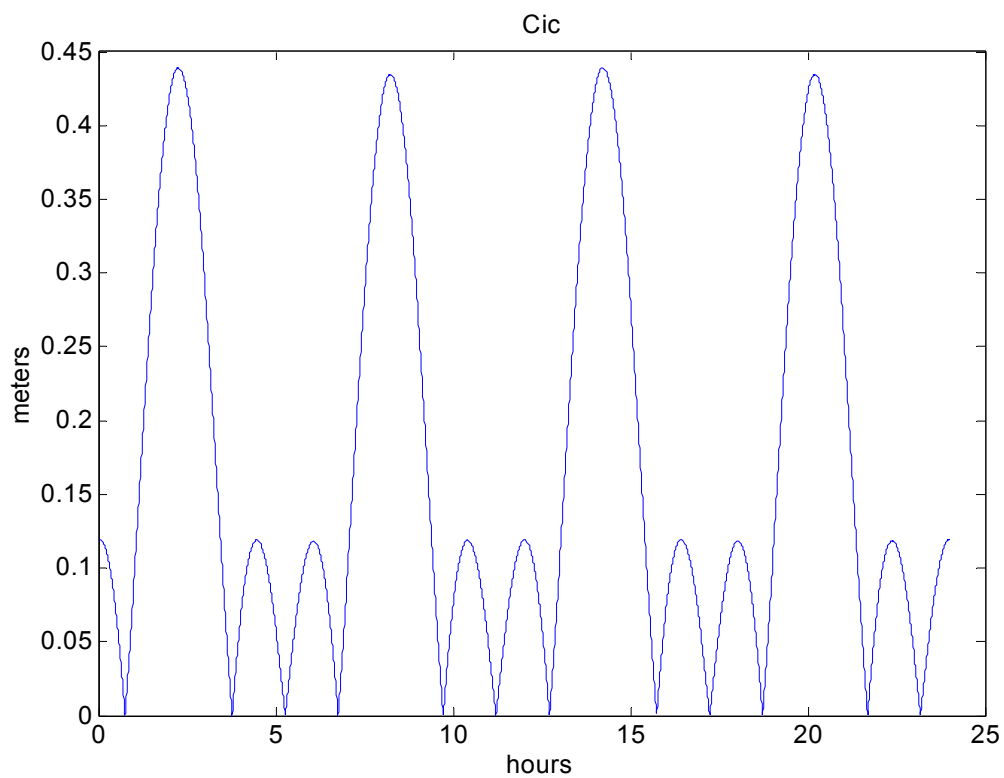


Figure C.14 One Sigma Position Difference due to Day to Day Changes in Cic

F

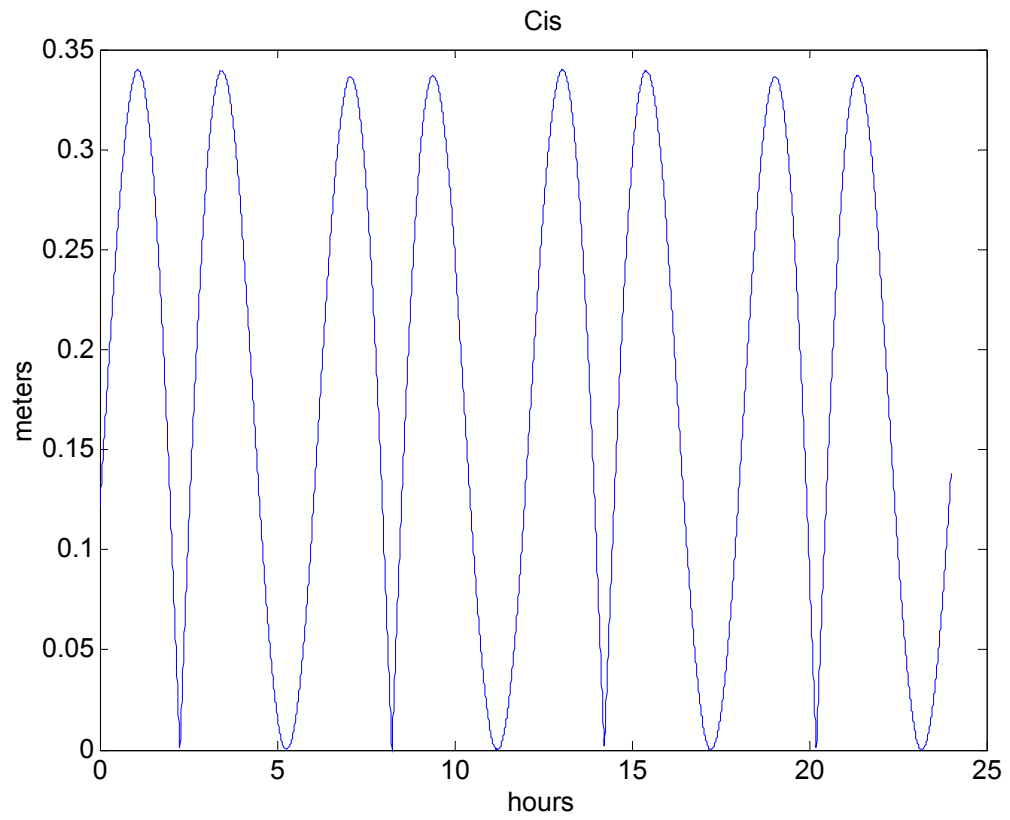


Figure C.15 One Sigma Position Difference due to Day-to-Day Changes in Cis

APPENDIX D
EPHEMERIS PARAMETER VALUES

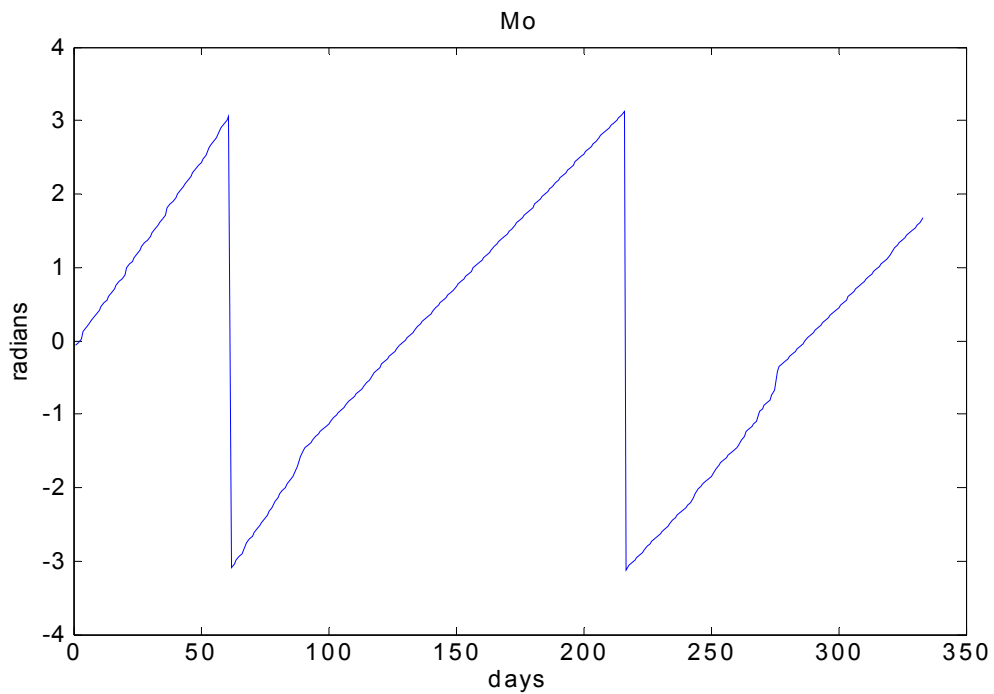
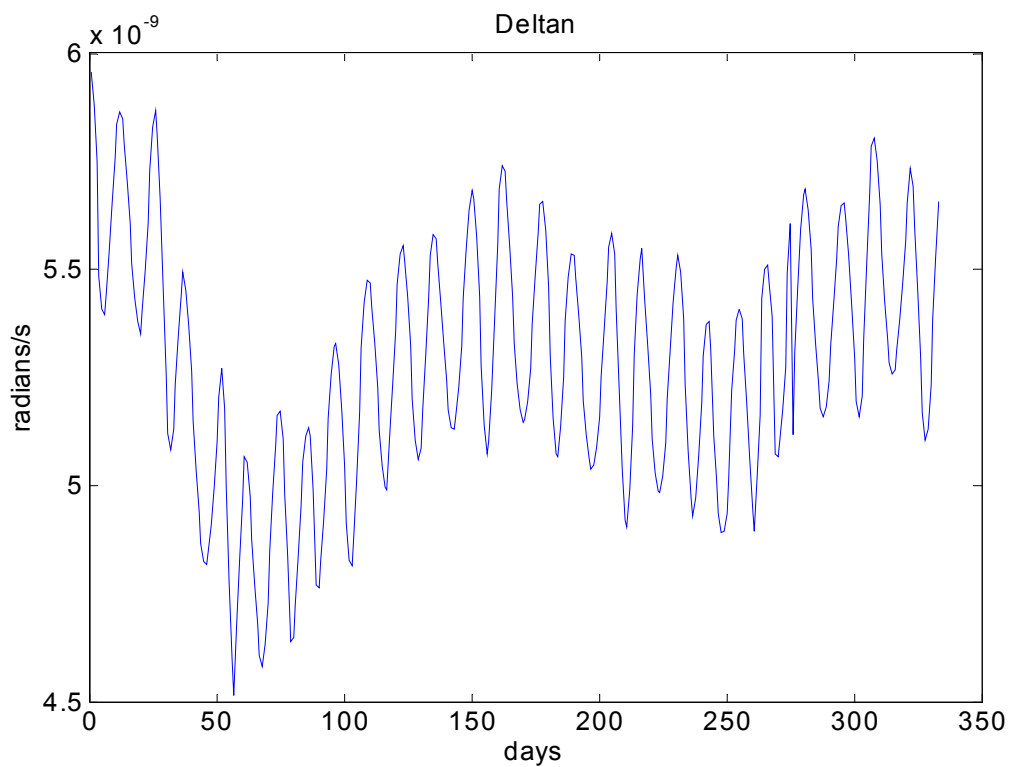


Figure D.1 Mo Values for PRN 2 Year 2002

Figure D.2 Δn Values for PRN 2 Year 2002

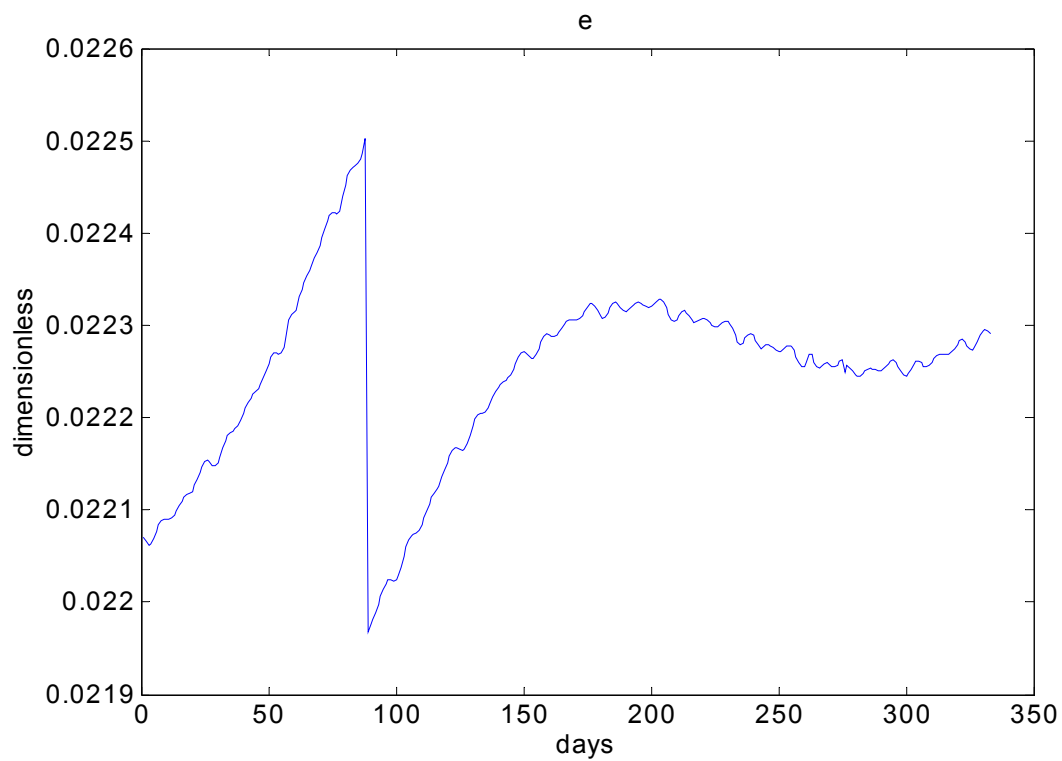


Figure D.3 Eccentricity Values for PRN 2 Year 2002

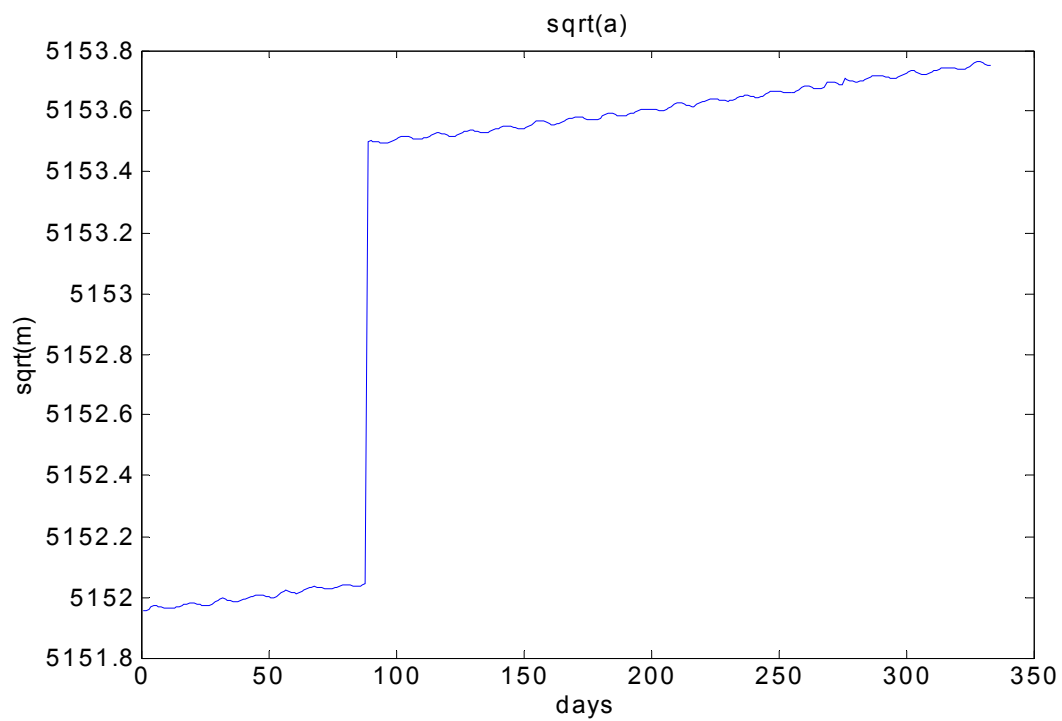


Figure D.4 Square Root of a Values for PRN 2 Year 2002

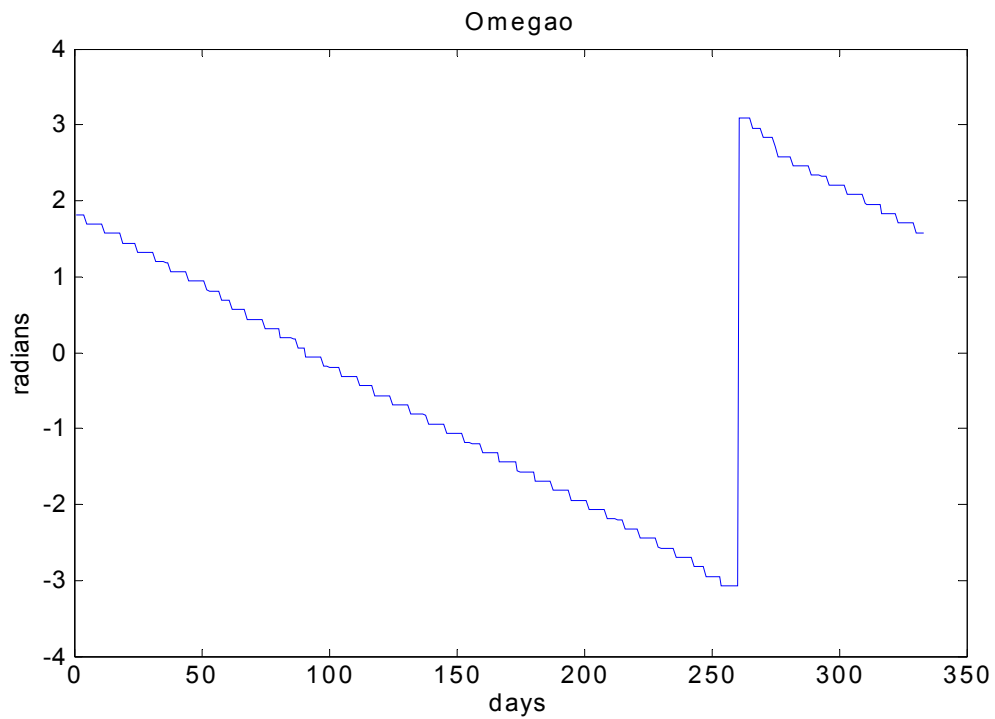
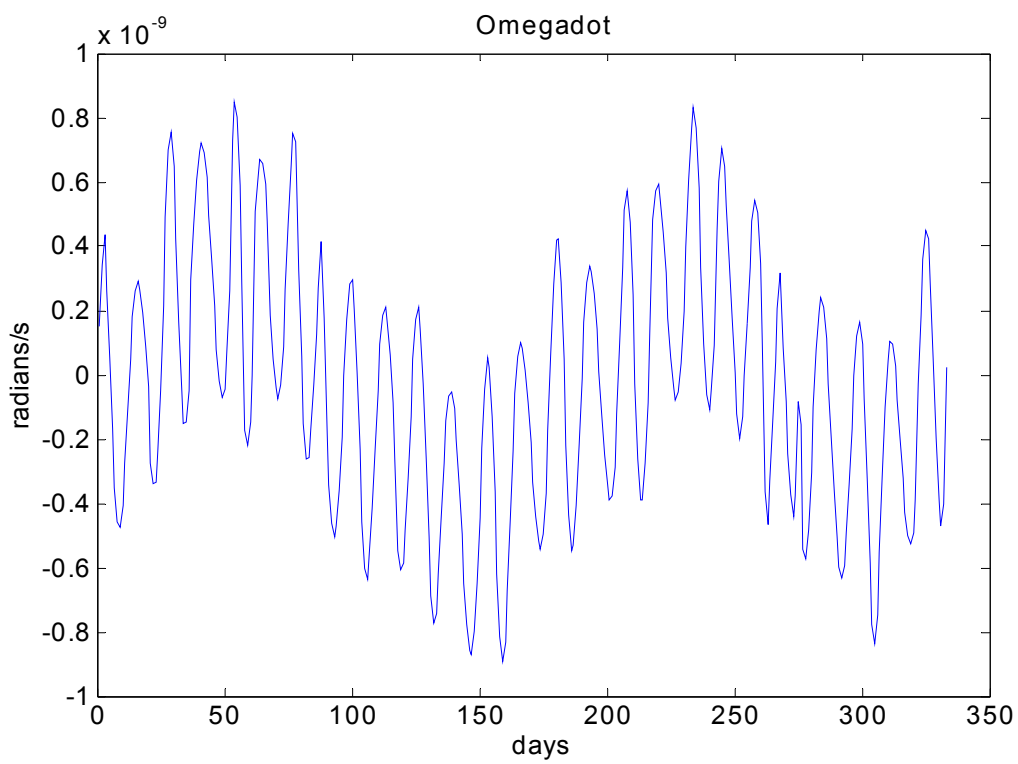
Figure D.5 Ω_0 Values for PRN 2 Year 2002

Figure D.6 Omegadot Values for PRN 2 Year 2002

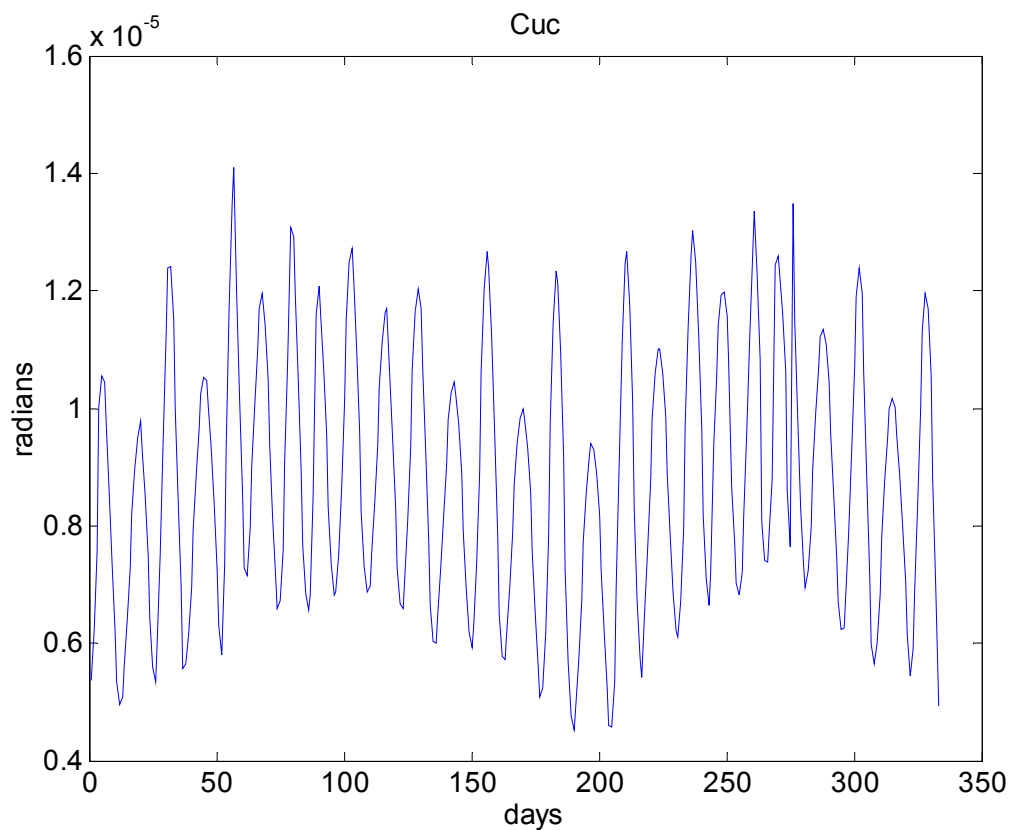


Figure D.7 Cuc Values for PRN 2 Year 2002

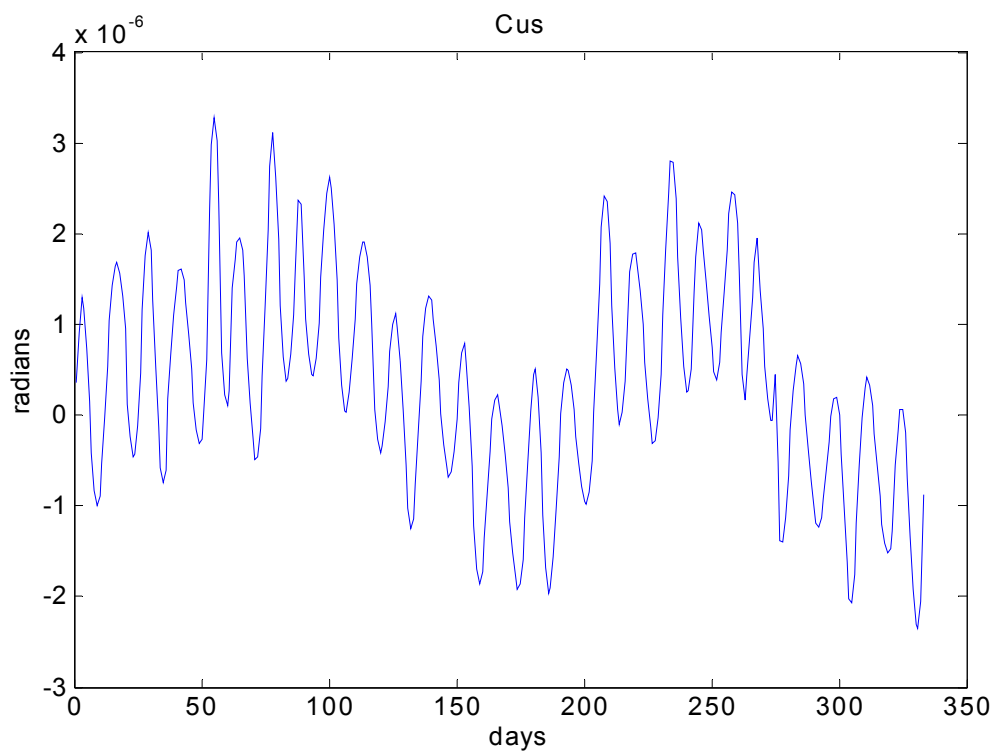


Figure D.8 Cus Values for PRN 2 Year 2002

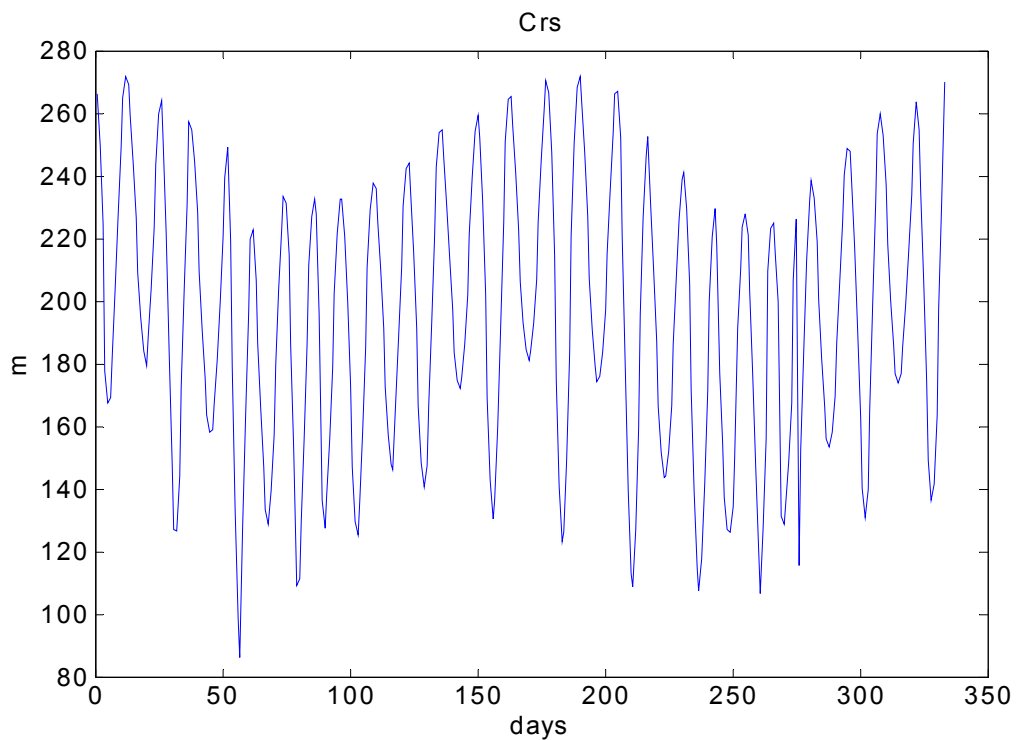


Figure D.9 Crs Values for PRN 2 Year 2002

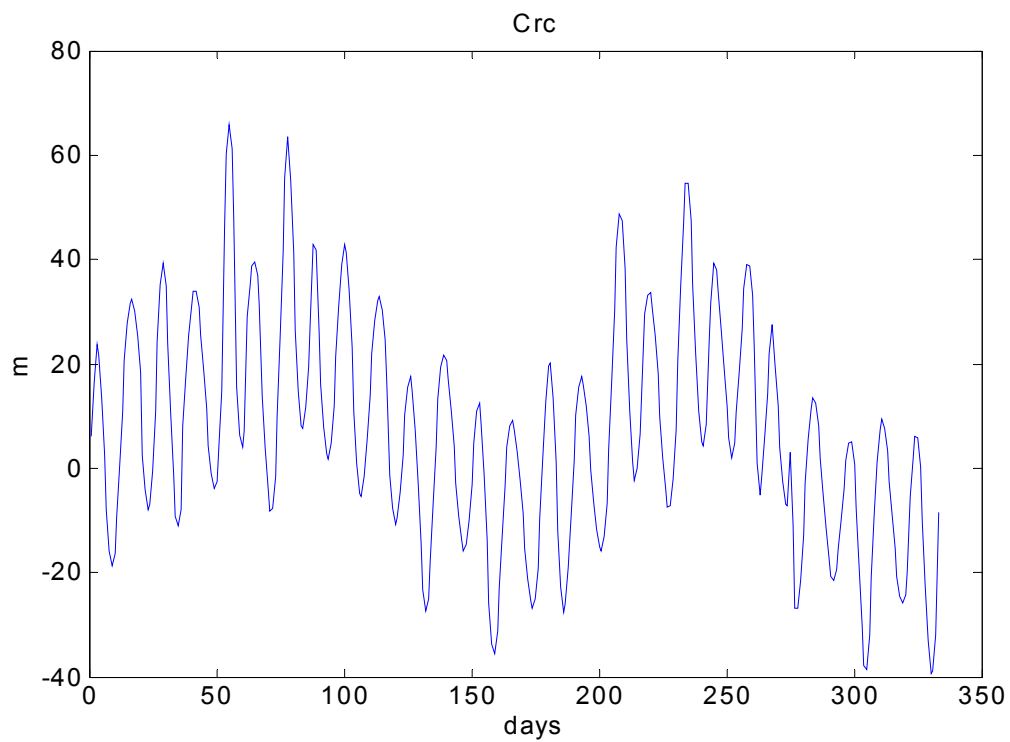


Figure D.10 Crc Values for PRN 2 Year 2002

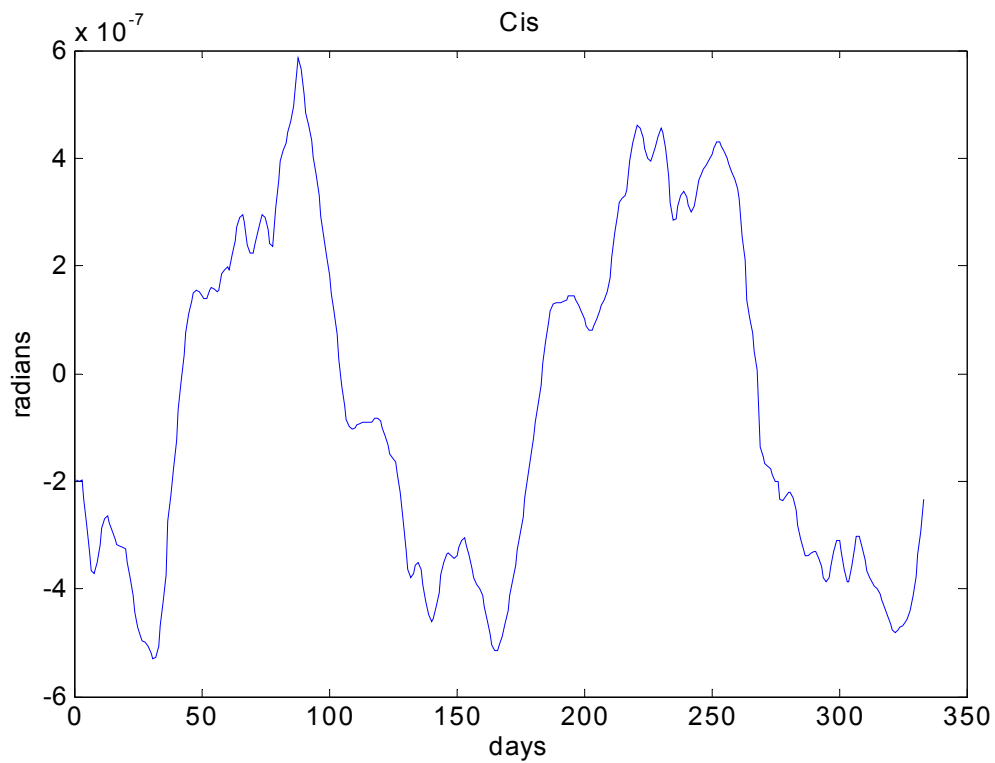


Figure D.11 Cis Values for PRN 2 Year 2002

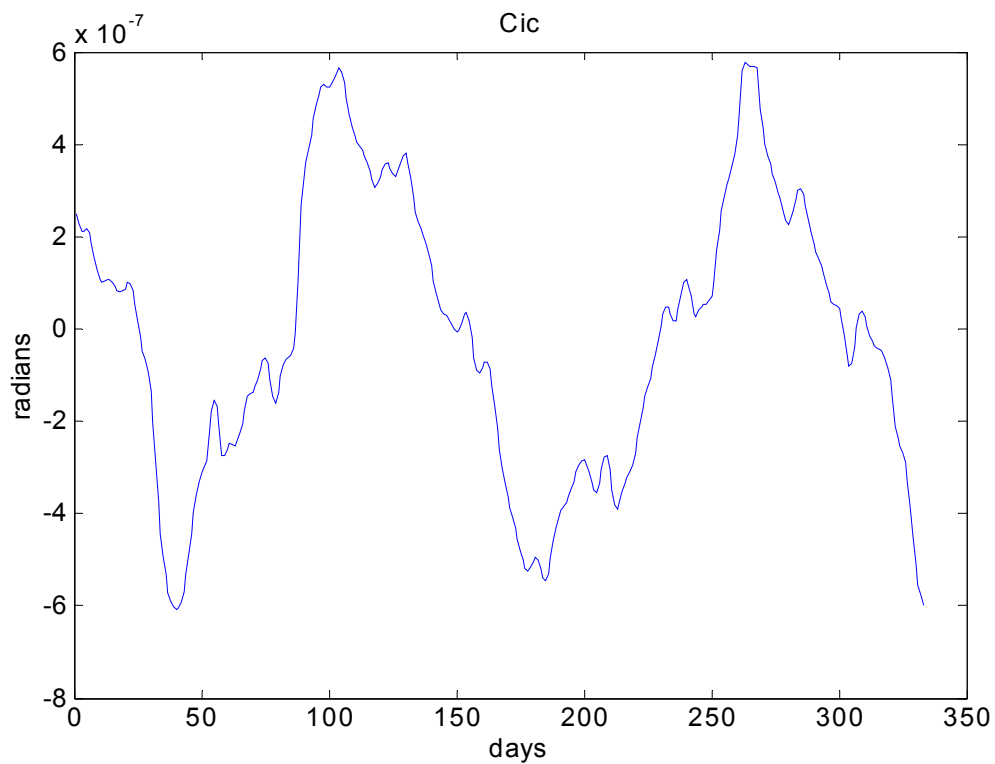


Figure D.12 Cic Values for PRN 2 Year 2002

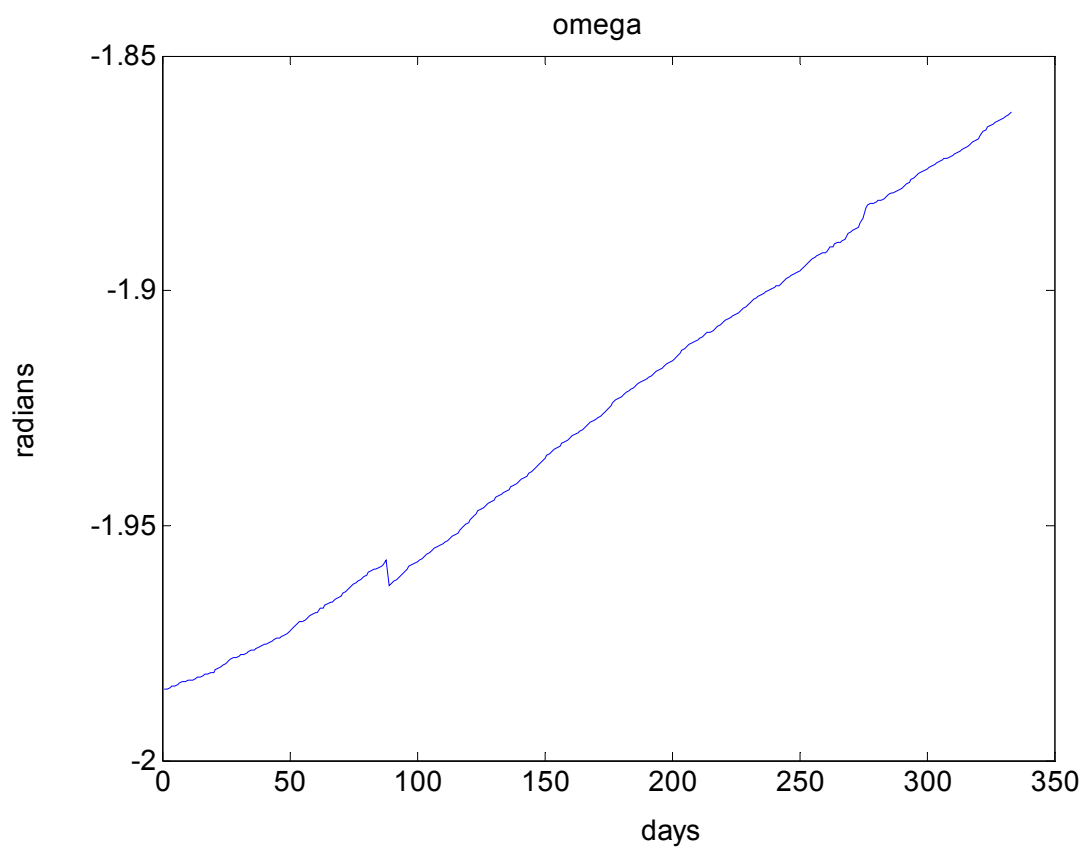


Figure D.13 ω Values for PRN 2 Year 2002

APPENDIX E

P₀ Parameter Values Update Formulas for Secular Effects

$$\begin{aligned}
 i_o^* &= i_{o_{k-1d}} + i_{\dot{o}_{k-1d}} 24\text{hs} \\
 \Omega_{o_{k-1d}}^* &= \Omega_{o_{k-1d}} + \Omega_{\dot{o}_{k-1d}} 24\text{hs} \\
 M_{o_{k-1d}}^* &= M_{o_{k-1d}} + (\sqrt{\mu}/a^3 + \Delta t_{\text{an}}) 24\text{hs} - 4\pi
 \end{aligned}$$

When there is a Saturday night crossover:

$$\Omega_{o_{k-1d}}^* = \Omega_{o_{k-1d}} + \Omega_{\dot{o}_{k-1d}} 24\text{hs} - 2\pi(24\text{hs} - \text{sidereal day}) / \text{sidereal day}$$

Where:

$$\mu = 3.986005 \times 10^{14} \text{ m}^3/\text{s}^2$$

$$\text{sidereal day} = 86164.09054 \text{ s}$$

APPENDIX F

Parameter Differences 24hs Apart

For PRN 2, Jan/June year 2002. For Po the difference shown is from “today” to “yesterday updated” with formulas in appendix F.

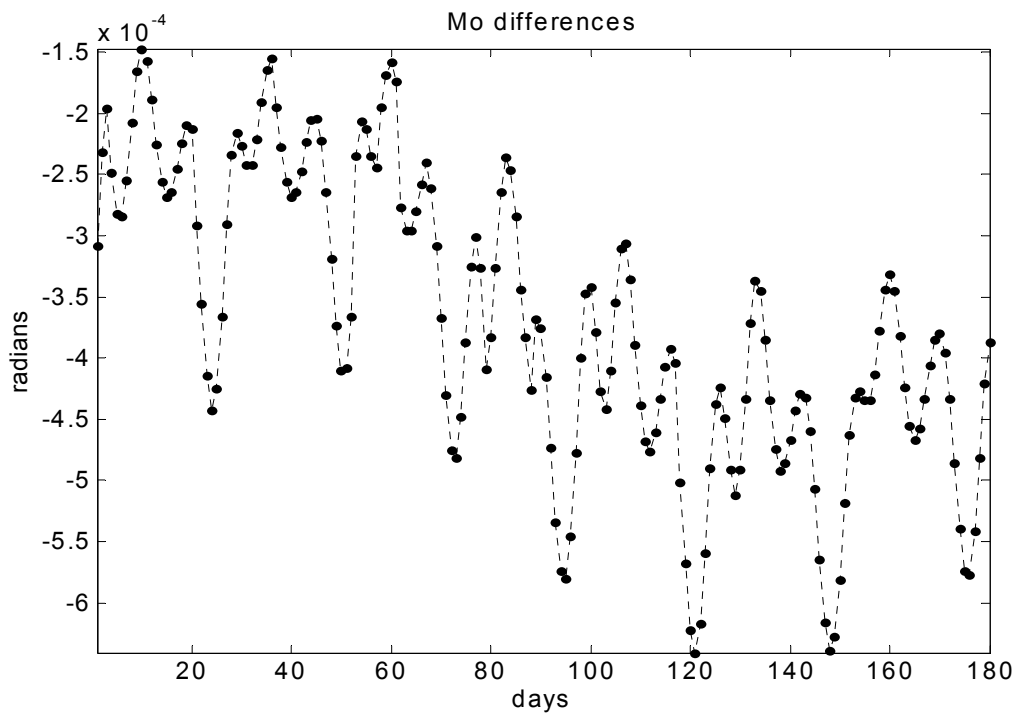


Figure F.1 Mo Differences Day to Day

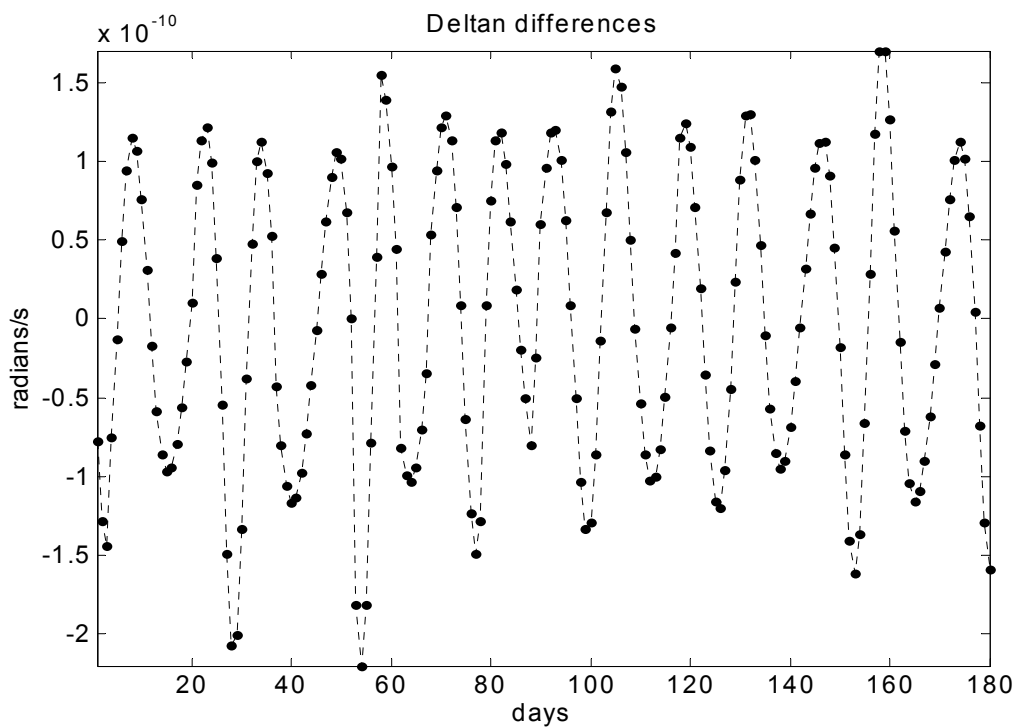


Figure F.2 Deltan Differences Day to Day

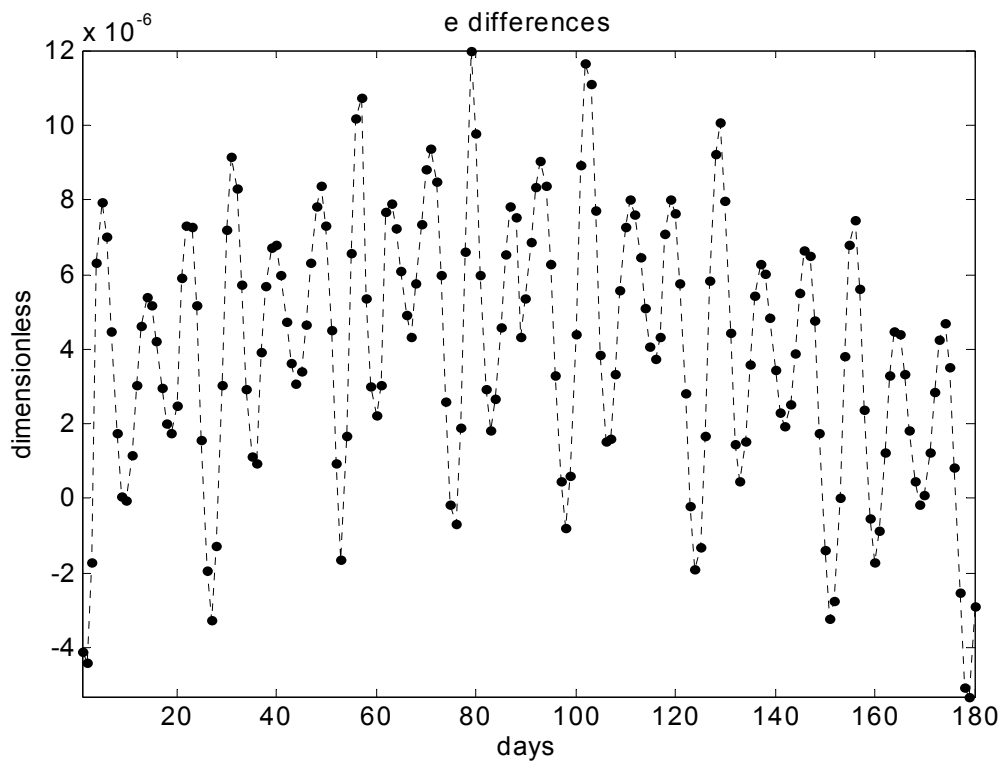


Figure F.3 e Differences Day to Day

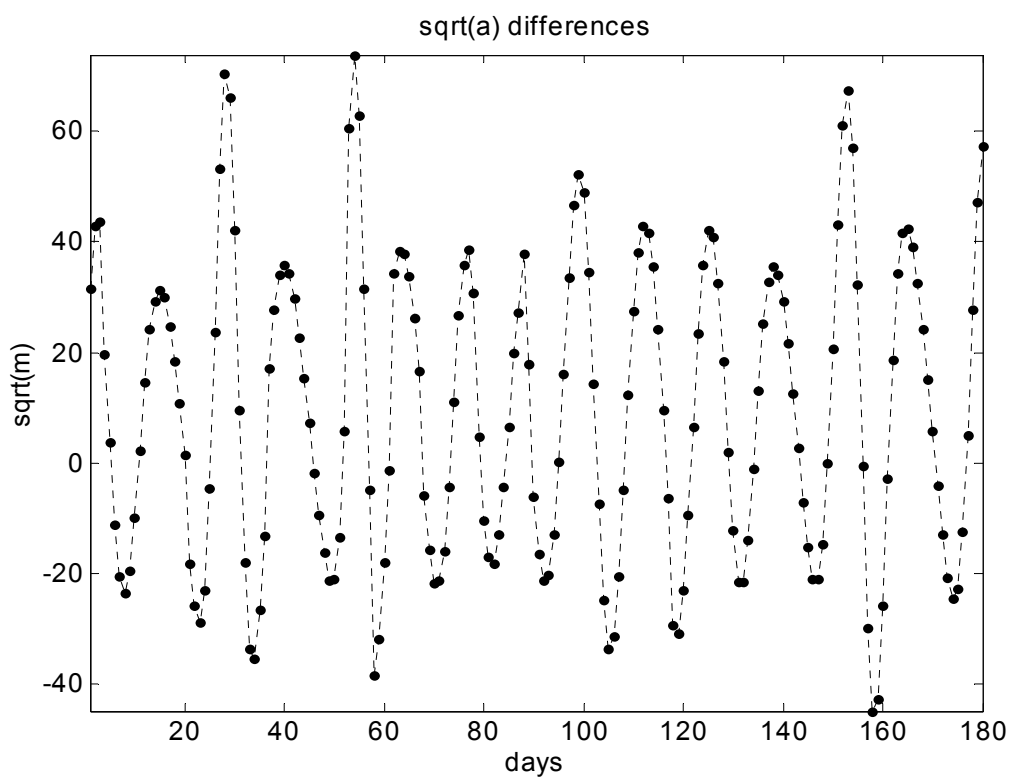
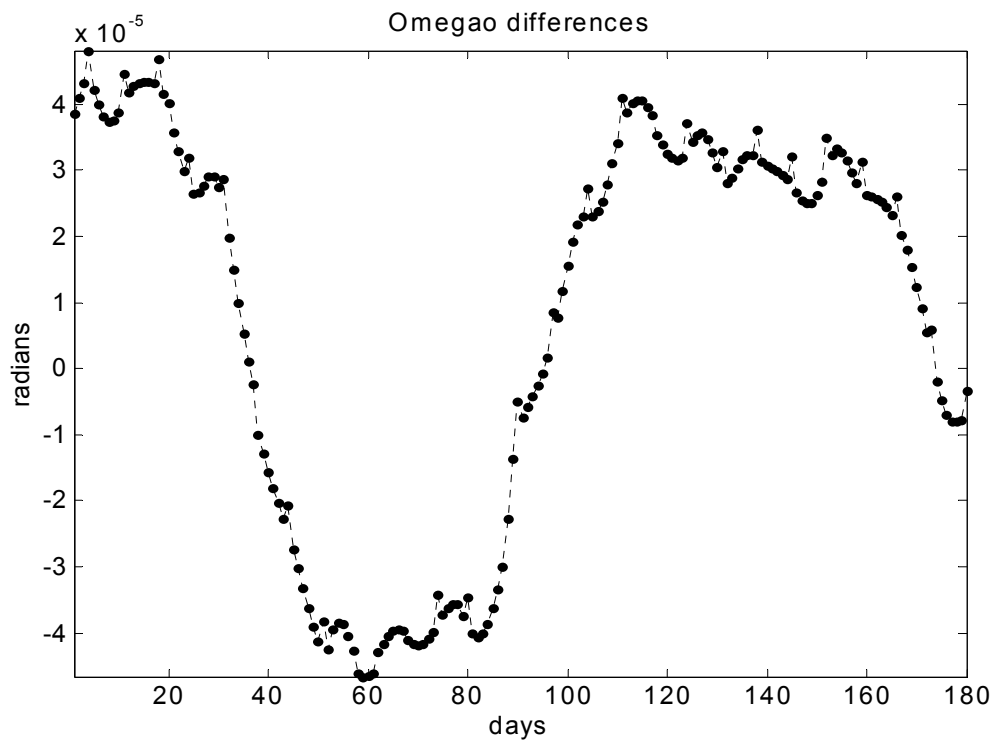
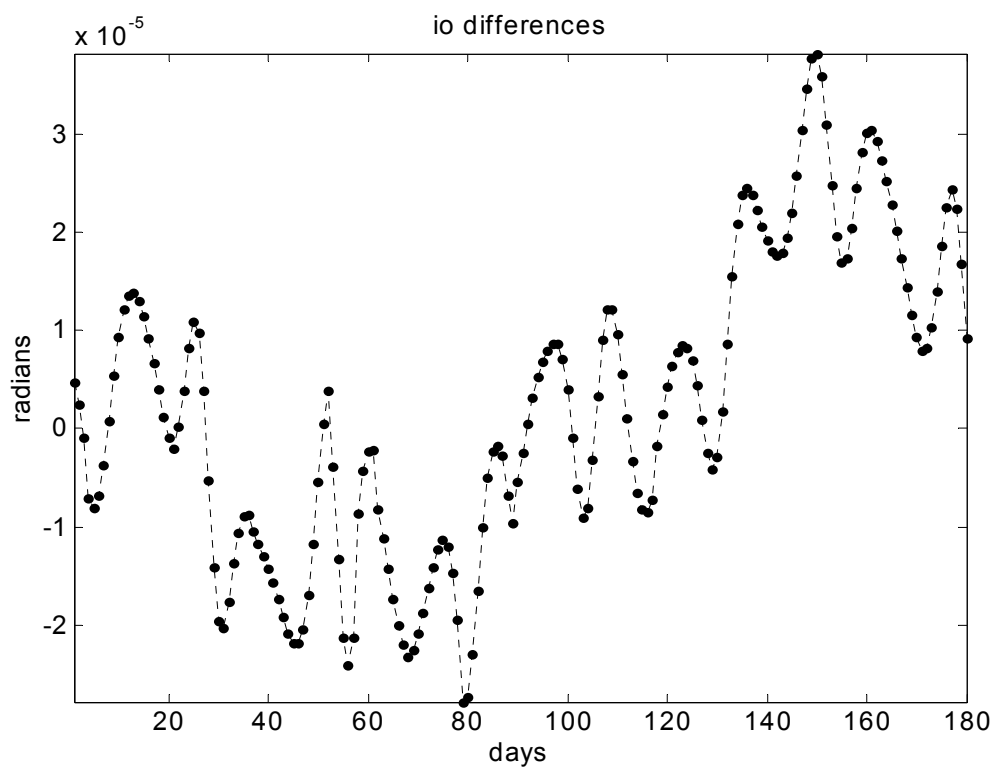


Figure F.4 sqrt(a) Differences Day to Day

Figure F.5 Ω_0 Differences Day to DayFigure F.6 i_o Differences Day to Day

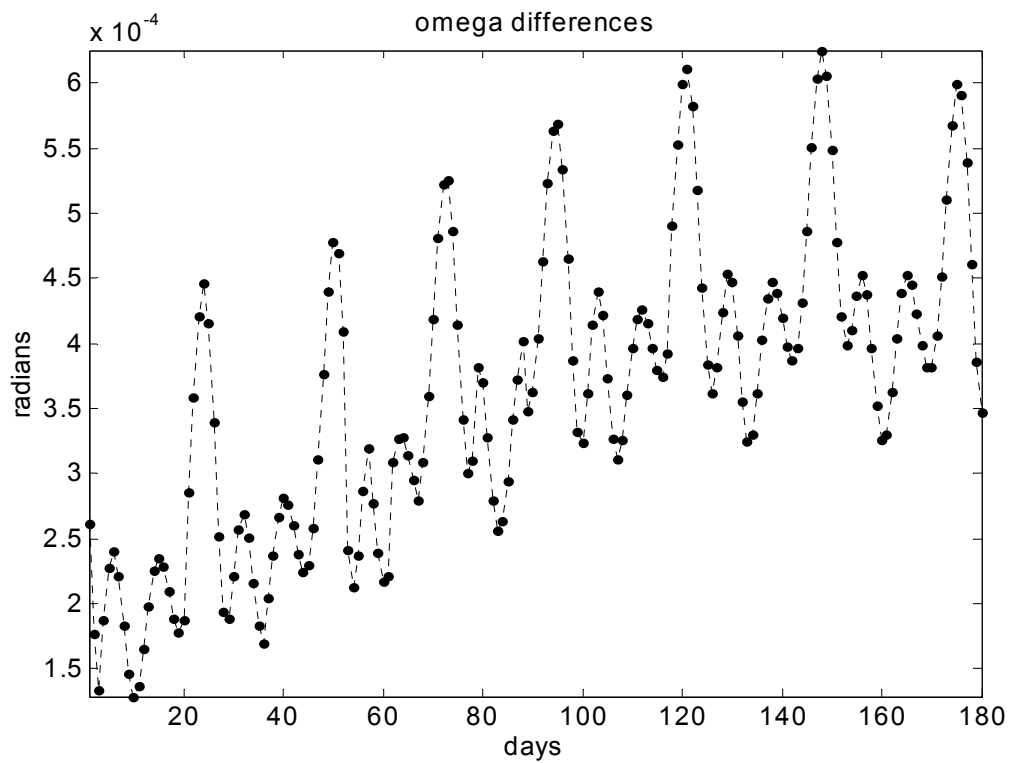


Figure F.7 omega Differences Day to Day

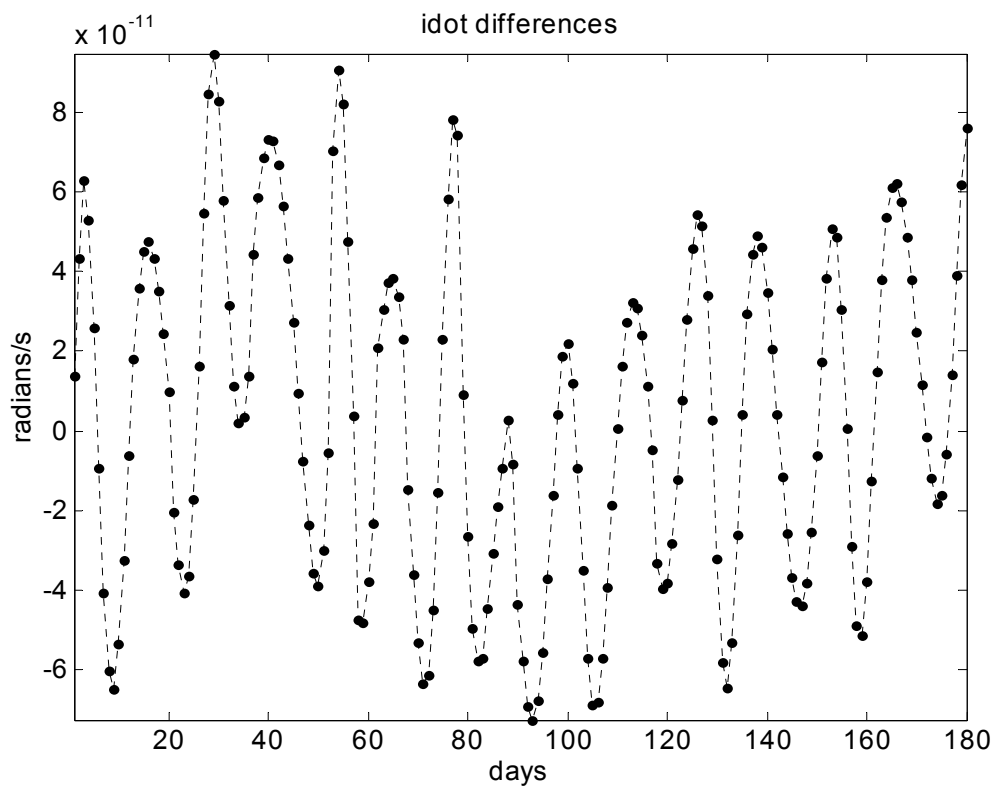


Figure F.8 idot Differences Day to Day

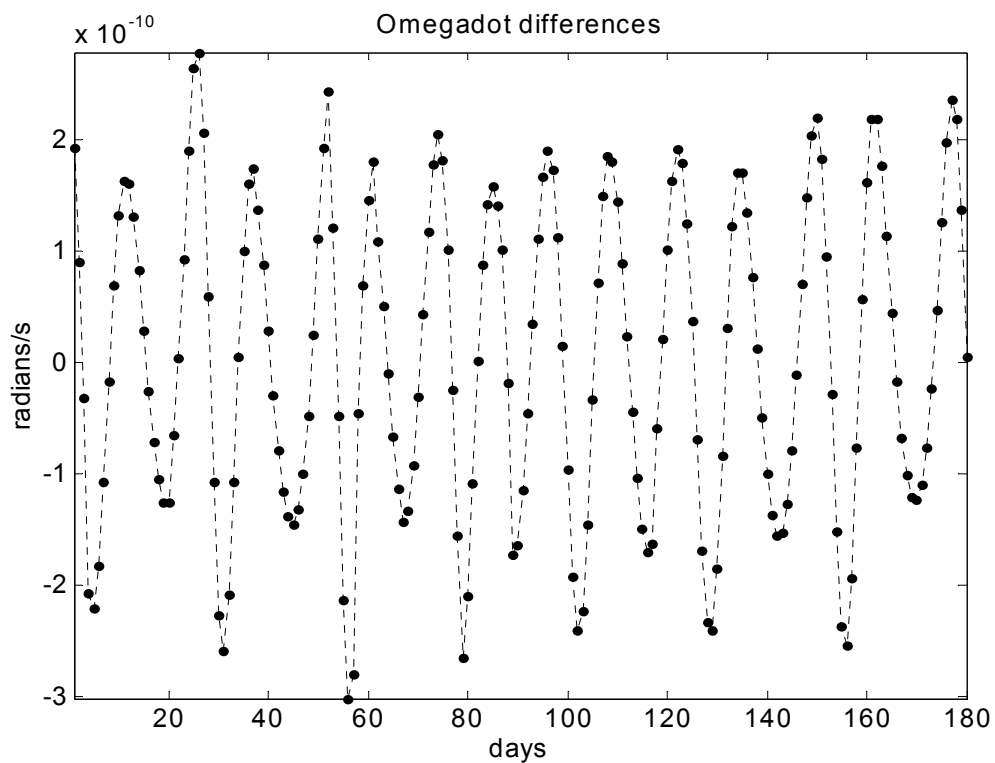


Figure F.9 Omegadot Differences Day to Day

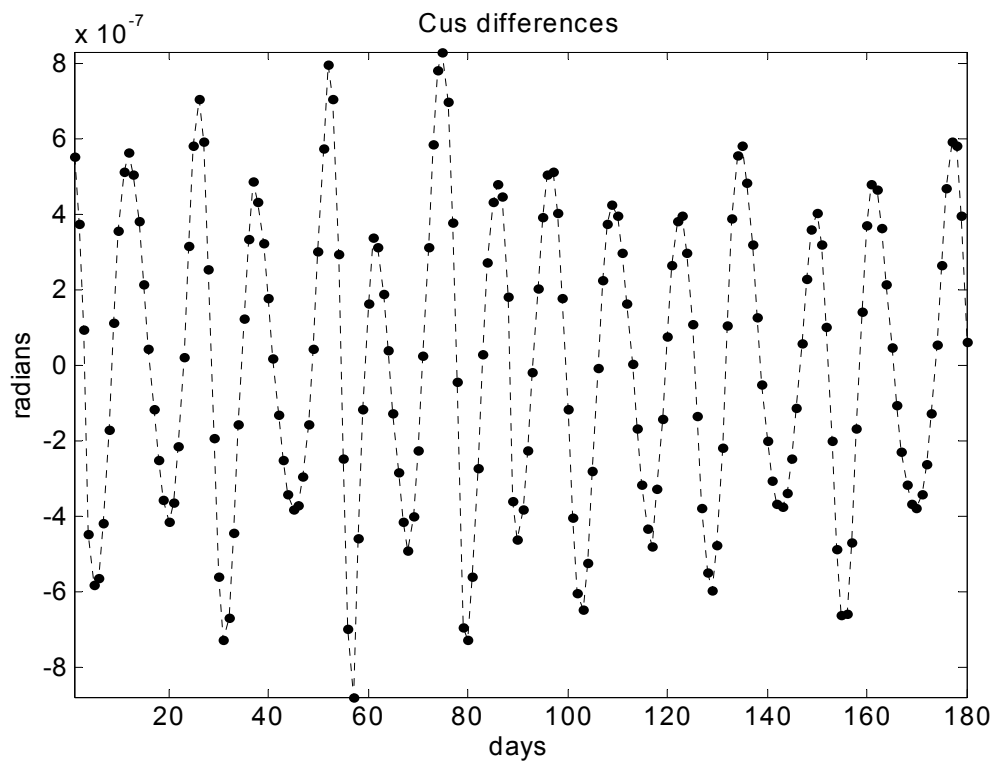


Figure F.10 Cus Differences Day to Day

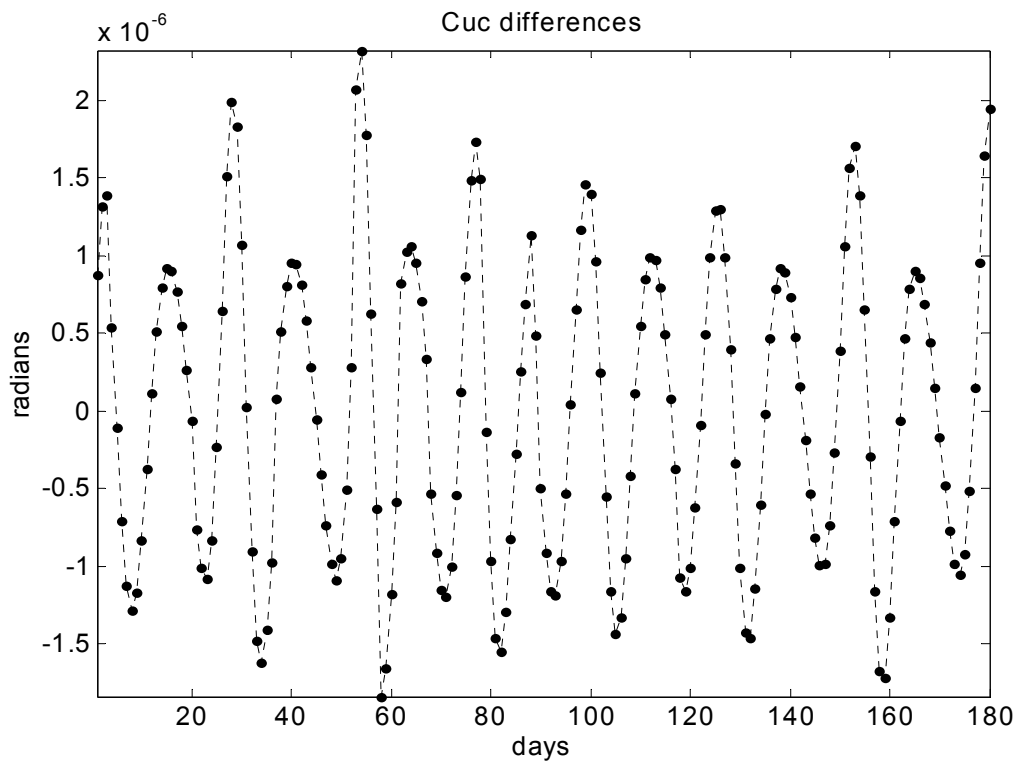


Figure F.11 Cuc Differences Day to Day

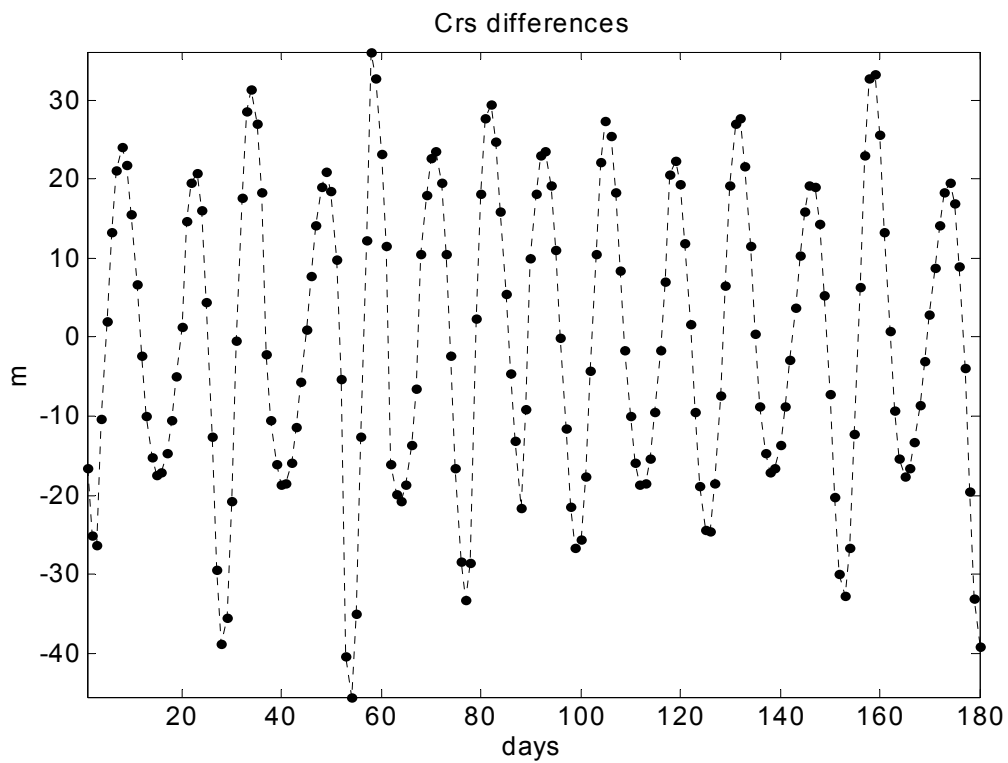


Figure F.12 Crs Differences Day to Day

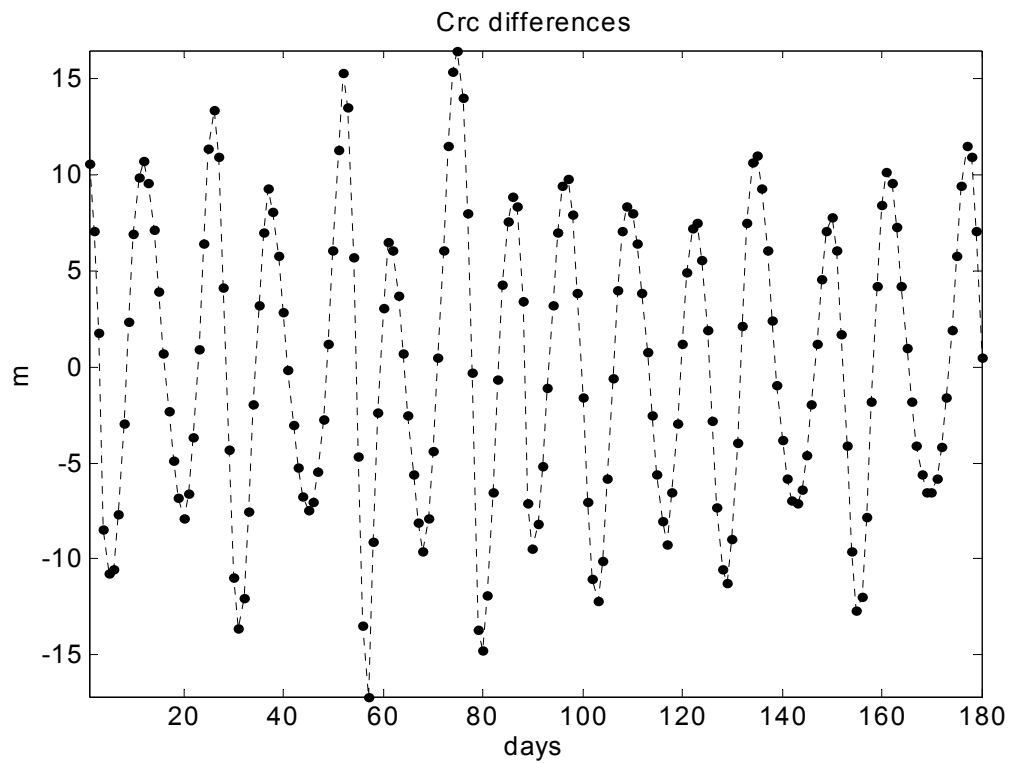


Figure F.13 Crc Differences Day to Day

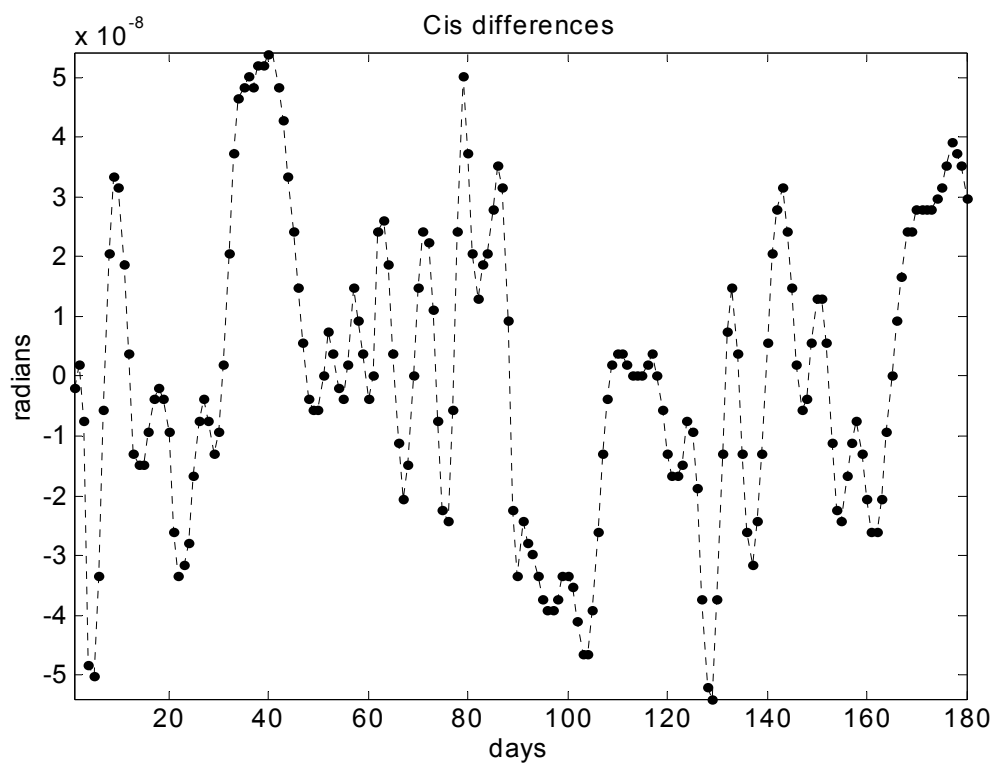


Figure F.14 Cis Differences Day to Day

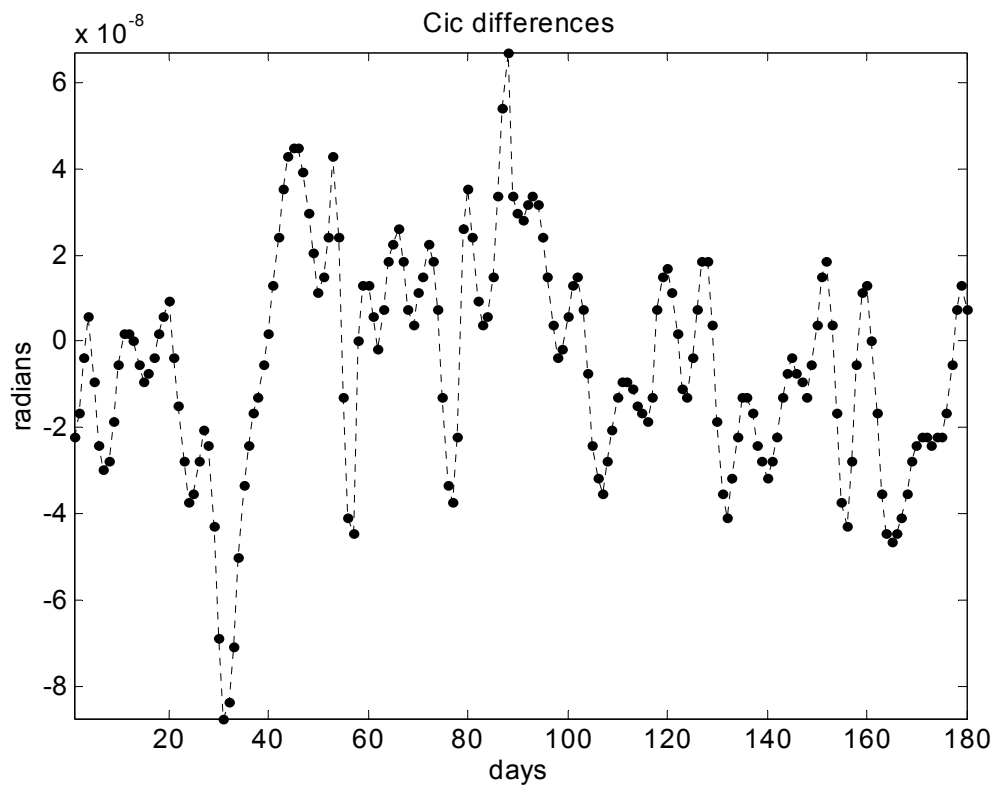


Figure F.15 Cic Differences Day to Day

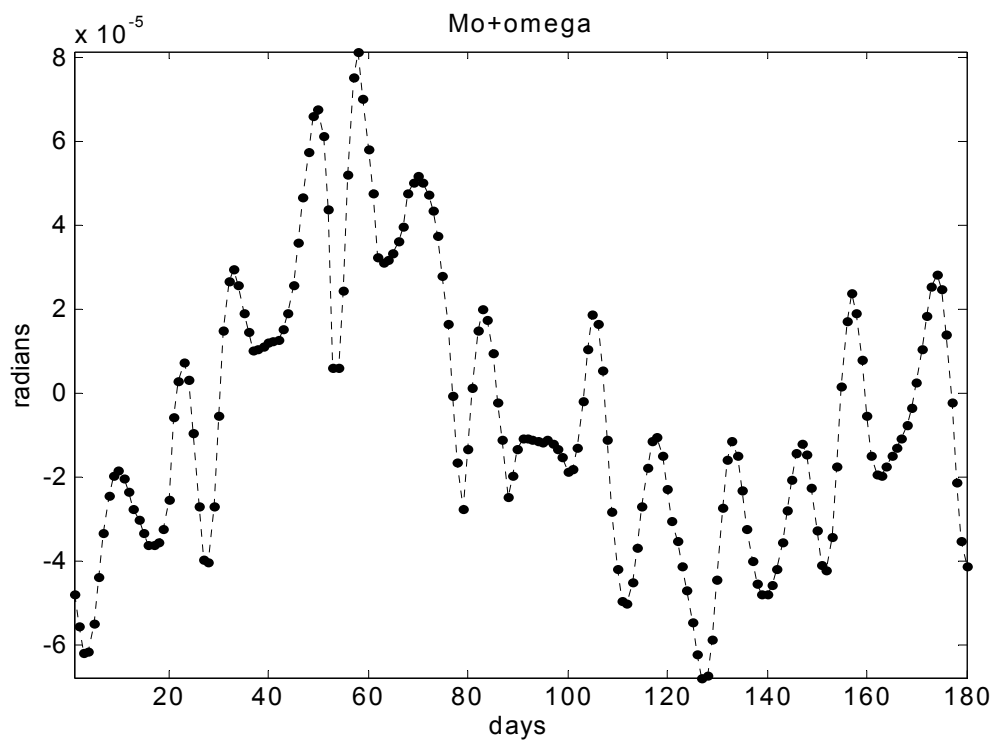
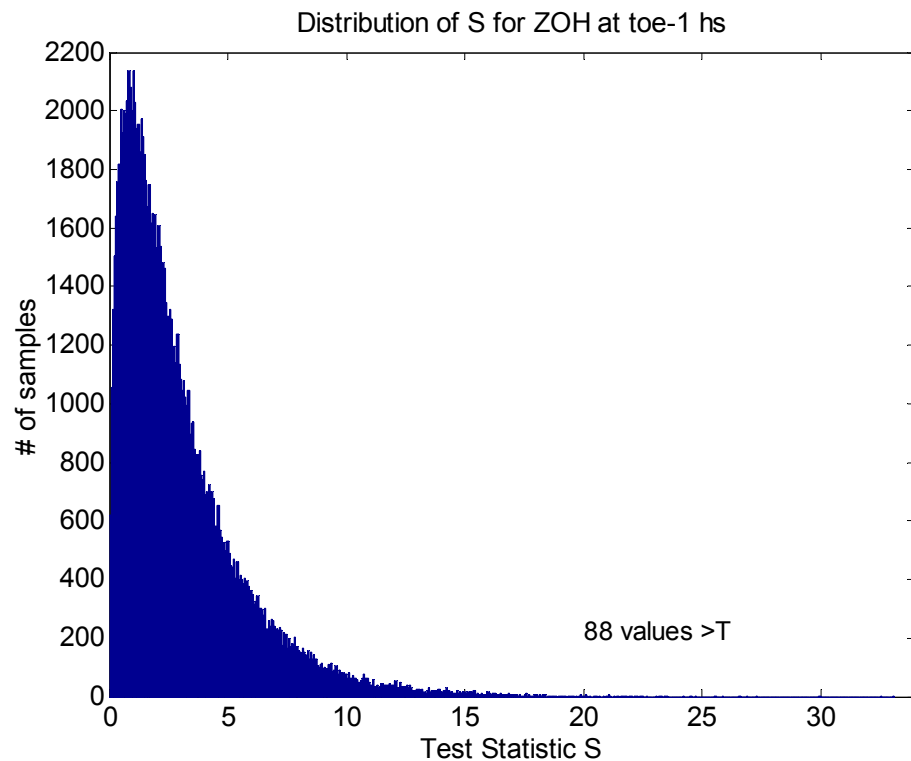
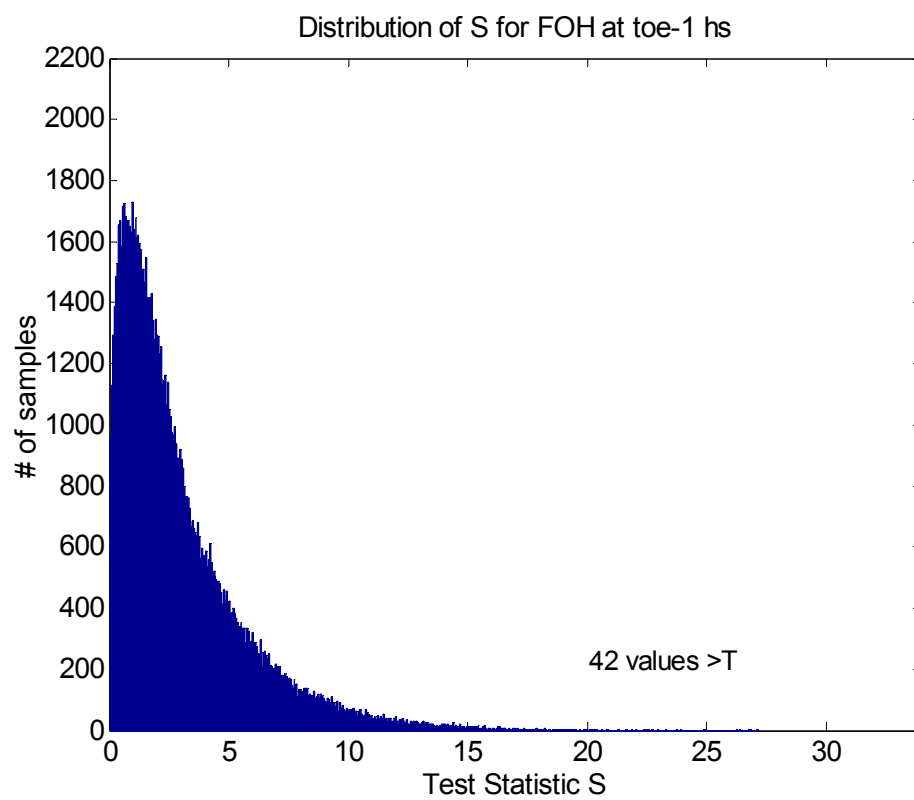
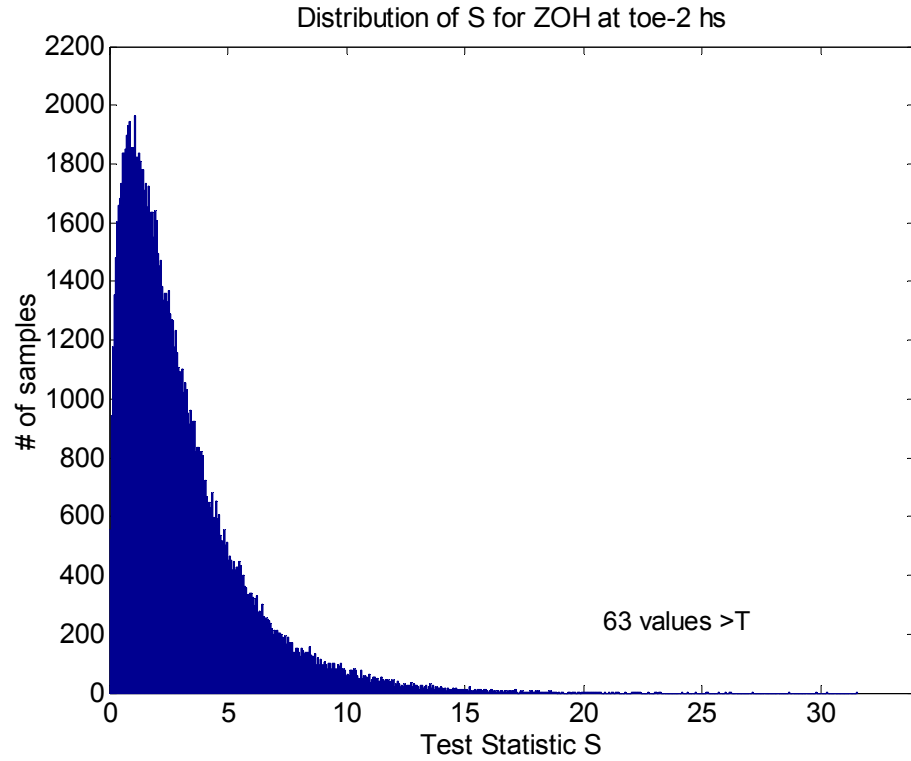
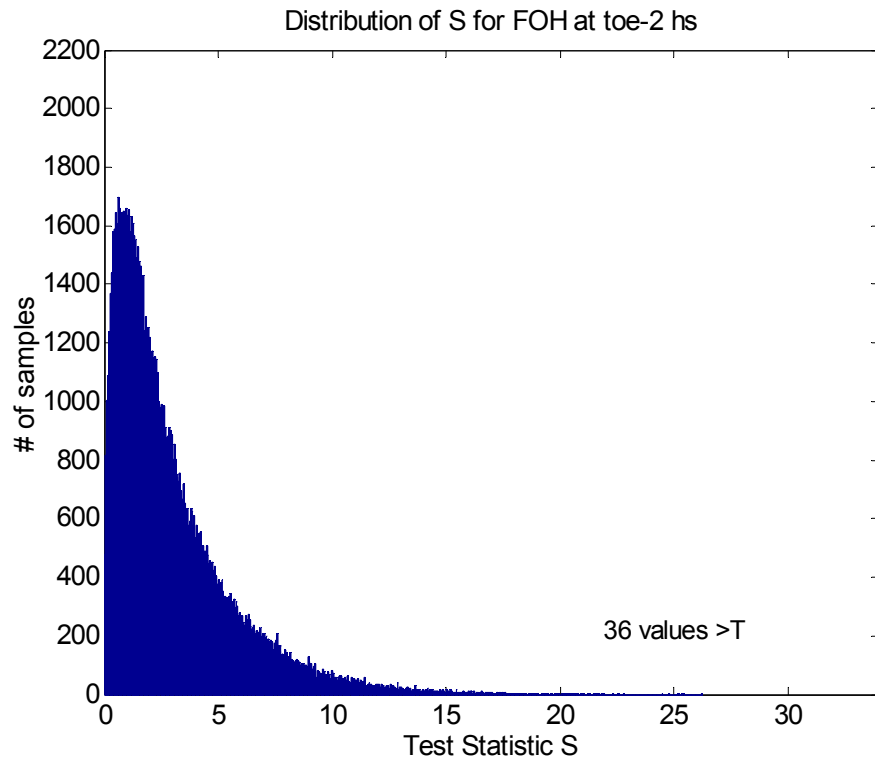


Figure F.16 Mo+omega Differences Day to Day

APPENDIX G

DISTRIBUTION OF TEST STATISTIC S FOR K DIFFERENT THAN 0

Figure G.1 Values of S with ZOH and $k = -1$ hFigure G.2 Values of S with FOH and $k = -1$ h

Figure G.3 Values of S with ZOH and $k = -2$ hFigure G.4 Values of S with FOH and $k = -2$ h

APPENDIX H

DETAIL OF CDF PLOTS FOR K DIFFERENT THAN 0

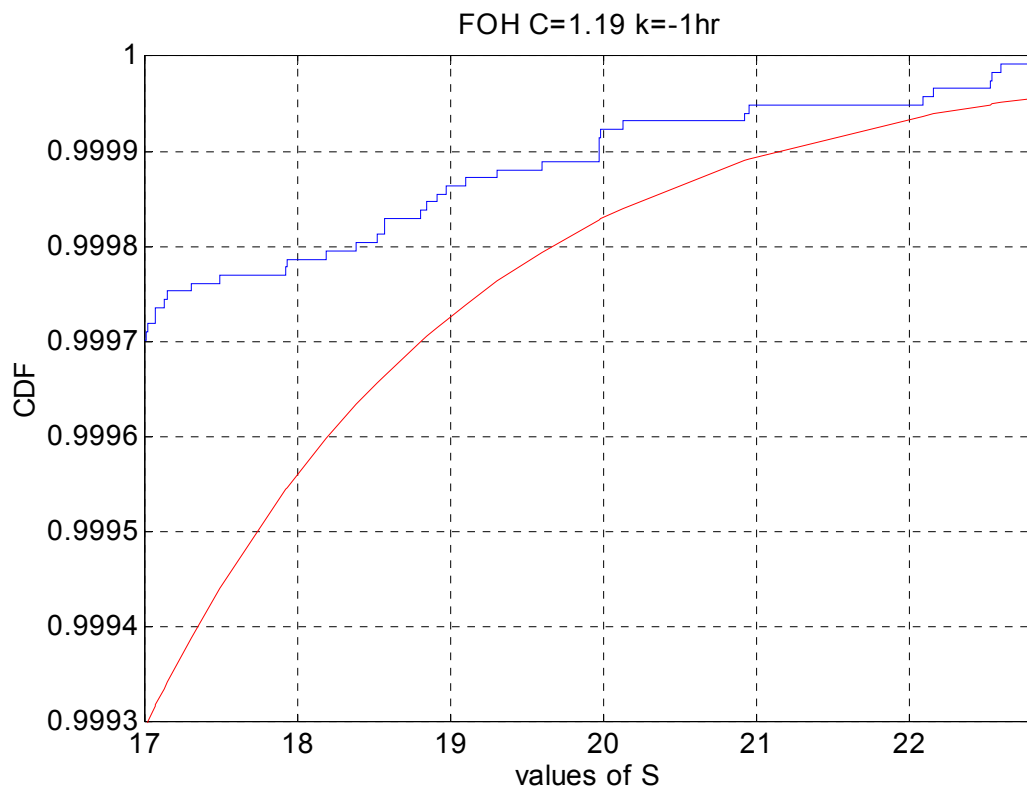


Figure H.1 FOH Theoretical and Empirical CDF Tails k= -1 h

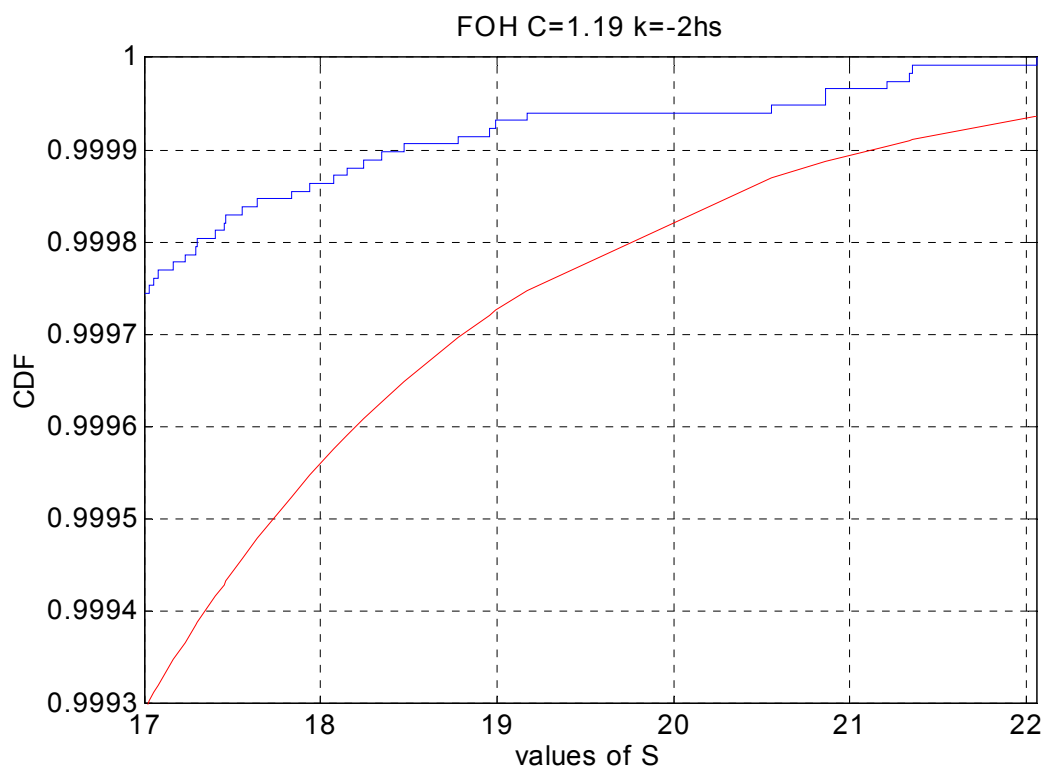


Figure H.2 FOH Theoretical and Empirical CDF Tails k= -2 h

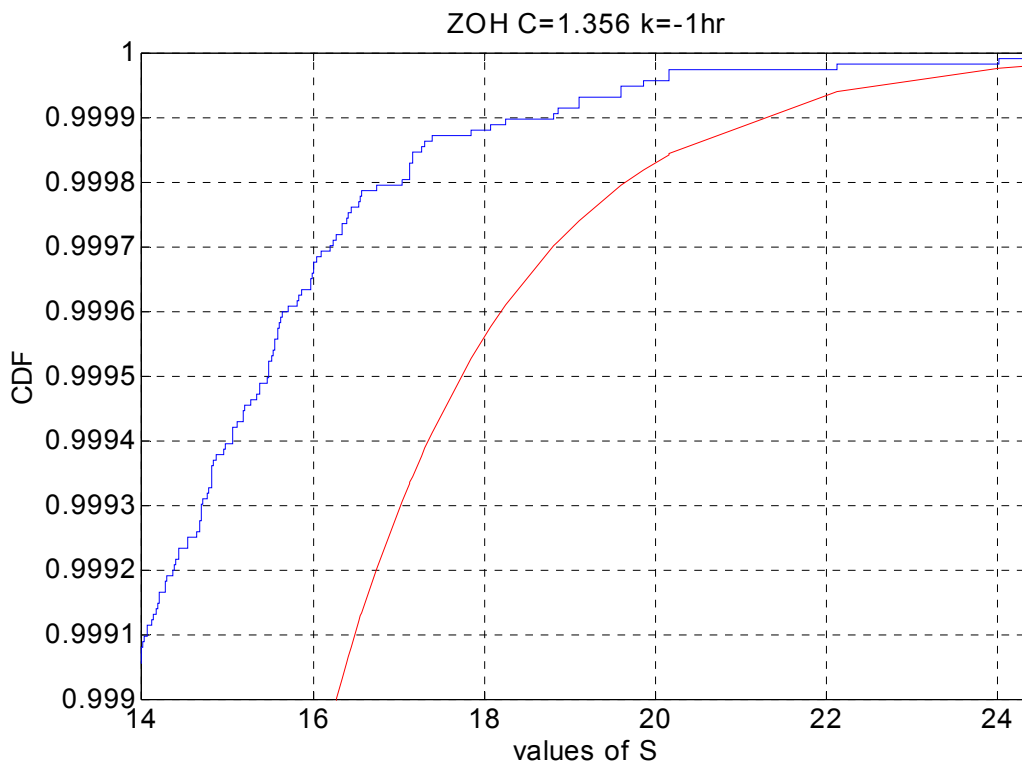


Figure H.3 ZOH Theoretical and Empirical CDF Tails $k= -1$ h

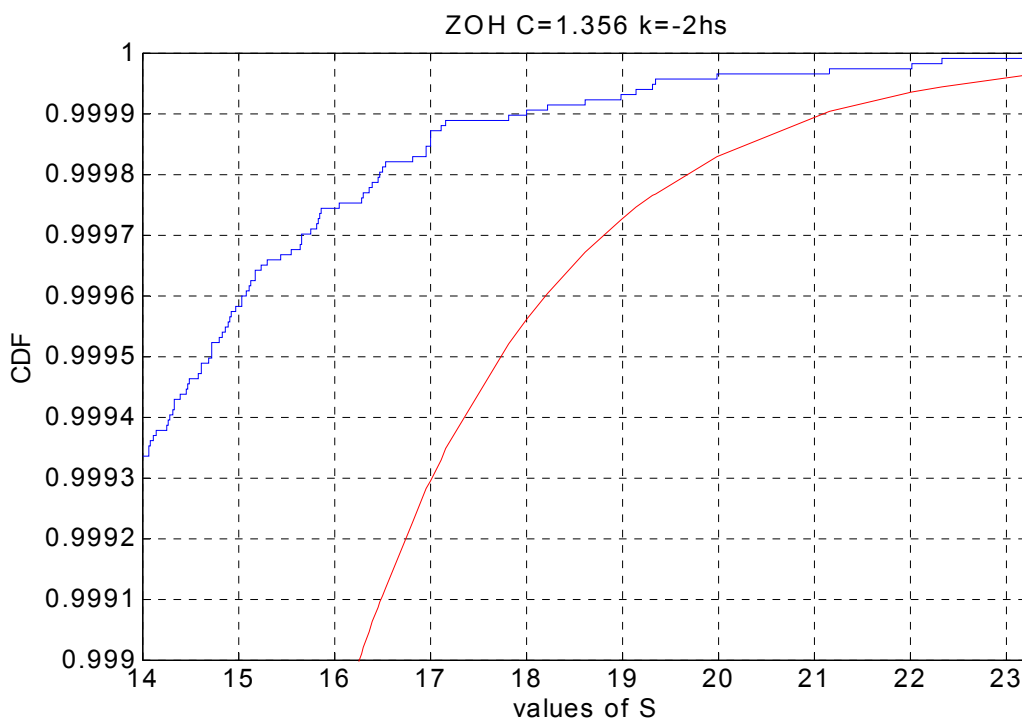


Figure H.4 ZOH Theoretical and Empirical CDF Tails $k= -2$ h

APPENDIX I

SENSITIVITY OF MDE VALUES TO LGF SITING

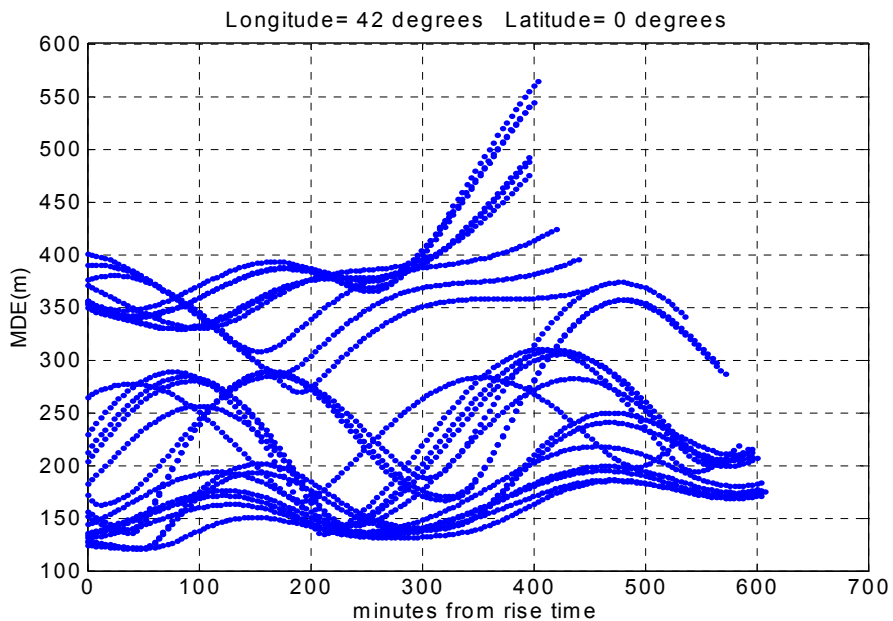


Figure I.1 MDE values From Measurement Based Monitoring Latitude=0°

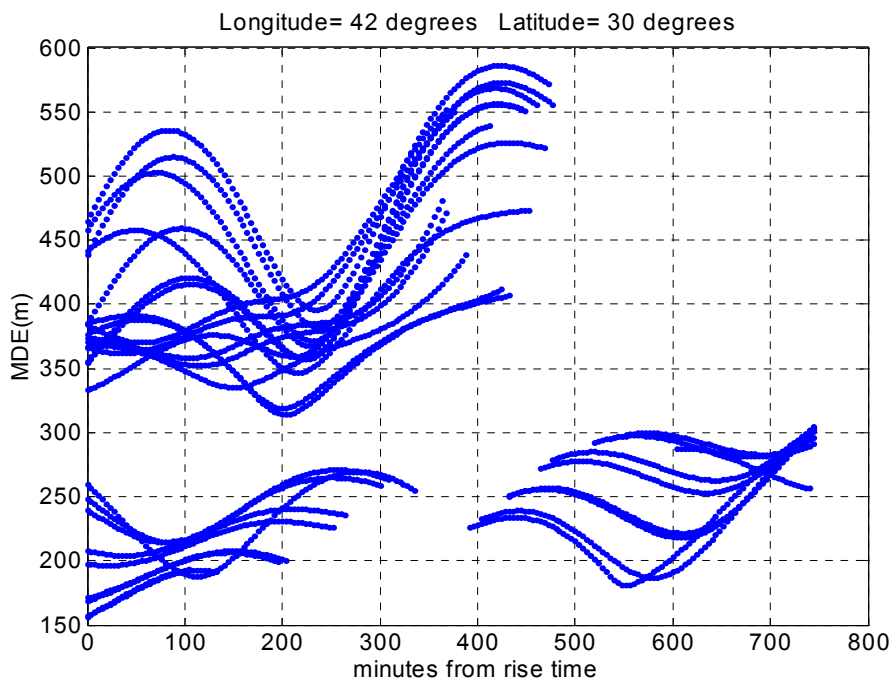


Figure I.2 MDE values From Measurement Based Monitoring Latitude=30°

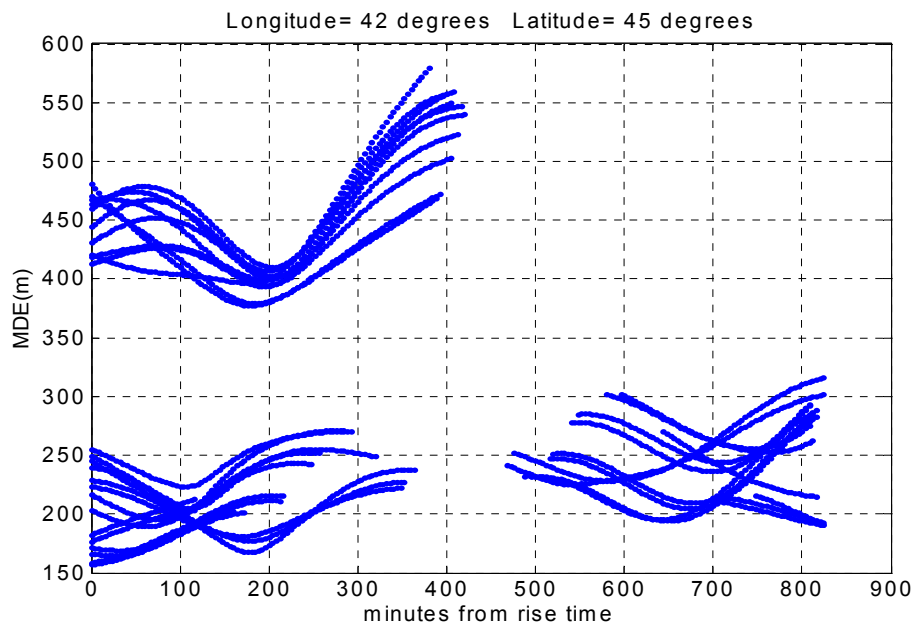


Figure I.3 MDE values From Measurement Based Monitoring Latitude=45°

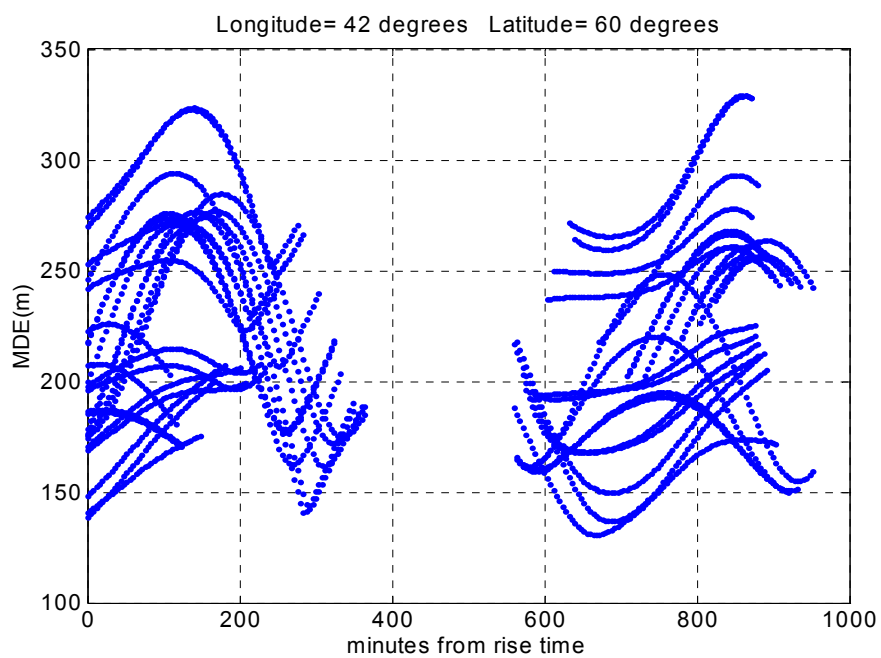


Figure I.4 MDE values From Measurement Based Monitoring Latitude=60°

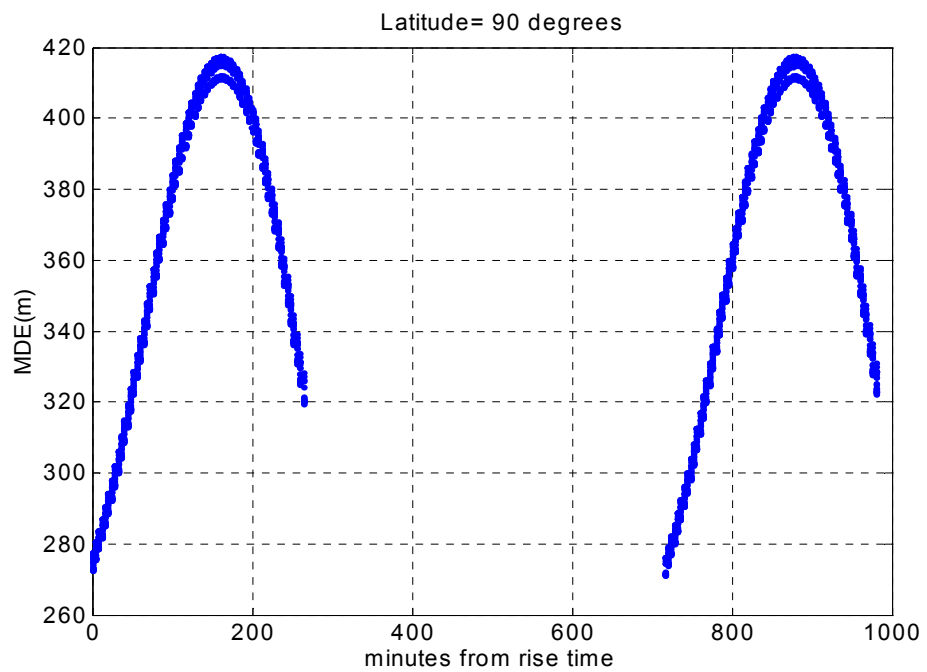


Figure I.5 MDE values From Measurement Based Monitoring Latitude=90°

BIBLIOGRAPHY

- [Cha01] Chan, F.C, "Detection Of Global Positioning Satellite Orbit Errors Using Short-Baseline Carrier Phase Measurements" Illinois Institute of Technology MS. Dissertation, MMAE Department, Jul. 2001.
- [Gel74] Gelb, A., Kasper Jr., J.F., Nash Jr., R.A., Price, C.F., and Sutherland Jr., A.A., Applied Optimal Estimation, M.I.T. Press, 1974.
- [ICD-200] Interface Control Document (ICD) GPS-200, Revision B, Rockwell International, 1987.
- [Mis99] Misra, P., Burke, B.P., and Pratt, M.M., "GPS Performance in Navigation," Transactions of the IEEE. VOL.87, No.1, Jan. 1999.
- [Par94] Parkinson, B., "Introduction and Heritage of NAVSTAR, the Global Positioning System," Global Positioning System: Theory and Applications, Vol. I, pp. 3-28, AIAA, 1994.
- [PT1LAAS99] "Specification: Performance Type One Local Area Augmentation System Ground Facility," United States Department of Transportation, Federal Aviation Administration, FAA-E-2937, Sep. 1999.
- [PTLAAS00] Minimum Operational Performance Standards for GPS Local Area Augmentation System Airborne Equipment. Washington, D.C.: RTCA SC-159 WG-4A, DO-253, January 11, 2000.
- [PTFAA01] Specification: Category One Local Area Augmentation System Non-Federal Ground Facility. Washington, D.C.: U.S. Dept. of Transportation, Federal Aviation Administration, FAA/AND710-2937, May 31, 2001.
- [Pul02] Pullen, S., Pervan, B., Lee, J., Luo, M., Chan, F.C, Gratton, L.R., "Ephemeris Protection Level Equations and Monitor Algorithms for GBAS" Department of Aeronautics and Astronautics, Stanford University, Department of Mechanical, Materials, and Aerospace Engineering, Illinois Institute of Technology, Aug. 2001.
- [Shi01] Shively, C.A., "Preliminary Analysis of Requirements for Cat IIIB LAAS," Proceedings of the 57th Annual Meeting of the Institute of Navigation, Albuquerque, NM, Jun. 2001.
- [Spi94] Spilker Jr., J.J., and Parkinson, B.W., "Overview of GPS Operation and Design," Global Positioning System: Theory and Applications, Vol. I, pp. 29-55, AIAA, 1994.

- [Zum96] Zumberge, J., and Bertiger, W., “Ephemeris and Clock Navigation Message Accuracy” Global Positioning System: Theory and Applications, Vol. I, pp. 585-599, AIAA, 1996.